Thesis for the Degree of Doctor of Science

Search for Gauge–Mediated SUSY Breaking in Diphoton Events in $p\bar{p}$ Collisions at $\sqrt{s} = 1.96$ TeV

Minsuk Kim

Department of Physics, Major in Particle Physics

The Graduate School

December 2004

The Graduate School
Kyungpook National University

Thesis advisor
DongHee Kim

Author
Minsuk Kim

Search for Gauge–Mediated SUSY Breaking in Diphoton Events in $p\bar{p}$ Collisions at $\sqrt{s} = 1.96$ TeV

Abstract

We present the results of a search for anomalous production of diphoton events with large missing transverse energy using the Collider Detector at Fermilab. In 202 pb^{-1} of $p\bar{p}$ collisions at $\sqrt{s} = 1.96$ TeV we observe no candidate events, with an expected standard model background of $0.27 \pm 0.07(\text{stat}) \pm 0.10(\text{syst})$ events. The results exclude a lightest chargino of mass less than 167 GeV/c^2, and lightest neutralino of 93 GeV/c^2 at 95% confidence level in a gauge–mediated supersymmetry–breaking model with a light gravitino.

Acknowledgements

I would like to thank my supervisor, Prof. DongHee Kim, for giving tremendous support from start to finish, and for inclining my mind to get the utmost out of my ability and background. He gave me to the opportunity to join the High Energy Physics group at the Kyungpook National University and gain my experience quite a lot in the challenging experiments. Besides all this, he pushed me in the world. I am deeply grateful to Dr. Ray Culbertson for his continual support, encouragement and guidance and for providing physics advice on photon analysis, as well as a gigantic help in closing the loop on the analysis. He is a great and understanding person, who is very kind. I want to thank Prof. Dave Toback for demanding that things make sense, which allowed me to delve into every corner of the analysis. He was also a huge help in many useful discussions and conversations. I am extremely grateful to Dr. Sungwon Lee. I simply cannot believe how lucky I am. I could not have survived without his energetic support throughout this whole thing.

I want to thank the Exotics conveners, Stephan Lammel, Beate Heinemann, Song-Ming Wang, Peter Wittich and Michael Schmitt without whose help I never would have finished this analysis. I am also grateful to Henry Frisch, Jane Nachtman, Giulia Manca for their Godparenting and encouraging support. The main results of this analysis have been accepted by CDF II collaboration for publication.

I very much thank Dr. Steve Kuhlmann for his powerful leadership of preshower detector upgrade at CDF. He always encouraged me in doing my best. This work also gave me the opportunity to have long and pleasant experience in hardware and software, and to work with many active people, Drs. Larry

Nodulman, Fumi Ukegawa, Maurizio Iori, Michele Gallinaro, Joey Huston and Willis Sakumoto. Thanks a lot! Thanks to Zeljko Matijas at Argonne Lab for teaching technical things on detector assembly and sharing his huge interest on all of the things. Thanks to Dr. Bob Blair for working together in material count using preshower detector. I want to thank Dr. Bob Michaels at JeffersonLab for starting my interest in experimental particle physics and teaching me basic analysis. Thanks to Dr. Gerry Bauer for being the careful leader of the TOF detector at CDF. He has spent so much time encouraging me with friendly advice. Thank you Koji Sato for the TOF maintenance shift partner. I want to thank Jim and Takashi for working together during the DAQ and detector monitoring shift. Thanks to Carsten for his friendly help and much interest in Korea.

The Korea contingent at CDF have been a family away from home - so many good friends, too many to mention all of them here, but special thanks to – Jaison Lee, Iisung Cho, Jieun Kim, Moohyun Ahn, Sung-Chul Hong, Eunjeong Son, Young-Jang Lee, Yuchul Yang and Sunghyun Chang, who have made the four years a lot more exciting and interesting than I hoped for – it is really possible! A million thanks to Dr. Youngdo Oh for being totally devoted to his work that has placed the CDF Korea group on a stable foundation. I want to thank Prof. Kihyeon Cho for encouraging me to give a talk in the APS meeting. He was also a gigantic help with enormous interest and responsibility. I bear the Korean house in memory... I was a pretty basic cook but I could just about feed a couple of people then. It seems to be pretty rusty at present.

Special thanks must go to Dr. Jae-Chul Yun and Mrs. Yun for praying for me and my family during my job search. Thanks to Asbury family! I would like to thank Dr. Soon Yung Jun for always encouraging me in doing my best, with a word of advice from an abiding interest. I am grateful to Prof. Jungil Lee for giving me sensible advice and inspiration. Thank you Dr. Hyunsoo Kim, who is travelling in his native country, for many useful physics discussions, his help and encouragement. Bon Voyage! I want to thank Dr. Hyangku Park, Mrs. Park and Ein for helping while living in the same town. Thanks to Dr. Un-Ki Yang (his wife Shinae Lee) with truly help "Yunu" for a hearty welcome. Many

thanks to Dr. Yeonsei Chung and Mrs. Chung for feeding students for all of those years. Thanks to Dongwook Jang (Mrs. Jang and Alexy) for several field breaks. A billion thanks to Daejung Kong (his wife and child, Nam-Mi Lee and Sukyung) and Dr. Jonghee Yoo, I think, you guys are cool! It is a pleasure to acknowledge a warm friendship with Jedong. He always made sure things were done fairly and with pinpoint accuracy. I gratefully acknowledge the help and support from Fermilab Koreans, Drs. Seung-Chan Ahn, Woo-Hyun Chung, Young-Kee Kim, Suyong Choi, Minjeong Kim, Dookee Cho and Sung-hwan Ahn.

I am sincerely thankful to Profs. Dongchul Son, Gui Nyun Kim, Soo-Bong Kim, Intae Yu, Hwanbae Park, Il Park, Wooyoung Kim, Hong-Joo Kim, Sang Ryul Ro, Bockjoo Kim, Jun-Suhk Suh and Seung-Woo Ham for the invaluable advice and encouragement. Thanks to my CHEP members, Man-woo Lee, Kockhee Han, Daehee Han, Wung-Hoa Park, Hyeyun Chin, Suk-Hee Koo, as well as my previous colleagues, Chiwoon Yun, Byung-Jae Ahn, Hyun-gun Jun, Dongho Kim, Gil-Ho Park, Jung-Wook Shin and Dr. Heuijin Lim. Thanks to Jae-Ho, who is a very friendly person, for the most fun time of my life. My thanks goes out to my best friends, Ik-Joon and Ki-Hun, who are very patient and hearty.

Finally, I would like to thank Mom, Dad, my sister Miyoung and her family, for their love, support and encouragement throughout all of my education. I am deeply grateful to Grandpa and Grandma for always loving, caring and understanding. Of course I must thank my Parents-in-law for their full confidence, support and encouragement in my study abroad. Especially many thank-yous to my wonderful wife and first child of one, YoungHye and Emily-Jiyeon, for encouraging and believing in me with your smile, love and help. They gave me the opportunity to concentrate on my research and so they deserve the most thanks. I dedicate this thesis to them.

Contents

List of Figures

List of Tables

Chapter 1

Introduction

Nature has arranged things so that the newborn baby focuses best at the distance he is from his mother's face when he is in her arms.

- in BabyTalk by Dr. Sally Ward

The standard model (SM) of elementary particles has been enormously successful, but it is incomplete [1]. For theoretical reasons [2, 3], and because of the '$ee\gamma\gamma$ + missing transverse energy ($\not\!\!E_T$ or MET)' candidate event recorded by the CDF detector in Run I [4, 5], there is a compelling rationale to search in high–energy collisions for the production of heavy new particles that decay producing the signature of $\gamma\gamma + \not\!\!E_T$. Of particular theoretical interest are supersymmetric (SUSY) models with gauge–mediated SUSY–breaking (GMSB). Characteristically, the effective SUSY–breaking scale (Λ) can be as low as 100 TeV, the lightest SUSY particle is a light gravitino ($\widetilde{G}$) that is assumed to be stable, and the SUSY particles have masses that may make them accessible at Tevatron energies [2].

1.1 SUSY with Gauge–Mediated Breaking

Supersymmetry is usually assumed to be broken in a hidden sector of particles and then communicated to the observable sector (where all the particles and their superpartners lie) via gravitational interactions. An alternative possibility is that this mediation is performed by Standard Model gauge interactions, leading to models of gauge mediated supersymmetry breaking. In most current GMSB theoretical work [2], it is assumed that the hidden sector is coupled to a messenger sector, which in turn couples to the visible sector through radiative corrections with gauge-interaction strength.

The primary motivation for GMSB is that it naturally accommodates the experimentally observed absence of flavour changing neutral currents due to the fact that gauge interactions are flavour blind. In these models the scale of SUSY breaking ($\sqrt{F}$) can be as low as about 10^4 or 10^5 GeV in order to have supersymmetric particle (sparticle) masses of the right order of magnitude (a few hundred GeV/c^2). [1] With spontaneously broken local supersymmetry, the spin $\frac{1}{2}$ Goldstino becomes the longitudinal components of the spin $\frac{3}{2}$ gravitino superpartner of the graviton. The mass of the gravitino ($\widetilde{G}$) is related to the scale of SUSY breaking through the expression:

$$m_{\widetilde{G}} = \frac{F}{\sqrt{3}M_P} \simeq 2.4 \times \left(\frac{\sqrt{F}}{100 \text{ TeV}}\right)^2 \text{ eV}/c^2, \tag{1.1}$$

where $M_P = 2.4 \times 10^{18}$ GeV is the reduced Plank mass and F is a vacuum expectation value which measures the magnitude of supersymmetry breaking in the vacuum state. Therefore $m_{\widetilde{G}}$ can be as low as few eV/c^2. Consequently in these models $\widetilde{G}$ is the lightest supersymmetric particle (LSP) and all the other sparticles will decay into final states that include it. Gavitino masses below 3×10^{-4} eV/c^2 have been ruled out using Tevatron data for the multijet final state [6]. On the other hand, hints from cosmology point in the direction of either a light gravitino with mass below 1 keV/c or a heavy one with mass above 1 TeV/c [7, 8].

[1] In gravity mediated SUSY breaking models $\sqrt{F} \sim 10^{10}$ or 10^{11} GeV.

The supersymmetric models with GMSB are characterized by a supersymmetry breaking scale Λ as low as 100 TeV and a light gravitino which is naturally the lightest supersymmetric particle. In GMSB models the standard model gauge interactions act as messengers of supersymmetry breaking if fields within the supersymmetry breaking sector transform under the standard model gauge group. The entire minimal supersymmetric standard model (MSSM) spectrum can be predicted in terms of the following parameters: [2]

Λ	the effective SUSY breaking scale
M_m	the messenger mass scale
N	the number of messenger generations
$\tan\beta$	the ratio of the MSSM Higgs vacuum expectation values
$\mathrm{sign}(\mu)$	the sign of the Higgs sector mixing parameter
C_G	the ratio of the messenger sector

In some sense, the most important parameter is Λ because it sets the overall mass scale of supersymmetric particles. To first approximation, all of the MSSM superpartner masses scale linearly with Λ. The gaugino masses scale like the number of messenger generation, N, is also very important because it determines which sparticle is the next-to-lightest supersymmetric particle (NLSP). For $N = 1$ the NLSP is mainly the lightest neutralino ($\widetilde{\chi}_1^0$), and for $N \geq 2$ it is one of the sleptons. While the NLSP decay length scales like C_G^2 and also depends on $m_{\widetilde{G}}$ [9], for much of the parameter space it is very small, and for our purposes we assume the lifetime is zero. [3]

The coupling to the gravitino is very weak, therefore, all the superparticle other than the next-to-lightest supersymmetric particle undergo chain decay down to the NLSP which finally decays to the gravitino. [4]

[2]The magnitude of μ is calculable from the other parameters in the model by imposing radiative electroweak symmetry breaking.

[3]The mass range $m_{\widetilde{G}}$ between a few eV/c^2 and a few hundred eV/c^2 is favored for cosmological reasons and typically produces a neutralino lifetime of less than a few hundred nsec depending on the NLSP mass. This parameter is important because the lifetime determines whether the NLSP decays inside or outside the detector. For more discussion of the issues and details of prospects of searches with long-lived neutralinos-NLSPs which decay to $\gamma\widetilde{G}$ see Ref. [10].

[4]The gravitino mass determines if the NLSP decay inside or outside the detector. For

1.2 Neutralino NLSP

In this paper data were analysed within the lightest neutralino NLSP scenario as discussed in the following [3].

Neutralinos are in general mixtures of the gauginos and Higgsinos. Since the gauginos are superpartners of the gauge bosons, a gaugino-like neutralino NLSP decays to the Goldstino predominantly by emission of a γ or Z boson. In many models of supersymmetry breaking, including the minimal model of gauge-mediation (MGM) [3], the gaugino masses are related by gaugino mass unification relations which imply that a gaugino-like neutralino NLSP is mostly Bino, the superpartner of the $U(1)_Y$ hypercharge gauge boson. Since the projection of the hypercharge gauge boson is larger in the photon than in the Z boson and because of the more favorable kinematics, a Bino-like neutralino NLSP decays to the Goldstino predominantly by emission of a photon:

$$\widetilde{\chi}_1^0 \rightarrow \gamma\widetilde{G} \tag{1.2}$$

Supersymmetric particles are produced in pairs, with all cascades passing through the NLSP (see Figure 1.1). For a Bino-like neutralino NLSP which decays by above equation, all supersymmetric final states include two hard photons, large missing energy carried off by the Goldstinos, and possibly other hard partons from cascade decays to the NLSP, $\gamma\gamma X \not{E}_T$. If the supersymmetry breaking scale $\sqrt{F}$ is smaller than a few 100 TeV, the decay length is short enough that the two hard photons appear to originate from the interaction point. In this case the photons are said to be prompt. However, for $\sqrt{F}$ between a few 100 and a few 1000 TeV, the decay of NLSP can take place over a macroscopic distance, but within the detector. In this case the photons are said to be non-prompt or displaced, with a finite distance of closed approach to the interaction point. For $\sqrt{F}$ greater than a few 1000 TeV, the decays take place outside the detector. In this case $\widetilde{\chi}_1^0$ is essentially stable on the scale of

example, for $m_{\widetilde{G}}$ between a few eV/c^2 and a few hundred eV/c^2 ($\sqrt{F} \lesssim 1000$ TeV), the NLSP has an intermediate mean decay length and it would decay in flight in some part of the detector volume. This range of $\sqrt{F}$ is in fact consistent with astrophysical and cosmological considerations [8, 11].

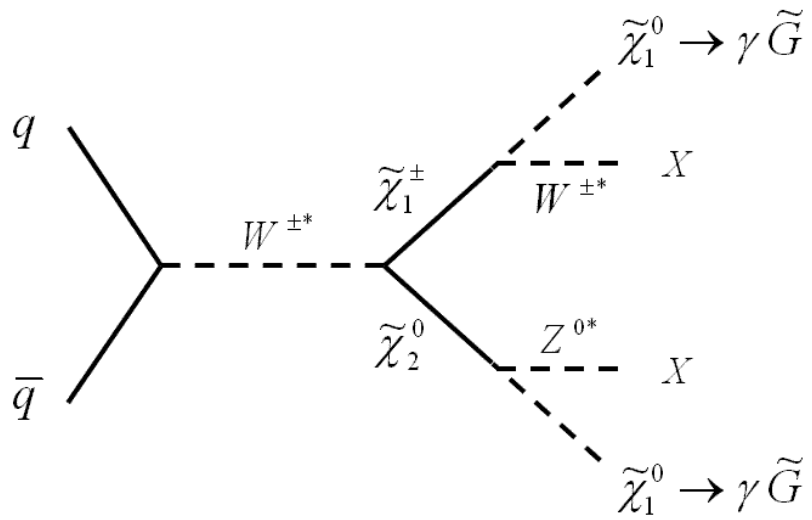

Figure 1.1: The Feynman diagram for $\widetilde{\chi}_1^{\pm}\widetilde{\chi}_2^0$ pair production and and decay in the light gravitino scenario. Both gauginos decay to the lightest neutralino, $\widetilde{\chi}_1^0$, which in turn decays via $\widetilde{\chi}_1^0 \to \gamma\widetilde{G}$.

the experiment and escapes as missing energy. The resulting signatures are then qualitatively similar to traditional SUSY missing energy signatures with a stable $\widetilde{\chi}_1^0$, and will not be considered further in this paper. The experimental signatures that are unique to a Bino-like neutralino NLSP with low scale supersymmetry breaking are therefore:

$$\gamma\gamma + X + \not{E}_T, \qquad X = \text{leptons and jets} \tag{1.3}$$

Observation of either of these signatures would yield interesting information about the superpartners and supersymmetry breaking. The final state $\gamma\gamma X\not{E}_T$, interpreted as arising from decay to Goldstino pairs, would immediately imply that the supersymmetry breaking scale is low. A large branching ratio for $\widetilde{\chi}_1^0 \to \gamma\widetilde{G}$ would imply the NLSP is mostly Bino. Finally, with displaced photons, the decay length distribution would yield the neutralino life time, and give an essentially model independent measure of the SUSY breaking scale.

For the quantitative studies presented in this paper, a Model Line within the MGM is defined in which the NLSP is Bino-like with nearly 100% branching

ratio $\widetilde{\chi}_1^0 \to \gamma\widetilde{G}$. The fixed parameters that define the Model Line are:

$$\text{Bino}-\text{like Neutralino NLSP}: \; N = 1, \; \frac{M_m}{\Lambda} = 2, \; \tan\beta = 15, \; \mu > 0, \quad (1.4)$$

with the overall superpartner mass scale defined by Λ, which is allowed to vary. The mass spectrum of the phenomenologically important superpartners and the lightest CP-even Higgs boson h^0, is shown in Figure 1.2 as a function of Λ in the range 45–90 TeV. Over the entire model line $\widetilde{\chi}_1^0$ is the NLSP, and the mass ordering of the superpartner spectrum is $m_{\widetilde{\chi}_1^0} < m_{\widetilde{\ell}_R} < m_{\widetilde{\chi}_2^0, \widetilde{\chi}_1^\pm}$. The left-handed sleptons, the mostly-Higgsino neutralino and chargino states, the squarks, and the heavy Higgs bosons, are all too heavy to be produced from the Tevatron collider at the Fermi National Accelerator Laboratory (Fermilab). The lightest neutralino, $\widetilde{\chi}_1^0$, is mostly $U(1)_Y$ Bino, while $\widetilde{\chi}_2^0$ and $\widetilde{\chi}_1^\pm$ are mostly $SU(2)_L$ Wino, and nearly degenerate. The light right-handed sleptons, $\widetilde{e}_R$ and $\widetilde{\mu}_R$, are effectively degenerate with $\widetilde{\tau}_1$ which is mostly $\widetilde{\tau}_R$ with a small $\widetilde{\tau}_L$ component from left-right mixing. The Higgs mass varies very slowly along the model line, due mainly to the varying virtual effects of the massive stop sqaurks.

The total SUSY cross sections for the light states are shown in Figure 1.3. The largest cross sections are for $\widetilde{\chi}_1^+\widetilde{\chi}_1^-$ and $\widetilde{\chi}_1^\pm\widetilde{\chi}_2^0$ production. These arise predominantly in the S-wave through off-shell γ^*, Z^*, and W^* couplings to the $SU(2)_L$ Wino components. Even through the right-handed sleptons are lighter, $\widetilde{\ell}_R^+\widetilde{\ell}_R^-$ production cross sections are smaller because of P-wave suppression and smaller $U(1)_Y$ hyperchage coupling. Since the two largest production cross-sections both involve the chargino, $\widetilde{\chi}_1^\pm$ is probably the best figure of merit for the discovery reach along this Model Line.

1.3 Overview

Prompt decays $\widetilde{\chi}_1^0 \to \gamma\widetilde{G}$ give rise to spectacular events with two hard photons and significant missing energy. A search for $\gamma\gamma X \not\!\!E_T$ events provides a very sensitive discovery reach for SUSY in this channel for a number of reasons. The $\gamma\gamma$ branching ratio is nearly 100%, which gives a large advantage

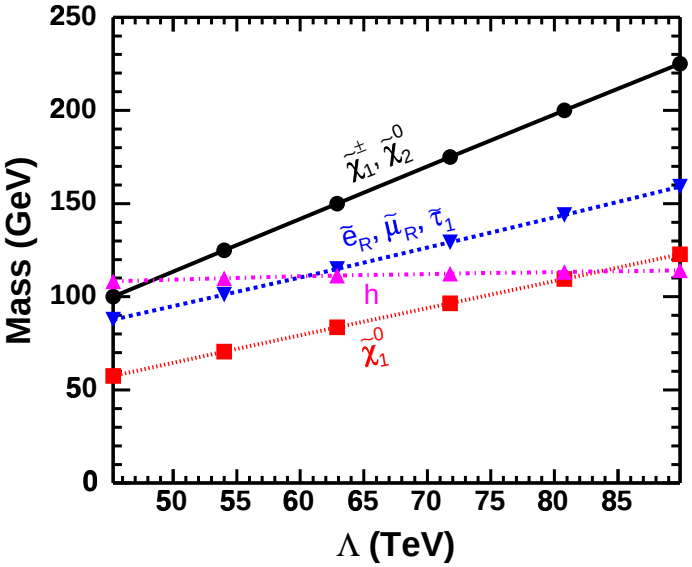

Figure 1.2: The masses of the lightest neutralinos, charginos, sleptons, and lightest CP–even Higgs boson as a function of the overall scale Λ along the Neutralino NLSP.

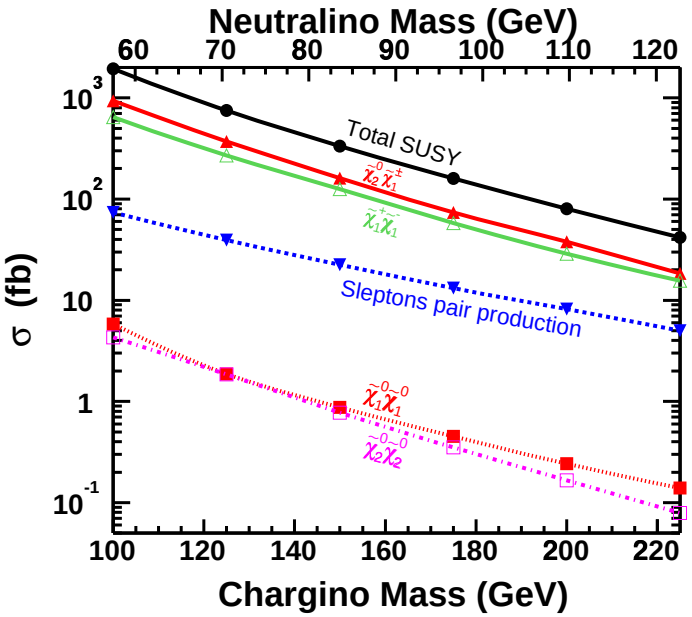

Figure 1.3: The most significant supersymmetric total production cross sections, at leading order (LO), in $p\bar{p}$ Collisions at $\sqrt{s} = 1.96$ TeV, as functions of $\widetilde{\chi}_1^{\pm}$ and $\widetilde{\chi}_1^0$ along the Neutralino NLSP.

over other channel which require, for example, leptonic decay of W and/or Z. There is essentially no standard model background to $\gamma\gamma X \not\!\!E_T$, although there is significant background from jet faking photons or mismeasured $\not\!\!E_T$. An inclusive search for $\gamma\gamma X \not\!\!E_T$, independent of X, is possible. So the specific form of cascade decays do not affect the discovery reach which depends mainly on the production cross section. Finally, the detectors have a relatively large coverage and detection efficiency for photons. In Run I CDF and DØ have searched for this mode [4, 12].

In this paper we summarize a search for anomalous production of inclusive $\gamma\gamma + \not\!\!E_T + X$ events in data corresponding to an integrated luminosity of 202 ± 12 pb^{-1} [13] of $p\bar{p}$ collisions at $\sqrt{s} = 1.96$ TeV using the CDF II detector [14]. We examine events with two isolated photons with $|\eta| \lesssim 1.0$ and $E_T^\gamma > 13$ GeV for the presence of large $\not\!\!E_T$. This work extends a previous CDF search [4] for SUSY in this channel by using an upgraded detector, a higher $p\bar{p}$ center-of-mass energy, and a larger data sample. The analysis selection criteria have been re-optimized to maximize, *a priori*, the expected sensitivity to GMSB SUSY based only on the background expectations and the predictions of the model. Similar searches for diphoton + $\not\!\!E_T$ events have been performed elsewhere [15].

We begin with a summary of the experiment apparatus and particle detection, triggers, data samples and selection criteria for the $\gamma\gamma$+$\not\!\!E_T$ final state, as well as for background estimate. The signal Monte Carlo (MC), methods for determining signal acceptance, and corrections for going from the MC to the data with an eye towards setting 95% Confidence Level (C.L.) cross section upper limit are discussed. We finally discuss the procedure for optimizing the photon E_T and $\not\!\!E_T$ thresholds to be used in limit setting, as well as the final results on the 95% C.L. lower limit on the lightest chargino and neutralino mass, $m_{\tilde{\chi}_1^\pm}$ and $m_{\tilde{\chi}_1^0}$, for the GMSB scenario.

Chapter 2

Experiment Apparatus and Particle Detection

The baby recognizes his mother's and father's voices on his very first day, from how they sounded while he was in the womb.

– in BabyTalk

The world's highest energy accelerator collides protons and anti-proton beams, and the CDF detector collects physics-quality data for this analysis. Between 1997 and 2001, both the accelerator complex and collider detector at Fermilab underwent major upgrade to increase instantaneous luminosity and take data sample of eventually 2 fb^{-1} of integrated luminosity or more. The upgraded accelerator has a shorter time between beam crossings than its predecessor: 396 ns in the current 36-bunch mode compared to 3.5 μs in the old 6-bunch mode. The new configuration required detector upgrades to ensure a maximum response time shorter than the time between beam crossings. In the following pages, we describe how the proton and anti-proton beams are produced, accelerated to their maximum center of mass energy of 1.96 TeV (Tera-electronvolt), and collided in the detector. We then describe the detector components used to identify and measure properties of the particles produced during the $p\bar{p}$ collisions.

2.1 Tevatron

The Tevatron is a superconducting accelerator at Fermilab. It accelerates and collides protons and anti-protons in a four-mile-long underground ring. The layout is shown in Figure 2.1.

The beam begins from a Cockcroft-Walton pre-accelerator [16] which accelerates H^- ions to 0.75 MeV. And the Linear accelerator (Linac) takes the H^- ions from 0.75 MeV kinetic energy to 400 MeV. The Linac has two parts: 116 MeV drift-tube (Alvarez) linac operating at 201.25 MHz and a 400 MeV side-coupled cavity linac operating at 805 MHz [17]. Because of the Linac geometry, the accelerated ions become grouped into bunches.

Then they are injected into the Booster ring (a rapid cycling synchrotron with a diameter of 74.5 m) and two electrons are removed from the H^- ions by a thin carbon foil strips, leaving protons. Successive turns of ions are injected into the same orbit as the circulating protons. The protons are accelerated to 8 GeV in the booster before they are extracted into the Main Injector (MI), which operates at 53 MHz. This is accomplished by a series of electromagnetic kicks applied by RF cavities, about 500 kV per turn.

The Main Injector accepts these protons and continues the acceleration process, increasing their energy to 150 GeV. In addition, the Main Injector accelerates a portion of the protons to 120 GeV for use in anti-proton production. Then the 150 GeV protons from the Main Injector are delivered to the Tevatron in which the magnets have superconducting coils. The Main Injector, a new element of the Run II accelerator complex, is capable of larger proton currents than its predecessor, the Main Ring, enabling a higher rate of anti-proton production.

Anti-Protons are produced by extracting the proton beam from the Main Injector to hit a nickel target, creating a multi-particle spray that contains on average 20 anti-protons per million protons, with a mean kinetic energy of 8 GeV. The anti-protons are then focused by a lithium lens and separated from other particle species by a pulsed magnet.

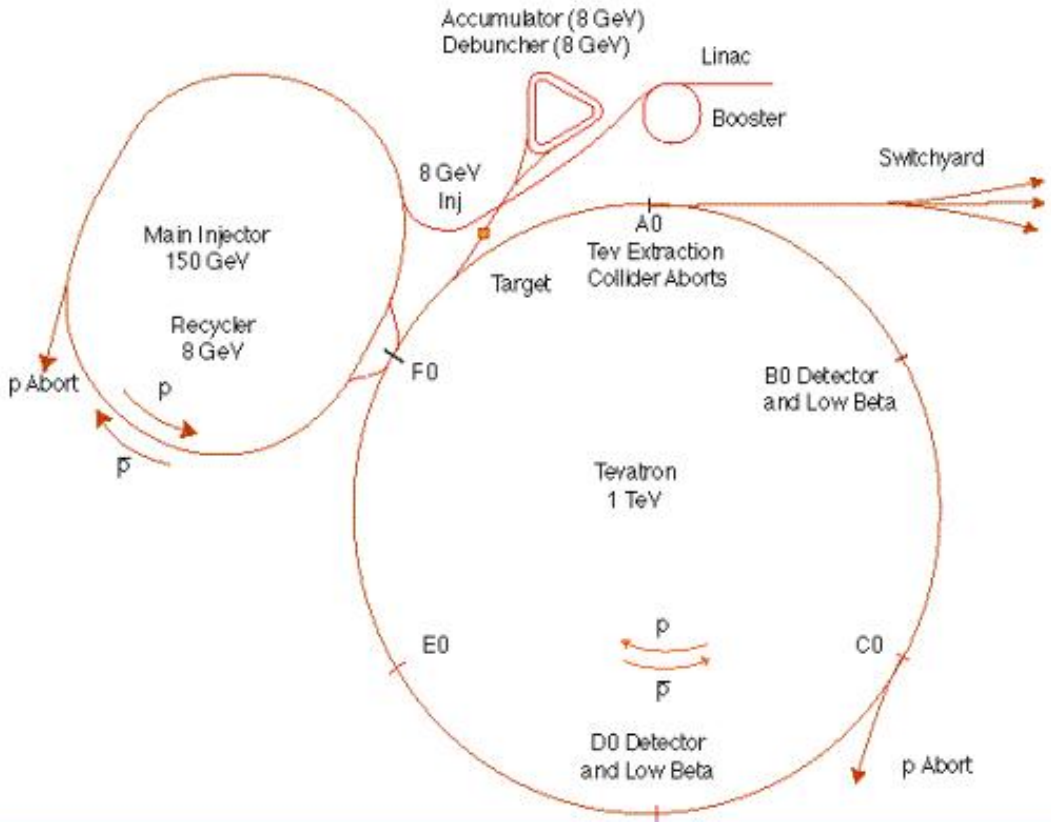

Figure 2.1: Fermilab accelerator complex.

Then the anti-protons produced in the target are accumulated in the $\bar{p}$ accumulator which actually has two rings. One is for debunching in which a rotation in synchrotron phase space is done to reduce the energy spread at the cost of increasing the time spread of the $\bar{p}$ bunch. After debunching, the $\bar{p}$'s are added to the circulating beam in the accumulator where stochastic cooling takes place to reduce the random motions of the $\bar{p}$'s: horizontal, vertical and in synchrotron phase space [18]. When enough anti-protons are circulating in the accumulator ring, they are transferred back into the MI, and are accelerated.

Over a period of 10 to 20 hours, a stack of anti-protons is built up, in preparation for a new store in the Tevatron. At the start of a store, about once per day, 36 bunches of about 3×10^{11} protons and 36 bunches of roughly 3×10^{10} anti-protons are accelerated to 150 GeV by the Main Injector, transferred to the Tevatron – the final stage of Fermilab's accelerator chain. During most of the 2002–2003 run (Run II), the Tevatron was run with "36×36". This led to an interval between beam crossings of about 396 ns. The 132 ns mode (140×105) is currently under development. The beam collisions continue typically for 8 hours.

In the collider run, protons and anti-protons are injected into Tevatron from opposite directions and accelerated up to 980 GeV. Then they collide with each other. This yields the center-of-mass energy of 1.96 TeV.

At two points around the Tevatron ("B0" and "D0") the beams are focused by quadrupole magnets to achieve the highest luminosity possible within the detectors: CDF and DØ. The instantaneous luminosity can be expressed as:

$$\mathcal{L} = \frac{f B N_p N_{\bar{p}}}{2\pi(\sigma_p^2 + \sigma_{\bar{p}}^2)} \; F\left(\frac{\sigma_l}{\beta^*}\right) \tag{2.1}$$

where f is the revolution frequency at which proton or anti-proton travel around the Tevatron, which is about 70 kHz. B is the number of bunches, which is 36 now. $N_{p/\bar{p}}$ are the numbers of particles in proton and anti-proton bunches, typically about the order of 10^{11} and 10^{10} respectively. $\sigma_{p/\bar{p}}$ are the rms beam size at the interaction point. F is a form factor which depends on the ratio of σ_l, the bunch length, to β^*, the beta function at the interaction point.

Run	Ib	IIa
protons/bunch	2.3×10^{11}	2.7×10^{11}
anti-proton/bunch	5.5×10^{10}	3.0×10^{10}
total anti-protons	3.3×10^{11}	1.1×10^{12}
proton emittance (mm-mrad)	23π	20π
anti-proton emittance (mm-mrad)	13π	15π
β^*	35	35
anti-proton bunches	6	36
bunch length (m)	0.6	0.37
bunch spacing (ns)	3500	396
interactions/crossing	2.5	2.3

Table 2.1: Parameters describing the accelerator configuration in Run I and II. The Run Ib column shows typical operating parameters during 6×6 bunches. The Run IIa column shows projections for 36×36 operation.

The beta function is a measure of the beam width, and is proportional to the beam's x and y extent in phase space. Anti-Proton availability is the most limiting factor for attaining high luminosities. The proton and anti-proton beams circulating in the Tevatron are unpolarized, and bunches exhibit a longitudinal density profile such that the resulting distribution of collisions along the beam axis is Gaussian, with a width of about 30 cm.

The average instantaneous luminosity of data is used 2×10^{31} cm^{-2} s^{-1} for this analysis. Since the start of physics–quality data taking at CDF in April, 2002, the Tevatron has delivered 330 pb^{-1} to CDF until October, 2004, of which approximately 200 pb^{-1} is declared to be good for this analysis. See Figure 2.2, 2.3 and 2.4 for integrated luminosity and data taking efficiency so far achieved. The Tevatron has broken 10^{32} cm^{-2} s^{-1} barrier at June, 2004, shown in Figure 2.5. Table 2.1 shows a comparison of Run I and Run II accelerator parameters.

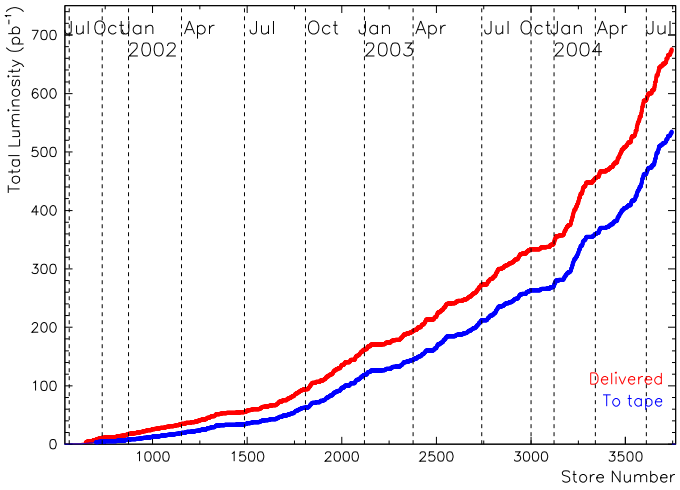

Figure 2.2: Integrated luminosity delivered (upper line) and recorded (lower) at CDF so far, as functions of $p\bar{p}$ stores and time [19]. It began to take physics-quality data at April, 2002.

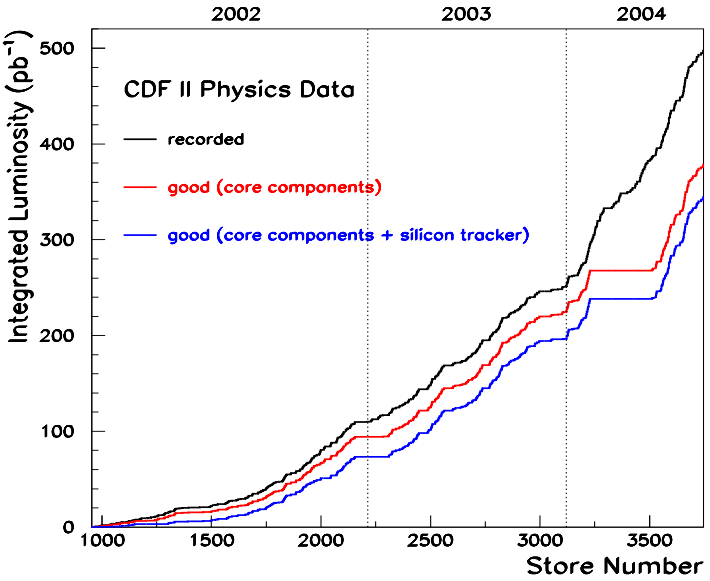

Figure 2.3: The summary of the integrated luminosity recorded at CDF so far, as functions of $p\bar{p}$ stores and time. The upper line shows all recorded, the middle line indicates that core components of CDF detector are good working, and the lower line when core components plus silicon tracker are good working.

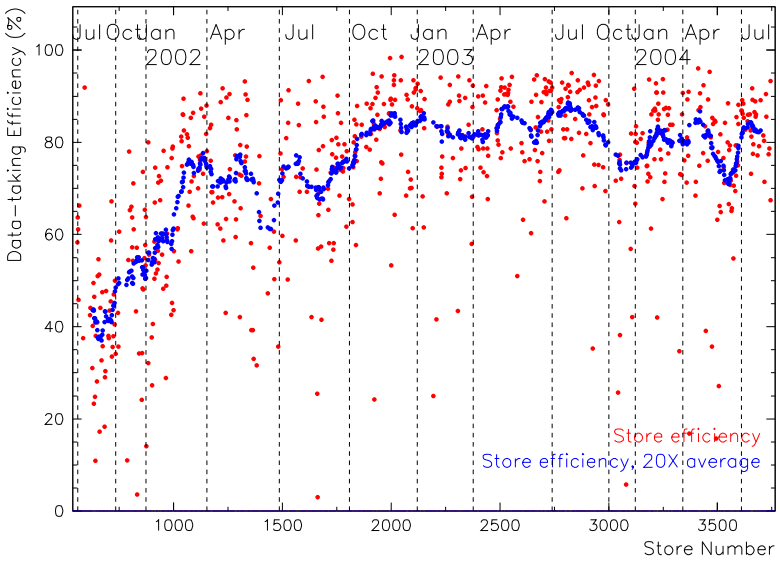

Figure 2.4: Data taking efficiency as functions of $p\bar{p}$ stores and time. It is a level of 80 to 90%. The inefficiency comes from trigger overflow, detector problem, high-voltage reconfiguration and so on.

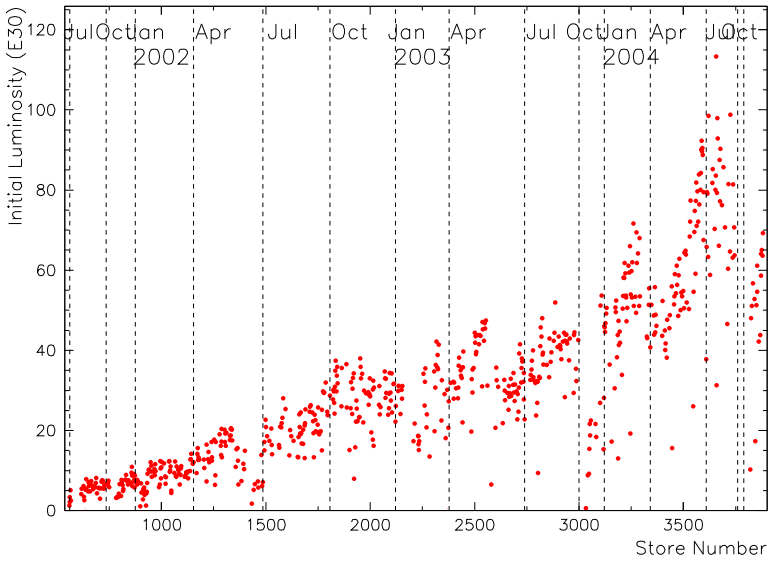

Figure 2.5: The initial instantaneous luminosity as functions of $p\bar{p}$ stores and time. The Tevatron has broken 10^{32} cm^{-2} s^{-1} barrier at June, 2004.

2.2 Collider Detector at Fermilab

The CDF detector is an azimuthally and forward-backward symmetric magnetic detector designed to study $p\bar{p}$ collisions at the Tevatron. The magnetic spectrometer consists of tracking devices inside a 3-m diameter, 5-m long superconducting solenoid magnet which operates at 1.4 T.

The CDF detector is a general purpose particle detector. It consists of a 2000-ton central detector with the superconducting solenoidal magnet, steel yoke, tracking chambers, electromagnetic calorimeters, hadron calorimeters and muon chambers, time-of-flight systems, and identical forward/backward detectors. The central detector can be rolled out of the collision hall for maintenance and upgrade during non-collider operation.

The major function of this detector is to measure the energy, momentum, and, where possible, the identity of the particles produced during the proton-antiproton collision.

A brief description to the components related to this thesis is given below. The detailed description of the individual detector component can be found in various papers [14]. A schematic drawing of the major detector components is shown in Figure 2.6.

In the detector coordinate system commonly used at CDF, we choose z axis along the proton beam direction (East) with zero at the detector center, y axis upward and x axis towards outside of the Tevatron ring (North). We use R as the distance to the beam line in cylindrical coordinates; ϕ is the azimuthal angle, and θ is the polar angle relative to the positive z-axis in spherical coordinates. Since hadrons are composite objects, daughter particles from a $p\bar{p}$ collision are often produced with significant momentum along the z axis. It is thus useful to define two variables, rapidity and pseudorapidity: The rapidity, which is defined as:

$$y = \frac{1}{2} \ln\left(\frac{\mathrm{E} + \mathrm{p_z}}{\mathrm{E} - \mathrm{p_z}}\right) \tag{2.2}$$

is often used instead of the polar angle θ in the laboratory coordinate frame.

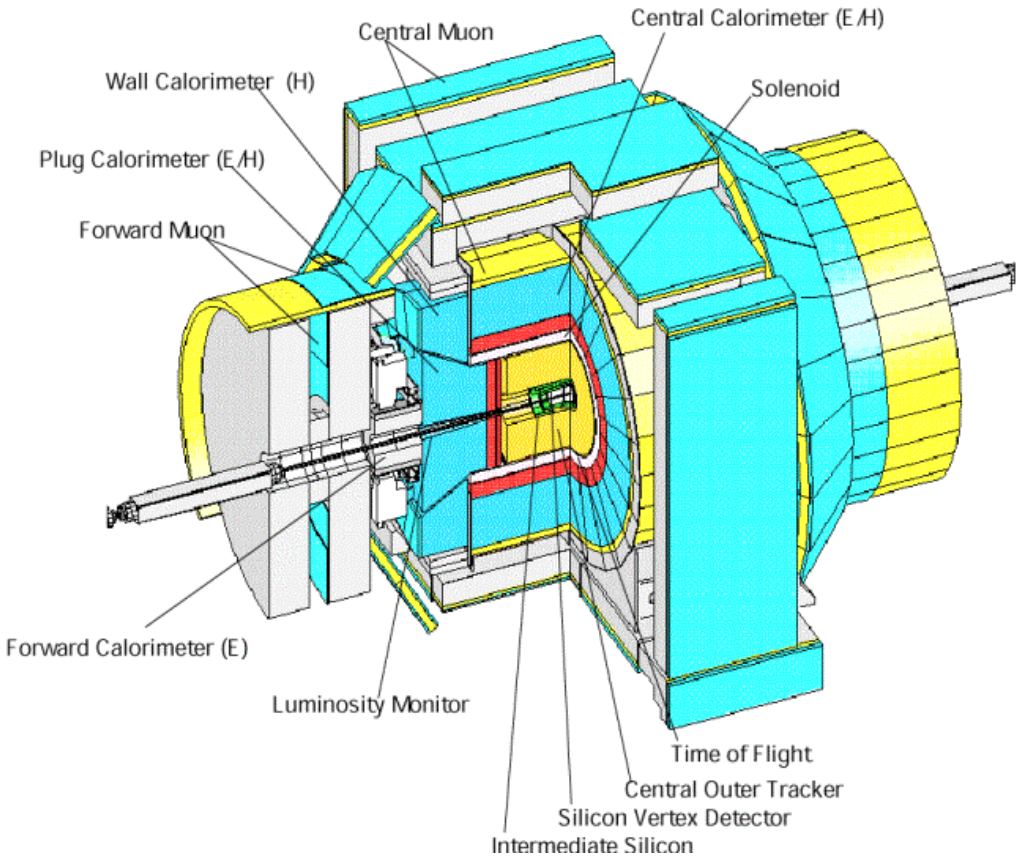

Figure 2.6: A schematic view of the CDF Run II Detector. The solenoid is located between the Central Outer Tracker and the Central Electromagnetic calorimeter. In the central region the existing solenoid and scintillator-based calorimeter were retained from Run I. On each "end" of CDF, the plug and forward ($|\eta| > 1$) calorimeters were replaced with one new end-plug calorimeter.

The advantage of rapidity is that a change of rapidity is a constant $\delta y = \theta \equiv \tanh^{-1}\beta$ under a boost in z direction with velocity $\beta \equiv v/c$. For the case where $E \gg m$, the rapidity can be approximated by pseudo-rapidity:

$$\eta = \frac{1}{2}\ln\left(\frac{\mathrm{E} + \mathrm{p_z}}{\mathrm{E} - \mathrm{p_z}}\right) = -\ln\left(\tan\frac{\theta}{2}\right) \tag{2.3}$$

The interaction point at CDF is not at the coordinate (0,0,0), however, it is assumed that the reconstructed default track at CDF is from (0,0,0). So the pseudorapidity calculated from default track is called detector pseudorapidity.

$|\eta|$ extends from 0 at the perpendicular to the beampipe to approximately 3.5 at the most forward part of the detector. The central portion of the detector spans $0.0 \lesssim |\eta| \lesssim 1.0$, while the forward (plug) detector is located at $1.0 \lesssim |\eta| \lesssim 3.0$. Sub-detectors are placed radially at varying distances from the collision point. Starting from the beampipe and expanding outward one finds the tracking system, calorimetry systems, and muon systems.

2.2.1 Cerenkov Luminosity Counter

At hadron collider experiments the beam luminosity, traditionally, has been measured using the process of inelastic $p\bar{p}$ scattering. It has a large cross-section, $\sigma_{in} \sim 60$ mb, measured at the Tevatron energy (1.96 TeV) by the CDF, with an uncertainty of $\sim 6\%$. The rate of inelastic $p\bar{p}$ interactions is given by [20]:

$$\mu \cdot f_{BC} = \sigma_{in} \cdot \mathcal{L} \tag{2.4}$$

where $\mathcal{L}$ is the instantaneous luminosity, f_{BC} is the rate of bunch crossing in the Tevatron, μ is the average number of $p\bar{p}$ interactions per bunch crossing.

To detect inelastic $p\bar{p}$ events[1] efficiently a dedicated detector at small angles, operating at high rate and occupancy, is required. In Run II the Cerenkov Luminosity Counters (CLC) are being used by CDF to measure the Tevatron luminosity. The CLC is designed to measure μ accurately (within a few per-

[1]The CLC has zero acceptance for elastic $p\bar{p}$ events.

cent) all the way up to the high luminosity regime $\mathcal{L} \sim 2 \times 10^{32}$ cm^{-2} s^{-1} expected in Run II [14].

There are two CLC modules in the CDF detector, installed at small angles in the proton (East) and anti-proton (West) directions with rapidity coverage between 3.75 and 4.75. Each module consists of 48 thin, long, gas-filled, Cerenkov counters. The counters are arranged around the beam-pipe in three concentric layers, with 16 counters each, and pointing to the center of the interaction region [21]. The Cerenkov counters are not sensitive to beam halo[2], photons or neutrons, nor to soft charged particles which fall under the Cerenkov threshold.

2.2.2 Tracking Systems

There are two primary tracking detector systems in CDF Run II. The inner tracking system of a 90-cm long silicon micro-strip vertex detector, consisting of one single–sided layer and six double–sided layers, with an additional double-sided layer at large η, surrounds the beam pipe [23]. Outside the silicon detector, a 3.1 meter long drift chamber with 96 layers of sense wires, the Central Outer Tracker (COT), is used with the silicon detector to determine the momenta of charged particles and the z position of the $p\bar{p}$ interaction (z_{vertex}) [24].

Detection and tracking of charged particles is an essential part of event analysis at CDF. Trackers provide two fundamental kinds of measurement. On one side, they determine the direction and curvature of a particle's path; on the other, they delimit a narrow region where the particle might have been produced.

Charged particle moving in a uniform magnetic field, as inside the CDF tracker, have a helicoidal trajectory. By measuring the radius of curvature of the helix, one obtains the particle's transverse momentum; the longitudinal momentum is related to the helix pitch. This information can be used in

[2] See Reference [22] for a measure of beam halo and losses using the installed arrays of scintillation counters on both sides of the CDF detector.

several ways: as a requirement in a trigger, during particle identification, in order to calibrate the calorimeters.

To obtain a precise measurement of the helix radius and pitch, it is necessary to sample points of the trajectory which are spread on a long lever arm. Therefore, a good spectrometer requires a large tracking volume.

On the other hand, by taking a few, very accurate measurements of the track position near the primary interaction point, it is possible to narrow the region of space in which a given particle was originated. By intersecting such regions, it is possible to determine which (if any) particles were produced in a secondary vertex, trigger on their existence, and measure the mass and lifetime of short-lived particles.

Secondary vertex detection does not require a large lever arm; the most important issues are the detector's closeness to the vertex and its ability to withstand a high density of tracks.

The CDF II tracking system, shown in Figure 2.7, fulfills both kinds of requirements by combining different detector elements. Momentum of tracks in the central region ($|\eta|$<1) is measured with an open-cell drift chamber, the COT, extending radially between 40 and 138 cm; several layers of micro-strip silicon wafers (SVX II and Layer 00) provides three-dimensional vertexing at radial coordinates below 10 cm; lastly, another silicon micro-strip detector (ISL) is used to track particles in the forward region, which is not adequately covered by the COT.

The silicon tracker is used not only to precisely reconstruct the track impact parameter or interaction points, but also to be able to perform the silicon stand-alone tracking for the region ($1.0 < |\eta| < 2.0$) which is not covered by the COT.

The COT covers the central region in the range $|\eta| \lesssim 1.0$ with the purpose of the high tracking resolution and reconstruction efficiency. The COT measure dE/dx for charged particles which is useful for particle identification [25]. The transverse momentum resolution is $\delta p_T/p_T^2 < 0.15\%$ $(\mathrm{GeV/c})^{-1}$.

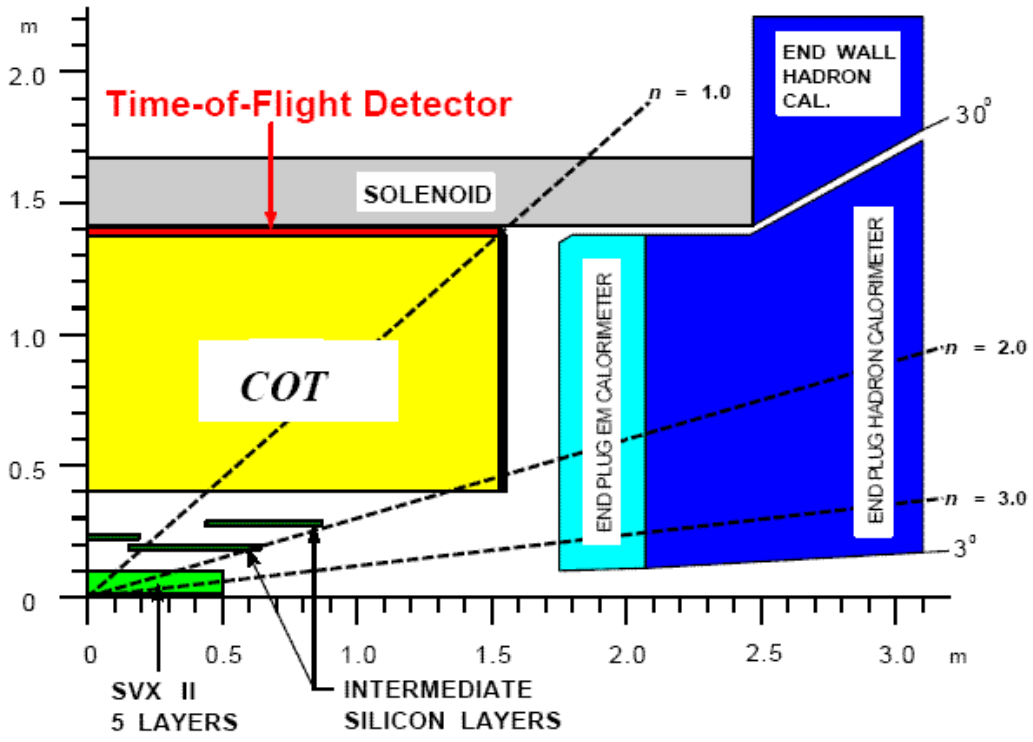

Figure 2.7: Side view of the central region of the CDF II detector (quarter section), showing the Tracking System which is cylindrically symmetric. Layer 00 is missing from the illustration.

2.2.3 Time-of-Flight Systems

Right outside of tracking systems, there is the Time-Of-Flight (TOF) detector which measures the time-of-flight of particles and it is very useful for particle identification in the Λ_b lifetime measurement [26].

The TOF detector has been added to the CDF II detector to enhance the particle identification [27]. The primary goal is to provide a 2σ separation between $\pi^{\pm}$ and $K^{\pm}$ for momentum $p < 1.6$ GeV/c^2. By combining it with dE/dx it is expected to improve the neutral B meson flavor determination. Another purpose of TOF detector is to search for highly ionizing particle-monopole [28]. Since the mass difference between pion and proton is even bigger than the difference between pion and Kaon, the particle identification ability of selecting proton from pion by combining TOF and dE/dx together is very powerful in Λ_b lifetime measurement.

2.2.4 Superconducting Solenoid Magnet Coil

The superconducting solenoid magnet coil is made of an aluminum-stabilized NbTi/Cu superconductor. It provides a uniform 1.41 T magnetic field along the incident beam direction in the COT region.

The CDF calorimeter systems are located outside the solenoid with two separated devices of the electromagnetic (EM) and hadronic (HA) calorimeters where hadron, electron, photon deposit most of their energy. This is useful to identify electrons and photons. Unlike hadrons and electrons, muons only deposit minimum ionization energy in the calorimeters, so muon system outside the calorimeter is used to identify muon. In addition, there are the Central Pre-Radiator (CPR) and Central Electromagnetic Strip (CES) chambers. Both CPR and CES are used to discriminate between a signal photon and background from a neutral pion decay to $\gamma\gamma$.

2.2.5 Calorimeters

Calorimetry has played a crucial role in the physics CDF has produced: the top mass discovery, the precision measurement of the W mass, photon and jet measurements over many orders of magnitude, and searches for new phenomena have all exploited the excellent behavior of the calorimeters. In the upgraded detector the existing scintillator-based calorimeter was retained within central region, but its electronics needed to be replaced due to the shorter bunch spacing. On each "end" of CDF, the plug and forward ($|\eta| > 1$) calorimeters were replaced with one new end-plug calorimeter. The system promises an exceptional increase in compactness, hermiticity, radiation hardness, and speed over the present system.

The solenoid and tracking volumes of CDF are surrounded by calorimeters, which cover 2π in azimuth and $|\eta| \leq 3.6$. The central electromagnetic (CEM) calorimeter covers $|\eta| \leq 1.1$ and is followed at a larger radius by the central hadronic calorimeters (CHA and WHA), which cover $|\eta| \leq 1.3$. These calorimeter use scintillator as the active medium. The CEM absorber is lead and the CHA/WHA absorber is iron. The calorimeters are segmented into units of 15 degrees in azimuth and 0.1 pseudorapidity. Two phototubes bracket each tower in ϕ, the average of the energy in the two tubes is used to determine the ϕ position of energy deposited in a tower.

The calorimeter is made up of wedges, or "physical towers", measured in $\eta - \phi$ coordinates. Each tower uses a series of absorber and scintillator layers. Scintillator light is collected by a light pipe and a wavelength shifter that directs the energy into a photomultiplier tube (PMT). An $r - z$ view of the detector shows the calorimeter wedges arranged as if a ϕ cut into slices, with each slice pointing back toward the interaction point. The central portion of the calorimeter has towers that span 15° in ϕ and 0.11 in units of η, while plug calorimeter towers span either 15° or 7.5° in ϕ, and varying ranges in η.

The CEM uses a hybrid design. It consists of the lead and scintillator layers with an embedded strip chamber approximately at the depth of maximum particle multiplicity for electromagnetic showers. The scintillator provides a

good energy resolution and the strip chamber provides the position determination and transverse development at the shower maximum. The average energy resolution of the CEM is

$$\frac{\sigma(E)}{E} = \frac{13.5\%}{\sqrt{E_T}} \oplus 2\% \text{ (added in quadrature)}, \tag{2.5}$$

where $E_T = E \cdot \sin\theta$ (E in GeV).

The CHA and WHA are made of steel and scintillator. The interaction length of both the CHA and WHA is 4.5 λ_0. The CHA has 32 layers with 2.5 cm sampling, and the WHA has 15 layers with 5.0 cm sampling. For hadrons, the single-particle resolution depends on angle and varies from roughly $50\%/\sqrt{E}$ plus 3% added in quadrature in the CHA to $75\%/\sqrt{E}$ plus 4% added in quadrature in the WHA.

For Run II, there is new plug calorimeter, with variable tower size, which extends coverage out to $|\eta| = 3.6$. The plug electromagnetic calorimeter (PEM) covers both ends of the superconducting magnet coil. Each of them are made of four quadrants of $\delta\phi = 90°$. And each of the quadrants consists of 34 layers of proportional tube arrays interleaved with 2.7 mm thick lead absorber panel filling about 50 cm in depth. The plug hadronic calorimeter (PHA) has 20 layers of steel and proportional tubes. Each energy resolution of PEM and PHA is about 16% and 80%. The PEM contains an embedded position detector at shower maximum to improve electron identification and π^0/γ separation. In addition, the first layer of the PEM may be read out separately as a pre-shower detector.

2.2.6 The CPR and CES chambers

The central calorimeter is segmented into 48 independent wedge modules. The full central detector is constructed of two rings of 24 wedges each that make contact at $z = 0$. Each wedge subtends 15° in azimuth and approximately one unit in η. Both CPR and CES chambers are segmented into two halves in CDF z coordinates.

A system of proportional wire chambers in front of the central electromagnetic calorimeters (the CPR system) uses the one-radiation-length-thick magnet coil as a 'preradiator' to determine whether showers start before the calorimeter [29]. Wire chambers with cathode strip readout (the CES system), located at shower maximum in the central electromagnetic calorimeter, give 2-dimensional profiles of showers.

The CPR chambers' perpendicular distance to beam line is 168 cm. Inside each CPR chamber the wires running along z directions are split about the middle of z. They are 16 wires at low $|z|$ (7.9 $\sim$ 119.7 cm), and 16 at high $|z|$ (123.5 $\sim$ 235.3 cm) for a total of 32 in one wedge.

The CES chambers' perpendicular distance to beam line is 184 cm. The CES anode wires measure ϕ and cathode strips measure η. Inside each chamber the wires running along z directions are split in the middle in z (121.2 cm). They are 32 wires at low $|z|$ (0.2 $\sim$ 121.2 cm), and 32 at high $|z|$ (121.2 $\sim$ 239.6 cm) for a total of 64 in one wedge. The strips are slightly different pitch in low and high $|z|$. There are the 69 z strips at low $|z|$ and 59 at high.

2.2.7 Muon Chambers

The muon detectors are located outside of the calorimeter, at the furthest reaches of the detector. Muons are minimum ionizing particles, which means they are capable of travelling through many interaction lengths before losing their energy and stopping.

CDF uses the steel in the calorimeter, the magnet return yoke, and additional steel shielding to stop all other charged particles from entering the muon detectors. The muon chambers record hits from the path of the muon through the detector. This information, combined with tracks in the COT, results in an excellent muon identification, as well as, rejection of cosmic background.

The muon detectors are four systems of scintillators and proportional wire chambers which extend out to $|\eta| \leq 2.0$. They are, moving outward from the interaction point: central muon (CMU), central muon upgrade (CMP), central muon extensions (CMX/CSX), and intermediate muon (IMU) detectors.

The rapidity coverage of the muon detectors are summarized as following:

- The CMU and CMP extend out to $|\eta|$ of 0.6.
- The CMX spans a range of $0.6 \leq |\eta| \leq 1.0$.
- The IMU finalizes the coverage from $1.0 \leq |\eta| \leq 2.0$.

2.3 Trigger and data acquisition systems

The trigger system is the important component for detector at hadron collider. It is impossible to record all events produced during the $p\bar{p}$ collisions. A typical event size is 250 kB. At the 2.5 MHz beam crossing rate, the system would have to be capable of recording 625 GB/s. This is assuming that there is an interaction every beam crossing, which is not unreasonable, described as an average of 2.3 interactions per crossing in Table 2.1.

We are interested in events containing particles with large transverse energy. This reflects hard scattering of quarks in the protons and anti-protons. The uninteresting inelastic events, called "minimum bias", occur ten orders of magnitude more frequently than $t\bar{t}$ events, and four order of magnitude more often than events with b's. Currently, the maximum event rate to disk is $\approx$ 70 Hz. If events were selected randomly, we would have no chance of acquiring interesting data samples large enough to make precise measurements or to approach new physics.

The complex system of digital electronics called the trigger allows the experiment to decide, in a very short amount of time, whether an event is interesting enough to record or not. It is of the utmost importance that the decision is fast, so that collisions are not missed while the trigger is thinking about its decision.

There are three trigger paths at CDF trigger system so that a data acquisition system (DAQ) efficiently consumes the collision events within a 132 ns

bunch-crossing rate. [3] Since all the events cannot be stored, only the interesting events are selected by triggers. In each trigger step, the data size is reduced according to that triggering ability: 40 kHz acceptable rate at Level-1, 300 Hz for Level-2, and 30-50 Hz at Level-3 trigger stage.

Figure 2.8 shows the functional block diagram of the readout electronics. To accommodate a 132 ns bunch-crossing time and a 4 μs decision time for the first trigger level, all front-end electronics are fully pipelined, with on-board buffering for 42 beam crossings. Data from the calorimeters, the central tracking chamber, and the muon detectors are sent to the Level-1 trigger system, which determines whether a $p\bar{p}$ collision is sufficiently interesting to hold the data for the Level-2 trigger hardware. See Figure 2.9 for details. The Level-1 trigger is a synchronous system with a decision reaching each front-end card at the end of 42-crossing pipeline. Upon a Level-1 trigger accept, the data on each front-end card are transferred to one of four local Level-2 buffers. The second trigger level is an asynchronous system with an average decision time of 20 μs. A Level-2 trigger accept flags an event for readout. Data are collected in DAQ buffers and then transferred via a network switch to a Level-3 CPU node, where the complete event is assembled, analysed, and, if accepted, written out to permanent storage. These events can also be viewed by online monitoring programs running on other workstations.

All events accepted by Level-2 trigger are collected in the Event Builder (EVB), and then the EVB assembles those event fragments into one data block and delivers it to the Level-3 trigger system. The Level-3 trigger system is a farm of parallel processors which operate on a Linux PC, where a full event reconstruction is implemented in software. After passing through the Level-3 trigger, the Data Logger system delivers events to the tape device or online monitoring processes. The Level-3 reconstruction program is written in C++ with object-oriented techniques. The same reconstruction program is used in the offline event analysis.

[3] In the period of data taking considered in this analysis, the accelerator was operating in 35 bunches mode (beam crossing interval of 396 ns) and the trigger was clocked every 132 ns with the two intermediate clock cycles automatically rejected.

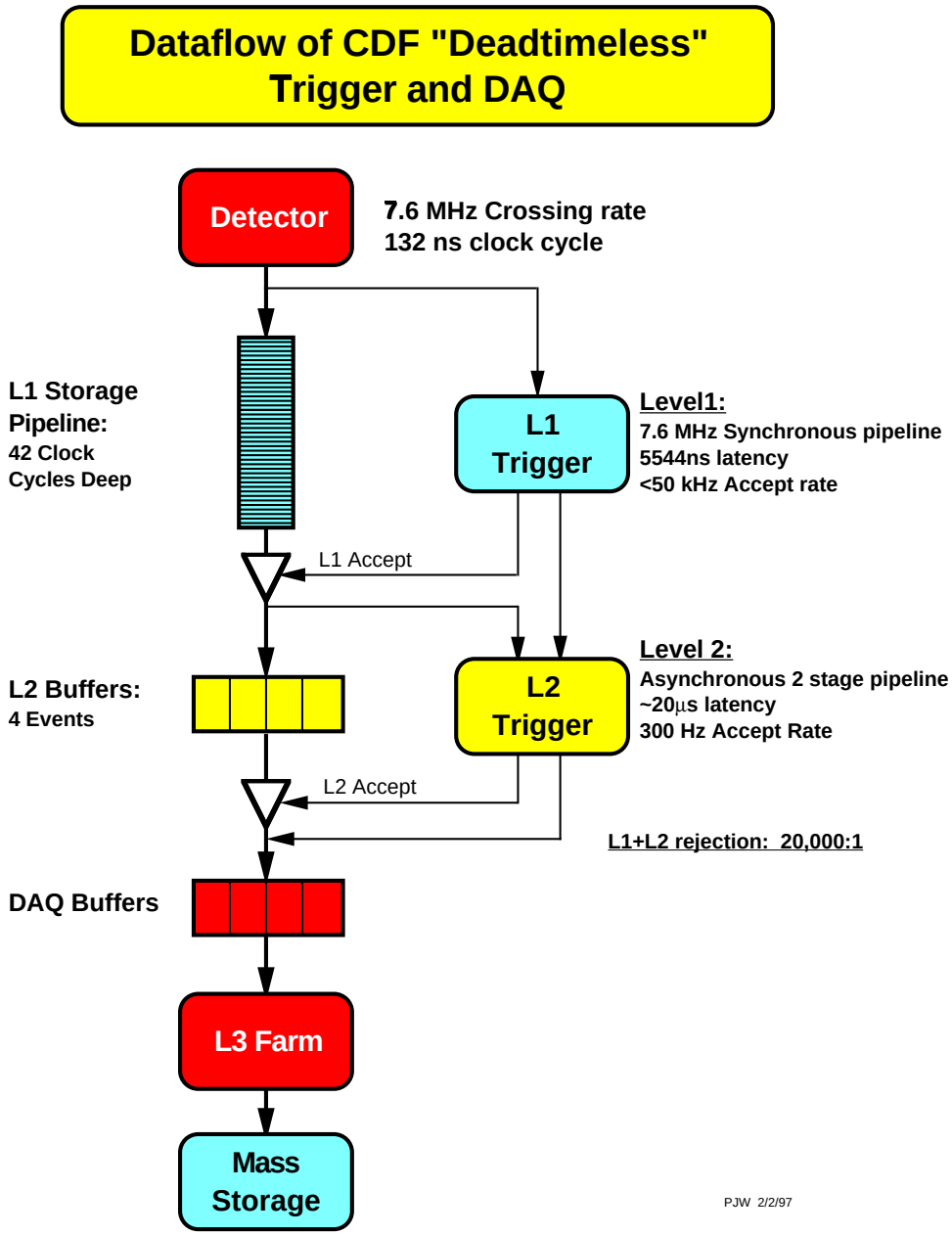

Figure 2.8: Trigger System Flowchart for CDF. This diagram shows the maximum rate which the trigger system was designed to handle. We are currently running at a 2.5 MHz input rate into Level-1, and a 20 kHz output rate from Level-1.

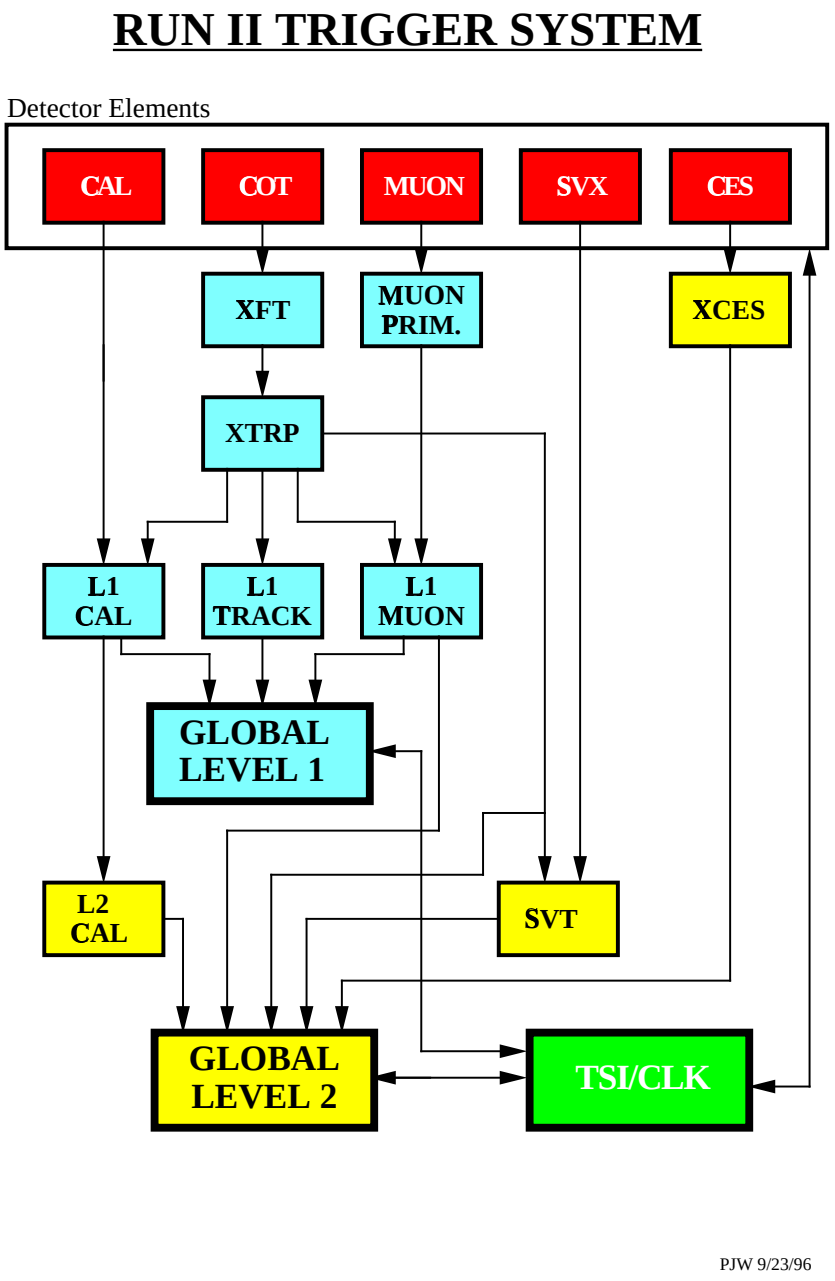

Figure 2.9: Block diagram of the Run II trigger system at CDF.

Chapter 3

Triggers, Data Samples and Selection Cuts

The baby is now showing rapidly increasing interest in speech and regularly looks around for, and successfully locates, speakers. He can differentiate between angry and friendly voices.

`- in BabyTalk (the 3rd month)`

The data used in this analysis were collected during 2002–2003 Tevatron Run II, corresponding to 202 pb^{-1} of total integrated luminosity. We used the database offline luminosity for all runs after the DQM "`Good Runs`[1]" version 4.0 [30] were selected, and scaled up by multiplying by 1.019 which corresponds to a $p\bar{p}$ inelastic cross section of 60.7 mb. The uncertainty in the luminosity is of the order of 6% [13].

[1]Good runs were required to have the "good run core components" bit set by the shift crew, and the CAL, COT, CMU and CMP offline marked as good. Each run was also required to have an integrated luminosity of greater than 10 nb^{-1}.

3.1 Trigger Requirements

The majority of the data studied in this analysis, both signal and background samples, was selected online for the presence of two electromagnetic clusters where both of have either $E_T > 12$ GeV and are isolated (`DIPHOTON_12`), or both have $E_T > 18$ GeV with no isolation requirement (`DIPHOTON_18`). Table 3.1 summarizes the cuts in the diphoton trigger paths. When a different dataset or trigger path is used, it will be described separately.

We have processed the full inclusive diphoton dataset; `cph208` and `cph209`. The events were reconstructed using production offline version `4.8.4`, and most major objects were reprocessed and "ntuplised" using offline version `4.11.2` and Stntuple version `dev_240`.

`DIPHOTON_12`	
L1	Single tower $E_T > 8$ GeV ($z = 0$) Single tower Had/EM< 1.25 or $E_T > 14$
L2	Two high E_T pass clusters, $E_T > 10$ ($z = 0$), $\eta < 3.6$ Both clusters Had/EM < 1.25 Both clusters Iso < 3 || Iso $< 0.15E_T$
L3	Two L3 clusters, $E_T > 12$ ($z = 0$) Both clusters Had/EM $< 0.055 + 0.00045E$ || $E_T > 200$ Both clusters Iso(cone 0.4) < 2 || $< 0.10E_T$ for central, average and scaled CES $\chi^2 < 20$
`DIPHOTON_18`	
L1	Single tower $E_T > 8$ GeV ($z = 0$) Single tower Had/EM< 1.25 or $E_T > 14$
L2	Two high E_T pass clusters, $E_T > 16$ ($z = 0$), $\eta < 3.6$ Both clusters Had/EM< 1.25
L3	Two L3 clusters, $E_T > 18$ ($z = 0$) Both clusters Had/EM $< 0.055 + 0.00045E$ || $E_T > 200$ for central, average and scaled CES $\chi^2 < 20$

Table 3.1: The cuts in the diphoton triggers use to create the diphoton sample.

3.2 Diphoton Dataset Event Selection

The backgrounds to the $\gamma\gamma + \not\!\!E_T$ search are dominated by QCD ($\gamma\gamma$, $\gamma - jet$ and $jet - jet$) + fake $\not\!\!E_T$ backgrounds, $e - \gamma$ type backgrounds with real $\not\!\!E_T$, and non-collision backgrounds such as from cosmic rays, beam-halo and beam-gas interactions. To suppress these backgrounds we select diphoton candidate events using four selection criteria; global event selection, standard photon identification, cosmic and halo rejection, and $\not\!\!E_T$ cleanup cuts. Table 3.2 summarizes the event selection cuts, and we describe the cut variables below.

After requiring the .OR. of the two diphoton trigger paths in Table 3.1 and the DQM version 4.0 "`GoodRun`" bit, we require a `ZVertexColl` vertex of any quality, selecting the highest Σp_T vertex (sum of the transverse momenta of tracks in the vertex, which comes from defTracks) if there is more than one, and require it vertex to have $|z_{\rm vertex}| < 60$ cm. We find 96% of events containing two good photons have a $z_{\rm vertex}$, and then the z cut reduces this to 92%. There are 665,549 events in this sample.

Both photons are required to pass the standard photon identification requirement (baseline analysis cuts for high p_T photons version 2.1) as defined by the photon group. For more information on the definitions of the cuts see Ref. [31]; each is summarized in Table 3.2 and in more words below. A sample of 3,546 diphoton events pass the standard photon identification requirements:

- Two central electromagnetic clusters with corrected transverse energy $E_T^\gamma > 13$ GeV [32] (where the 12 GeV trigger becomes $> 99.7\%$ efficient [33]).

- The fiducial part of the detector, defined by $|\mathrm{CES}x| < 21.0$ cm in the CES local coordinate and $9.0 < |\mathrm{CES}\ z| < 230.0$ cm in the CDF coordinate.

- No tracks (N3D), or only one N3D with $p_T < 1.0{+}0.005 E_T^\gamma$ GeV, pointing at either cluster (to remove electrons), where N3D is the number of tracks associated with the cluster.

- The ratio of the hadronic to electromagnetic energy in the cluster is required to have Had/EM $< 0.055 + 0.00045E^{\gamma}$ (to reject jets).

- Isolation requirements; candidates are required to be isolated in the calorimeter and tracking chamber to reject hadronic backgrounds which fake prompt photons. In the calorimeter the isolation is defined as the energy in a cone of 0.4 in $\eta - \phi$ space[2], minus the photon cluster energy, and corrected for energy loss into cracks as well as the number of vertices in the event. We require isolation $< 0.1 \times E_T$ for $E_T < 20$ GeV, and < 2.0 GeV $+ 0.02 \times (E_T - 20$ GeV), above. In the tracking chamber we require the scalar sum of the p_T of all tracks in the 0.4 cone to be < 2.0 GeV $+ 0.005 \times E_T$.

- A χ^2 is obtained by comparing the observed lateral shower shape in the CES strips and wires with the predicted shape based on test beam. We require the averaged and scaled $\chi^2 < 20$ to remove π^0 backgrounds.

- To further remove π^0 backgrounds we require no other strip or wire CES clusters[3] with $E_T > 0.14E_T^{\gamma}$ for $E_T < 18$ GeV, or $> 2.4 + 0.01E_T^{\gamma}$ for $E_T > 18$ GeV.

After the standard photon identification cuts, there is still some contamination from non-collision sources such as cosmic rays, beam-halo or beam-gas interactions in the data sample. To reduce backgrounds which are not from the collision, in general, we require that the hadron TDC results are consistent with no energy out-of-time: we reject any event which has a tower above 500 MeV which is 3σ out-of-time as defined in Ref. [34]. Further rejection against events where the photons are not from the collision is gained by rejecting the event if the $\not\!\!E_T$ (which is also spurious) is approximately equal in magnitude

[2]That is, $\Delta\mathcal{R} \equiv \sqrt{\Delta\eta^2 + \Delta\phi^2} = 0.4$.

[3]The highest energy of secondary highest strip or wire is chosen. If only the strips or wires have a secondary cluster, place the cut on the available one, if neither have a second cluster, it passes. The $\sin\theta$ of photon corrects for the path length through the CES detector. It does not make the quantity transverse and CES energies have strip/wire corrections ($E_{\rm CES} = E_{\rm CES} \cdot \sin\theta$).

Global Event Selection
DIPHOTON_12 or DIPHOTON_18 trigger paths
DQM Version 4.0 GOOD RUN bit
z_{vertex} exists, $\lvert z_{vertex}\rvert < 60$ cm
Standard Photon Identification
Central
$E_T^\gamma > 13$ GeV
$\lvert$CES $x\rvert < 21.0$ cm
$9.0 < \lvert$CES $z\rvert < 230.0$ cm
Had/EM $< 0.055 + 0.00045E^\gamma$
CalIso(cone 0.4) $< 2.0 + 0.02 \times (E_T^\gamma - 20)$ for $E_T^\gamma > 20$ GeV
$\lvert\rvert$ CalIso $< 0.1E_T^\gamma$ if $E_T^\gamma < 20$ GeV
Average and scaled CES $\chi^2 < 20$
N3D= 0 $\lvert\rvert$ N3D= 1 and $p_T < 1.0 + 0.005E_T^\gamma$
Σp_T(cone 0.4) $< 2.0 + 0.005E_T^\gamma$
$E_{\text{2nd CES cluster}} < 2.4 + 0.01 \times E_T^\gamma$ for $E_T^\gamma > 18$ GeV $\lvert\rvert < 0.14E_T^\gamma$ if $E_T^\gamma < 18$
Cosmic and Halo Cuts
HADTDC method: No towers with 0.5 GeV and 3σ out-of-time
For photons which have $0.8 < \lvert \not\!\!E_T/E_T^\gamma \rvert < 1.2$ and $\Delta\phi(\not\!\!E_T - \gamma) > 2.9$)
1) Sidewedges cut
2) HaloEast + HaloWest ≤ 1
3) No muon stubs within 30°
$\not\!\!E_T$ cleanup cuts
$10° < \Delta\phi(\not\!\!E_T$–jet$) < 170°$ (for any raw jet $E_T > 10$ GeV)

Table 3.2: The diphoton signal sample event selection cuts. For more information on the photon ID variables, HADTDC and beam halo cuts, see Refs. [31, 34, 35]. Note that the $\Delta\phi$ cut assumes the corrected ϕ position of the $\not\!\!E_T$ (see Section 3.4), and that jets are defined with a cone size of $\Delta R = 0.4$ with no η restriction. As discussed in Chapter 6, after optimization, the final $\not\!\!E_T$ cut is 45 GeV. Note that if both photons are in the same wedge and the vector sum of their E_T is equal and opposite to the $\not\!\!E_T$, as might be the case from beam-halo, then we also require the event to pass the cosmic/halo cuts.

and opposite in direction to either photon and there is evidence of cosmic-ray interactions or beam-halo contributions. We following the cuts in Ref. [35] and remove these events as described in Table 3.2. If both photons are in the same wedge and the vector sum is equal and opposite to the $\not\!\!E_T$, as might be the case from beam-halo, then we also require the event to pass the cosmic/halo cuts. We do not require this for photons in different wedges as this is very inefficient for events with no jets in the final state. After these cuts we are left with 3,447 events in the data.

Further background rejection against QCD backgrounds with fake $\not\!\!E_T$ is achieved by removing events with a potentially poor $\not\!\!E_T$ measurement. To avoid cases where a jet is mis-measured by the calorimeter we remove events which have a jet with uncorrected $E_T^j > 10$ GeV pointing within 10° in azimuth of the $\not\!\!E_T$ or more than 170° with the $\not\!\!E_T$. Note that the $\Delta\phi$ cut assumes the corrected ϕ position of the $\not\!\!E_T$ (see Subsection 3.4), and that jets are defined with a cone size of $\Delta R = 0.4$ with no η restriction.

After all the online and offline selection criteria are applied (except the final $\not\!\!E_T$ threshold, optimized, 45 GeV, described in Chapter 6 but given here for pedagogical reasons), 3,306 diphoton candidate events remain in our final sample. Figure 3.1 shows the diphoton event yield/luminosity as a function of run number and shows no change in event yield over the data-taking period. Although the results are not used in any substantial way in the analysis, just for general information, we have estimated the mixture of photons and neutral meson background using the standard statistical estimation methods of the CES/CPR [29]. We find that $29 \pm 4\%$ of the events are $\gamma\gamma$, $47 \pm 6\%$ are γ-jet, and $24 \pm 4\%$ are jet-jet.

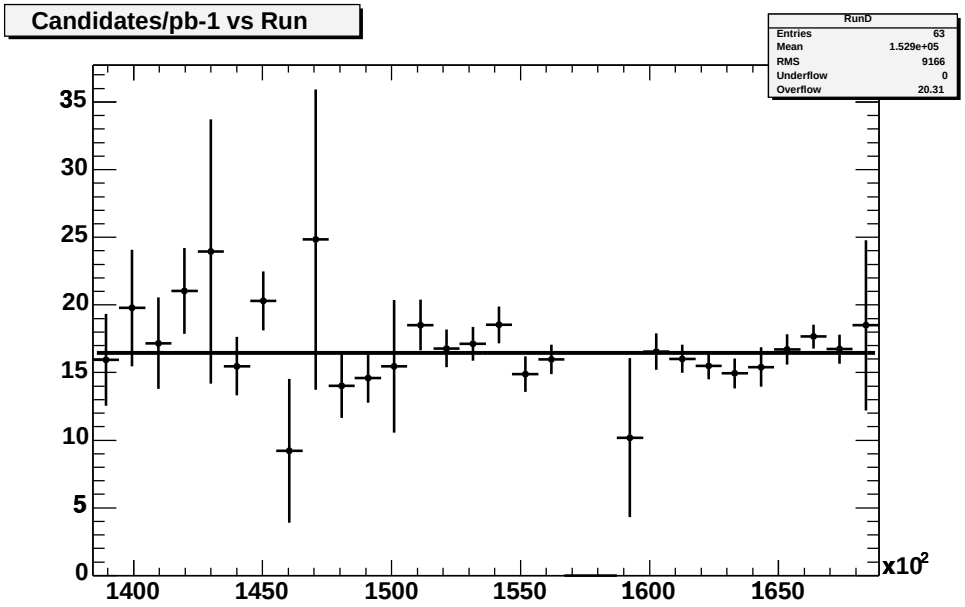

Figure 3.1: Diphoton event yield/luminosity as a function of run number.

3.3 The $Z \to ee$ and Diphoton Control Samples

Throughout this note we will use various $Z \to ee$ samples and a "control" sample of events with two EM objects which are similar to, but don't pass photon cuts, to help us estimate various quantities of interest. In both cases the samples are selected using the same triggers listed in Table 3.1, and are especially helpful because electrons and electromagnetic jets mock-up the detector response to our signal region events. The selection requirements are given in Tables 3.3 and 3.4. For simplicity we refer to a cluster which passes the cuts in Table 3.3 as being a "control" photon or as having passed the control sample cuts. There are 3,394 events in the $Z \to ee$ sample and 7,806 events in the control sample. A detailed comparison of the diphoton and control sample kinematics is given in Appendix A.

Global Event Selection, Cosmic and Halo Cuts, and $\not\!\!E_T$ cleanup cuts are same as diphoton sample
Control "Photon" Identification
Central
$E_T^{\text{"}\gamma\text{"}} > 13$ GeV
$\lvert\text{CES } x\rvert < 21.0$ cm
$9.0 < \lvert\text{CES } z\rvert < 230.0$ cm
Had/EM < 0.125
CalIso(cone 0.4) $< 3.0 + 0.02(E_T^\gamma - 20)$ $\lvert\rvert$ $< 0.15E_T^\gamma$ if $E_T^\gamma < 20.0$
$p_T < 0.25E_T^\gamma$
Σp_T(cone 0.4) < 5.0
Not in diphoton sample

Table 3.3: Photon control sample selection cuts. Note that the diphoton signal sample selections are given in Table 3.2.

Global Event Selection are the same as diphoton sample
Z Electron Identification
Central
$\lvert\text{CES } x\rvert < 21.0$ cm
$9.0 < \lvert\text{CES } z\rvert < 230.0$ cm
Had/EM $< 0.055 + 0.00045E^\gamma$
CalIso(cone 0.4) $< 2.0 + 0.02(E_T^\gamma - 20)$ $\lvert\rvert$ $< 0.1E_T^\gamma$ if $E_T^\gamma < 20.0$
average and scaled CES $\chi^2 < 20$
N3D= 1 $\lvert\rvert$ N3D= 2 and $p_T < 1.0 + 0.005E_T^\gamma$
$\Sigma \text{p}_\text{T} - \text{p}_\text{T,ele}$(cone 0.4) $< 2.0 + 0.005E_T^\gamma$
$0.8 < E/p < 1.2$

Table 3.4: The electron ID requirements use to make the $Z \to ee$ sample. The baseline sample has no mass requirement, but does require electrons which pass the above cuts. Note that the diphoton signal sample selections are given in Table 3.2.

3.4 Missing E_T Measurement and Corrections

The raw $\not\!\!E_T$ (taken from CdfMet which assumes z=0) is corrected for the vertex position and for jet energy mismeasurements. Since we want to minimize the backgrounds from mismeasurement we choose the jets and jet corrections which minimize the number of large $\not\!\!E_T$ events in a sample which has small contribution from real events with large $\not\!\!E_T$. Using the $Z \to ee$ sample described in Table 3.4 we measure the $\not\!\!E_T$ resolution and the fraction of events with $\not\!\!E_T > 20$ GeV, f_{20}, as a function of both quantities. [4] Table 3.5 shows the comparison of a number of different $\not\!\!E_T$ correction algorithms we tried. We find that correcting the $\not\!\!E_T$ for the vertex offline and for jets with raw $E_T^j > 10$ GeV with jet corrections with Level=5 corrections (version 4, or version 0 for MC, up to and including relative energy corrections, time dependence corrections, raw energy scale corrections and absolute energy corrections, but not including multiple interaction, underlying event or out-of-cone corrections).

Algorithm	Notes	σ_x	σ_y	f_{20}
0	raw $z = 0$	5.00	4.96	0.0300
1	$z = z_0$	4.65	4.70	0.0221
2	$z = z_0$, L2, $E_T > 5$	4.60	4.88	0.0187
3	$z = z_0$, L2, $E_T > 10$	4.61	4.88	0.0200
4	$z = z_0$, L2, $E_T > 15$	4.65	4.89	0.0208
5	$z = z_0$, L5, $E_T > 5$	4.54	4.64	0.0152
6	$z = z_0$, L5, $E_T > 10$	4.43	4.71	0.0126
7	$z = z_0$, L5, $E_T > 15$	4.46	4.64	0.0126

Table 3.5: A comparison of the different $\not\!\!E_T$ correction algorithms on the resolution using $Z^0 \to e^+e^-$ data. The widths are in GeV and are found from Gaussian fits to $-10 < \not\!\!E_T^x < 10$ GeV. L2 refers to level 2 jet corrections (tag jetCorr00: relative and time-dependent corrections). L5 refers to level 5 jet corrections. The E_T cut refers to the required raw jet E_T before corrections are applied. We select Algorithm 6 as the final choice for the analysis.

[4] For historical reasons this was done with no track isolation requirement and $0.5 < E/P < 1.5$ on both legs ($Z \to ee$), and $|M_Z - 91 \text{ GeV}| < 15$ GeV.

Chapter 4

Background Estimate

The magical first smile is seen at about six weeks.

`- in BabyTalk`

Background to the $\gamma\gamma + \not\!\!E_T$ final state can be grouped into the three categories below. In the next sections we discuss each. While the dominant background to the diphoton candidate sample is from QCD processes, since that background estimate relies on the $e\gamma$ background estimate methods, we begin with a description of $e\gamma$, then continue with QCD, and conclude with non-collision backgrounds:

- `QCD + fake` $\not\!\!E_T$`:` $\gamma\gamma$, γ-jet, where the jet fakes a photon, and jet-jet where both jets are photon fakes. A jet or vertex mismeasurement leads to large $\not\!\!E_T$.
- `Inclusive` $e\gamma$ `production:` Events where one of the photon candidates is really an e which faked the photon signature by "losing" its track. Many sources of electrons contain real $\not\!\!E_T$ e.g. $W\gamma \to e\nu\gamma \to \gamma\gamma_{fake}\not\!\!E_T$, $W + jet \to e\nu$+jet (lost track and jet faking photon), $Z\gamma \to ee\gamma$, $Z \to ee$, $Z \to \tau\tau \to ee + X$, $t\bar{t} \to ee + X$, WW and WZ productions.
- `Non-collision sources of spurious energy:` Cosmics, beam halo and beam-gas interactions where either one or more of the photons and/or the $\not\!\!E_T$ is spurious.

4.1 $e\gamma$ Events

If a real electron is produced but its track is not reconstructed, then it will pass all photon cuts and can form part of a background event. The track may be lost due to tracking inefficiency, or more likely, to a hard bremsstrahlung where the track curls away. The usual sources of electrons are $W \to e\nu$, $Z\gamma \to ee$, $b \to eX$, and conversions. Events which can produce $\gamma\gamma$ candidates are dominated by sources where there is a real or fake photon, such as $W\gamma \to e\nu\gamma$, $Wj \to e\nu\gamma_{fake}$, $Z\gamma \to ee\gamma$, $Zj \to ee\gamma_{fake}$, or two fake photons $Z \to ee \to \gamma_{fake}\gamma_{fake}$, $WW \to ee\ \gamma_{fake}\gamma_{fake}$, $t\bar{t} \to WWbb \to ee\nu\nu bb\gamma_{fake}\gamma_{fake}+X$ and so on. Since the rates at which electrons fake photons are low, and the rate at which $\not\!\!E_T$ is faked is low (see Section 4.2), the dominant source of $\gamma\gamma\not\!\!E_T$ candidates comes from electrons from $W\gamma \to e\nu\gamma \to \gamma\gamma_{fake}\not\!\!E_T$ production and decay.

4.1.1 Estimating the background from $e\gamma$ sources

While the dominant background comes from $W\gamma$, we estimate the background for all $\not\!\!E_T$ values and from all sources of electrons faking photons at once using the data. The method is to select a sample of events passing all the diphoton selection criteria, except we require one of the photons to be an electron. We then scale the sample down by the ratio of the E_T dependent probability for an electron to fake a photon, divided by the probability for an electron to pass the electron cuts. This estimation method thus includes all sources, including real or fake photons for the second photon, and real or fake $\not\!\!E_T$.

The $e\gamma$ sample is selected using the diphoton triggers described in Table 3.1 and the cuts in Table 3.2 except for the electron leg. To select an electron leg we require the following: central, $E_T > 13$ GeV, fiducial, Had/EM, calorimeter isolation, track isolation, CES χ^2 the same as the photons (while ignoring the leading track), and require $0.8 < E/p < 1.2$. We find 462 eγ events in the data. Figure 4.1 shows the $\not\!\!E_T$ spectrum for the sample. The same figure also shows the distribution predicted from the normalized distributions from MC

$W\gamma$ and MC $Z\gamma$ background passed through the detector simulation and using the K-factors and cross sections used by the $W\gamma/Z\gamma$ group [36]. While this MC simulation is not used in the analysis, it provides good evidence that the $e\gamma$ events with large $\not\!\!E_T$ are dominated by $W\gamma$ sources as expected.

To estimate the fake-rate scaling we use a combination of MC and data. This is done because while the simulation shows an E_T dependence on the rate at which electrons fake photons, we have no reason to believe it gets the overall rate correct as almost 30% of the material is missing in the simulation. Since the only reliable/pure sample of electrons comes from $Z \to ee$ events, we estimate the fake rate from the MC and normalize the rate to that observed in the data at $E_T \sim 45$ GeV. For the data we use the unbiased $Z \to ee$ sample described in Table 3.4, and fit to the region $|M_Z - 91 \text{ GeV}| < 15$ GeV. We find 1622 ± 65 events with both passing electron cuts, 35 ± 12 with one electron and one EM object which passes the photon cuts, 131 ± 20 with one electron and one EM object which passes the photon or control sample cuts, and 91 ± 15 with one electron and one EM object which passes the control sample cuts. The probability for an electron to pass all photon cuts divided by the probability for an electron to pass the electron cuts is given by the ratio of the first two numbers and divided by 2 (two combinations for each) and gives $1.07 \pm 0.38\%$ for the diphoton candidate cuts. Using a similar technique we find $3.88 \pm 0.62\%$ for the photon-or-control cuts, and $2.81 \pm 0.49\%$ for control cuts, which is useful for propagating uncertainties. Figure 4.2 shows the final result as a function E_T along with the E_T spectrum from electrons from Z's and from the electrons in the $e\gamma$ sample (electrons from $W\gamma$ which bremmed). Multiplying the fake rate bin-by-bin as a function of E_T we find an expected scaled background of 8.2 events in the $\gamma\gamma$ candidate sample, with 0.14 events above 45 GeV.

4.1.2 Errors on the $e\gamma\not\!\!E_T$ background estimate

Since the number of events passing the $e\gamma$ cuts is small, the statistical uncertainty on the $e\gamma$ background estimate is dominated by the uncertainty on the

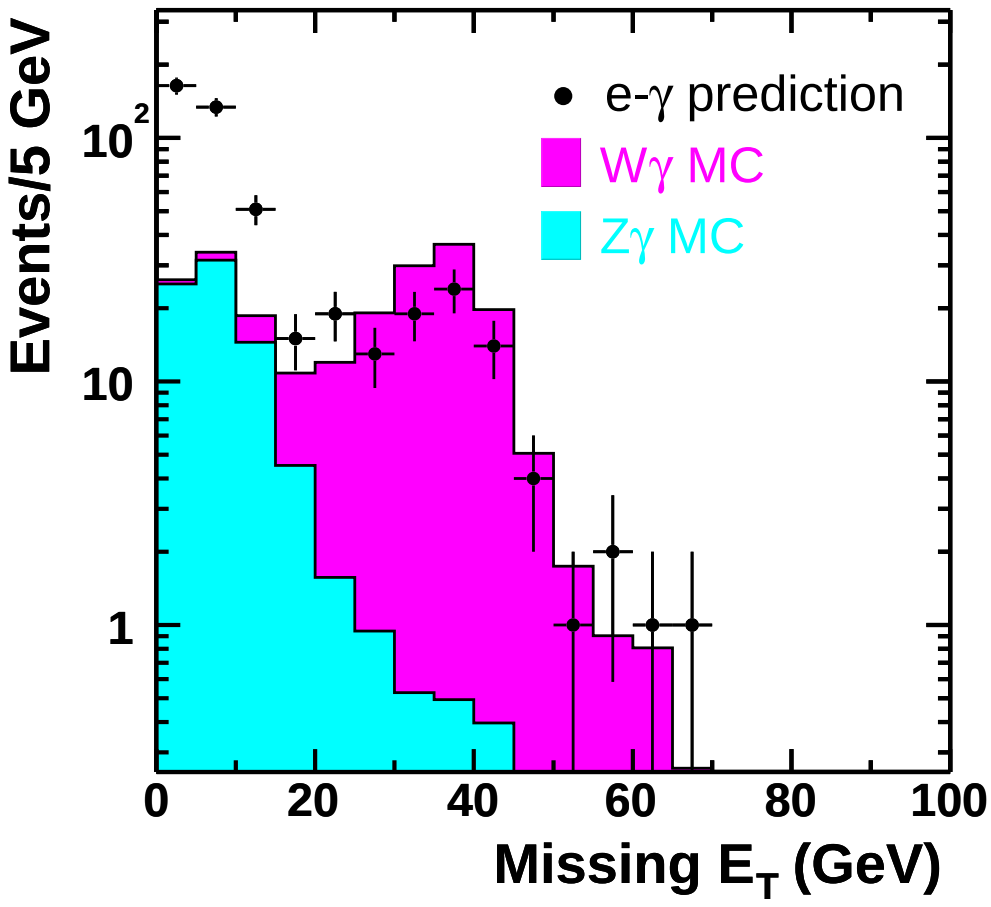

Figure 4.1: This figure shows the $\not\!\!E_T$ spectra for $e\gamma$ events with $E_T^\gamma > 13$ GeV. The points are the data and the histograms are the MC sample of $W\gamma$ and $Z\gamma$ backgrounds. No attempt has been made to estimate the low $\not\!\!E_T$ region which is presumably from $Z \to ee$ or other sources with no intrinsic $\not\!\!E_T$. As expected the background is dominated by $W\gamma$ production and decay.

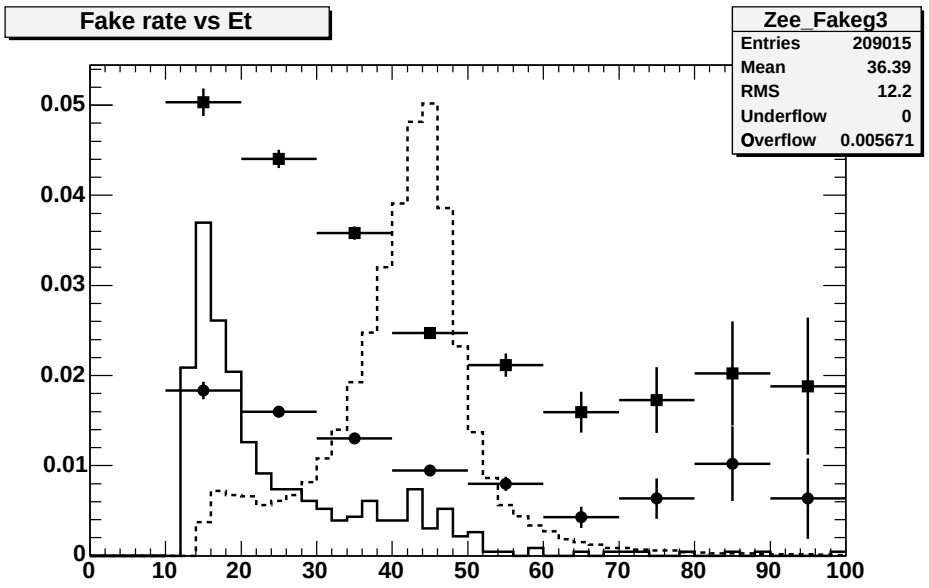

Figure 4.2: This figure shows the rate at which electrons fake photons as a function of E_T^{γ}. The circles are the photon fake rate vs. E_T from Drell-Yan MC, the squares are the rate at which EM clusters pass the photon or control sample cuts vs. E_T from Drell-Yan MC, the histogram is the data $e\gamma$ electron E_T distribution, and the dashed hist is the $Z \to ee$ electron E_T distribution.

$e \to \gamma$ fake rate and is 40%. In addition, we include the uncertainty from the number of $e\gamma$ events.

The dominant systematic error comes from the concern that part of the $e\gamma$ sample is not from real electron sources. If electron fakes come from pions in jets then they will not brem the way that electrons do, so they will fake photons at a lower rate. To investigate this, we looked at the E/p, CES Δx and Δz distributions and found that the sample is clearly dominated by electrons. The fake electrons are estimated to be less than 10% so we overestimate the error and take a 10% systematic uncertainty on this source of background. The final estimate is 8.21 ± 2.95 events in the $\gamma\gamma$ candidate sample, with $0.14 \pm 0.06 \pm 0.05$ events above 45 GeV.

4.2 QCD Background

QCD, $\gamma\gamma, \gamma j$, and jj, events have no intrinsic missing E_T, and only appear in the high-$\not\!\!E_T$ signal region due to mis-measurement of the $\not\!\!E_T$. We estimate the number of $\gamma\gamma$ with large $\not\!\!E_T$ using the data and the following steps:

- We take the shape of the $\not\!\!E_T$ distribution from the control sample.
- We next correct the shape of the $\not\!\!E_T$ distribution as a function of $\Sigma \mathrm{E_T^{Corrected}}$ using a Histogrammed MET Model (described in Section 4.2.2).
- We next subtract off the $e\gamma$ contribution in the control sample to avoid double counting.
- Finally we fit to the low-$\not\!\!E_T$ region and project to the signal region to estimate the number of events in the high-$\not\!\!E_T$ region ($\not\!\!E_T >$ 45 GeV).

4.2.1 Using the control sample

To first-order the control sample should have the same calorimetric response and $\not\!\!E_T$ resolution as the diphoton sample because a jet that fakes a photon fragments into one or more neutral pions which decay to photons and shower in a manner which is similar to a single photon in the calorimeter. Therefore we can estimate the QCD background by extracting the shape of the $\not\!\!E_T$ distribution from the control sample. More material supporting this idea can be found in Appendix A.

4.2.2 Correcting for differences between the diphoton sample and the control sample: The Histogrammed MET Model

It has long been known that the $\not\!\!E_T$ resolution is a function of the total energy in the calorimeter for an event (see for example Ref. [4]). Thus, differences in the total energy between two samples can cause their $\not\!\!E_T$ distributions to not

be the same, even when there is no intrinsic $\not\!\!E_T$. Since the resolution is more a function of the E_T of the jets and the unclustered energy than the photons, we take as the measure of total energy to be $\Sigma \mathrm{E_T^{Corrected}}$ where we take

$$\Sigma \mathrm{E_T^{Corrected}} = \Sigma \mathrm{E_T} - \mathrm{E_T^{\gamma_1}} - \mathrm{E_T^{\gamma_2}} - \Sigma(\mathrm{E_T^{uncorrected\ jet}} - \mathrm{E_T^{corrected\ jet}}), \qquad (4.1)$$

that is, $\Sigma \mathrm{E_T}$ taken over all towers, subtract off the uncorrected photon energies, and correct for all jets with $E_T^j > 10$ GeV. Figure 4.3 compares the $\Sigma \mathrm{E_T^{Corrected}}$ distributions of the diphoton sample and the control sample. The means of the distributions for the two samples are similar, but not identical. They are separated by approximately 6%, most likely due to different percentage contributions from $\gamma\gamma$, γj, and jj which may have different $\Sigma \mathrm{E_T^{Corrected}}$. We correct for this difference.

In Run I we corrected for differences between $\Sigma \mathrm{E_T^{Corrected}}$ in the control sample [1] and the diphoton sample using a method which assumed that the $\not\!\!E_T$ distribution was well modeled by Gaussian errors on resolution [4]. However, at this point in time, with the current calibrations, this method does not reproduce back the distribution it was taken from so we have abandoned it for this analysis. For more details see Appendix B. Furthermore, since the control sample is larger than the $Z \to ee$ sample, we now elect to use it instead.

To estimate the background at large $\not\!\!E_T$ we use a Histogrammed MET Method based on the control sample. We begin by dividing the events into regions of $\Sigma \mathrm{E_T^{Corrected}}$ (a histogramed value) and make the $\not\!\!E_T$ distribution for each region. These $\not\!\!E_T$ distributions are then summed with a weighting given by the number of events in the diphoton sample with the same $\Sigma \mathrm{E_T^{Corrected}}$ region value, thus correcting the difference in the $\Sigma \mathrm{E_T^{Corrected}}$ between the samples. We check the method using the control sample to predict the $\not\!\!E_T$ distribution for a $Z \to ee$ sample, and a $Z \to ee$ sample to predict the control and diphoton samples. The results are shown in Figure 4.4 along with the uncertainties. In general the $\not\!\!E_T$ predictions based on the Histogrammed MET Method agree well with the shape of the data.

[1] In Run I we used a $Z \to ee$ control sample.

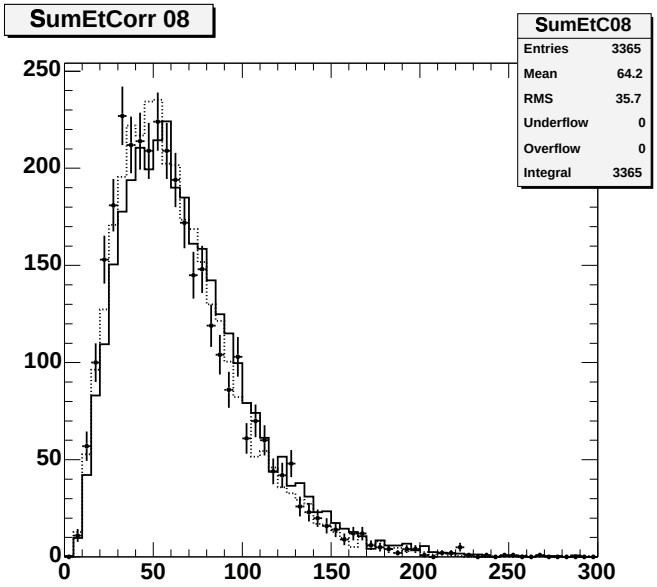

Figure 4.3: The $\Sigma E_T^{Corrected}$ distributions for the diphoton (points) and control (solid histogram) samples. The two are similar, but shifted by approximately 6%. The dotted histogram shows the control sample scaled 0.937 for comparison.

4.2.3 Subtracting off the $e\gamma$ background

The $e\gamma$ background will appear in both the diphoton candidate sample and the control sample. Since we are using the control sample to determine the QCD background in the signal region, we want to first subtract the $e\gamma$ background from the control sample to derive a pure QCD shape. This subtraction is complicated by the fact that the control sample is selected with loose ID/Iso cuts and any $e\gamma$-control sample used for subtraction can have multiple ways an electron can contribute. The number of $e\gamma$ events in the control sample is found using the following relation:

$$N_{e\gamma_{control}} = (N_{e\gamma_{control}} - N_{e\gamma}) \times \mathcal{P}(e \to \gamma_{control}) + N_{e\gamma} \times (\mathcal{P}(e \to \gamma_{control}) - \mathcal{P}(e \to \gamma)) \quad (4.2)$$

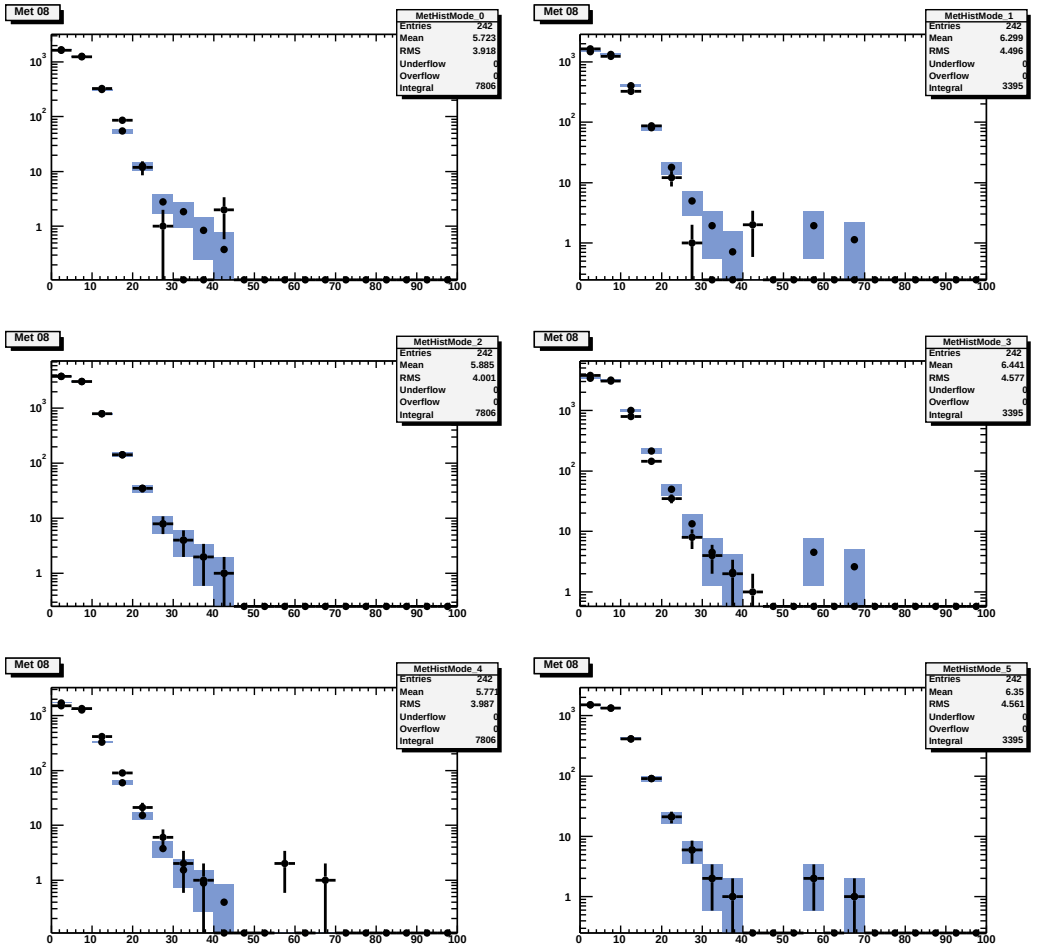

Figure 4.4: A comparison of $\not\!\!E_T$ data distribution to a background shape predicted from the Histogrammed MET Method using various samples. The histograms in the two columns have the predictions from (1) the control sample (2) the $Z \to ee$ sample. The three rows are $\not\!\!E_T$ for (1) diphoton data, (2) control sample data and (3) $Z \to ee$ data. In all plots the points are data and the solid, with uncertainties, is the background prediction. Middle-left and bottom-right should match the prediction exactly. This shows that the method does a good job of allowing us to predict the $\not\!\!E_T$ in various samples.

where $\mathcal{P}$ is the fake rate measured in Section 4.1.1, γ indicates that the photon passes the ID and Isolation cuts in Table 3.2, and $\gamma_{control}$ indicates that it passes the cuts in Table 3.3.

4.2.4 Extrapolating the shape to large $\not\!\!E_T$ values

Because the control sample is statistics limited, to get the best estimate for large values we do a double exponential fit to the corrected control sample events with $\not\!\!E_T < 45$ GeV, and extrapolate to $\not\!\!E_T > 45$ GeV. We find that the data in the low $\not\!\!E_T$ region is best modeled (see Section 4.2.5 and Figure 4.5) by this fit. After the fit, we expect 0.01 events of QCD background of $\not\!\!E_T > 45$ GeV.

4.2.5 Errors on the QCD background estimate

The statistical error on the background is taken from the $\pm 1\sigma$ variation from the double exponential fit which is extrapolated to $\not\!\!E_T > 45$ GeV. To get the systematic error on the number of events above 45 GeV we examine the effects of varying the control sample fit function. These includes (1) double exponential, (2) single exponential, (3) Gaussian+single exponential and (4) single exponential with a threshold function. The best-fit for each function is shown in Figure 4.5 with the number of expected event with $\not\!\!E_T > 45$ GeV in each given in Table 4.1. The variations implies a 70% systematic uncertainty on the background estimate.

We also examine the effects of varying the control sample selection criteria by slightly tightening (or loosening) the cuts as specified in Table 3.3. These includes tightening the energy isolation to the diphoton sample value, tightening $p_T < 1.0$ GeV, tightening $\Sigma p_T < 2.0$ and adding a second CES cut which is the same as the diphoton sample value. The variations to the control sample are shown in Figure 4.6 and all the variations describes the shape of the default control sample $\not\!\!E_T$ well. Numerically, each control sample $\not\!\!E_T$ distribution is normalized to the default control sample distribution and, after fitting

each with the default double exponential to predict the number of events with large $\not\!\!E_T$, the results are given in Table 4.2. The effects of varying the control selection are taken into account as a systematic uncertainty, and give rise to a systematic error averaging 60% on the number of QCD events above 45 GeV. The final total background estimate is $0.01 \pm 0.01 \pm 0.01$.

Fit functions	Number of expected above $\not\!\!E_T > 45$ GeV	χ^2/ndf
Double exponential	0.014	2.13/8
Single exponential	0.004	3.86/10
Gaussian+single exponential	0.002	4.57/7
single exponential + $\frac{A}{1+e^{B\times(x-C)}}$	0.014	2.13/7

Table 4.1: The fit functions applied to fit the control samples and the number of expected above $\not\!\!E_T > 45$ GeV.

Selection Criteria	Number of expected above $\not\!\!E_T > 45$ GeV
Control	0.014
Control + Diphoton Isolation	0.010
Control + p_T $<$ 1.0 GeV	0.007
Control + Σp_T $<$ 2.0 GeV	0.006
Control + Diphoton 2nd CES	0.006

Table 4.2: Selection criteria applied to select the control sample and the number of expected above $\not\!\!E_T > 45$ GeV. Here we have changed the values of the control sample cuts to be from their nominal values

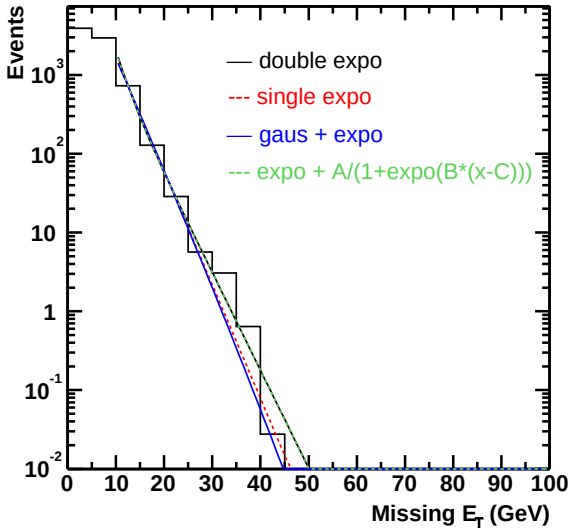

Figure 4.5: The results of fits to the control data using different functional forms to estimate the systematic uncertainty. The lines are fit to $\not\!\!E_T < 45$ GeV and extrapolated to $\not\!\!E_T > 45$ GeV. We take $\pm 1\sigma$ in the fit function as the uncertainty for $\not\!\!E_T > 45$ GeV.

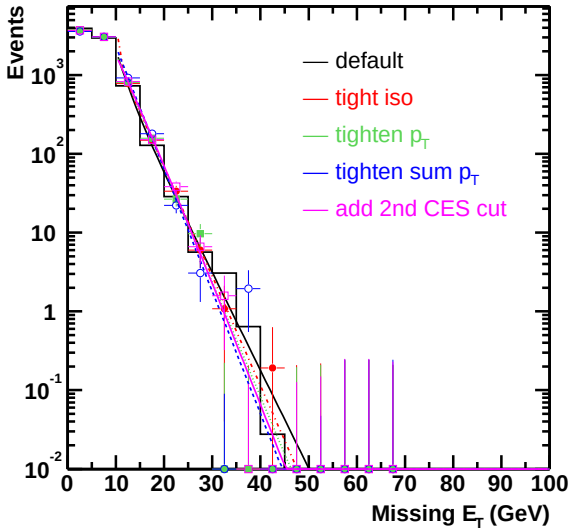

Figure 4.6: Control sample ID/Iso selection variation on the QCD background estimate. These include: default selection, (1) tighten isolation energy to diphoton candidate selection cut value, (2) tighten $p_T < 1.0$ and N3d $= 1$, (3) tighten $\Sigma \mathrm{p_T} < 2.0$ and (4) second CES cut. Each control $\not\!\!E_T$ distribution is normalized to the default control sample.

4.3 Events with Non-Collision Sources of Spurious Energy

Events with spurious energy, i.e., not from the collision, constitute the last important background. The spurious energy can come from sources such cosmic rays which bremsstrahlung in the calorimeter, beam-halo or beam-gas interactions, and may take the form of a fake photon which is not from the collision or fake energy in the calorimeter which gives an energy imbalance i.e., fake $\not\!\!E_T$. While the level of non-collision backgrounds in the $\gamma\gamma$ sample is small, see Figure 4.7, this background can be problematic because of the large probability that if it does produce all or part of a $\gamma\gamma$ event, it is likely to have large $\not\!\!E_T$. It is for this reason that we have placed additional topology cuts to directly remove these backgrounds as discussed in Table 3.2.

To first order all these sources should show up in the control sample so we begin with that dataset to estimate the number of events from non-collision sources. However, the statistics of that estimate are poor and do not allow for a estimate which tells us if it is the dominant background or if the rejection methods are strong enough. To estimate the number of residual out-of-time events in the signal region we use the fact that the HADTDC cut is 97% efficient and removes approximately 80% of the out-of-time backgrounds [34]. Before the $\Delta\phi$ and HADTDC cut, but after the $\not\!\!E_T > 45$ GeV cut, we estimate 0.67 events from the control sample and eγ backgrounds and observe 1 event in the data. Using the one event in the data to estimate the number of cosmics in the sample at $1.0-0.67 = 0.33$, and that after the HADTDC cut we expect to remove 80% of out-of-time events we expect $(1-0.80)\times 0.33 = 0.07$ events from out-of-time sources. As another estimate we take the all-but-HADTDC sample which has an estimate of 0.24 events from the control sample and eγ, and 1 event in the data. Using the same methodology we expect $(1-0.80)\times(1-0.24) = 0.15$ out-of-time events. These small number give a fair range of the systematic uncertainty and are consistent with the zero events in the final sample.

To get a more sophisticated estimate we divide the spurious energy sources

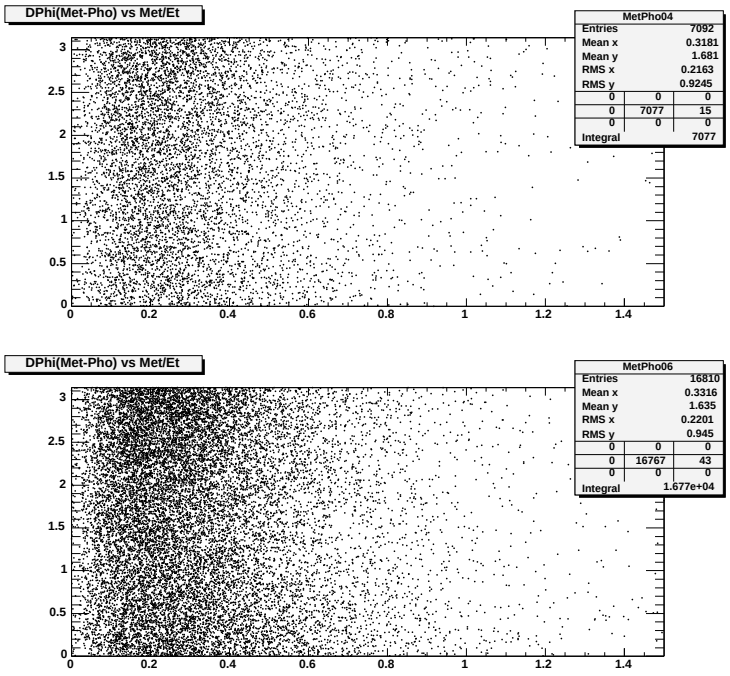

Figure 4.7: The x-axis is the event $\not\!\!E_T$ divided by the photon E_T (one entry per photon), and the y-axis is $\Delta\phi(\not\!\!E_T - \gamma)$. A photon from cosmic and halo backgrounds would appear in the region $0.8 < \mid \not\!\!E_T/E_T^{\gamma} \mid < 1.2$, and $\Delta\phi(\not\!\!E_T - \gamma) > 2.9$. The sample has very few of these events. The upper plot is for diphoton candidate data events and the lower plot is for the control sample.

into three kinds and estimate separately.

- Type 1a, where the spurious energy is one of the photons.
- Type 1b, where the spurious energy is both of the photons. This occurs, for example, when a muon from a cosmic or halo either brems twice or a single cosmic ray shower produces two separate clusters.
- Type 2, where the photons are part of the collision, but the $\not\!\!E_T$ is caused by some other type of interaction like-beam gas.

To be conservative, while these numbers are small, we add them to the control sample and $e\gamma$ numbers as part of the full background estimate.

4.3.1 Type 1a: One Spurious Photon

The rate at which cosmics/halo produce a single spurious photon on top of a SM event to produce the $\gamma\gamma + \not\!\!E_T$ final state can be estimated in an *a priori* manner using the data. The method is the following:

- Count the number of low-E_T photons in no-vertex data to estimate the number of photons which appear in a crossing from a spurious source.
- Estimate the number of empty crossing to get the probability that a spurious photon will show up in any given crossing.
- Apply this accidental, or overlap, rate to the inclusive photon sample to find the number of diphoton events expected due to a single cosmic overlapping a single photon event.
- Correct for the fraction of events with $\not\!\!E_T > 45$ GeV.

First we define a sample dominated by spurious energy clusters, which we can call the "cosmic-like" sample, selected by the presence of an EM cluster and no vertex in the event. [2] We begin with the `EM8` trigger data, which only requires a single EM-tower with 8 GeV. In about 200 pb^{-1} there are 539 events with $\not\!\!E_T < E_T - 2$ GeV ($\not\!\!E_T$ is equal to the cluster) and no vertex (unlikely to be caused by collision), and $\Sigma E_T - \not\!\!E_T < 10$ GeV (no other energy in the event). To get the number of spurious "photons" we use the probability for a cluster to pass the photon cuts which comes from the 71 events in the data. The probability as a function of E_T is shown in Figure 4.8 and is about 15%, but appears to be dropping at higher E_T. Since the `EM8` trigger is prescaled by 2,500 and taking the average of 15% we estimate there to be $539 \times 2,500 \times 0.15 \approx 200,000$ crossings with spurious photons in the data.

We next estimate the rate of empty crossings using the data. The average instantaneous luminosity (estimated from the data) is $17 \cdot 10^{30}$ cm^{-2} s^{-1}. With

[2] Since there is no vertex, these clusters must be caused by a spurious source such as cosmics or beam halo, to first order.

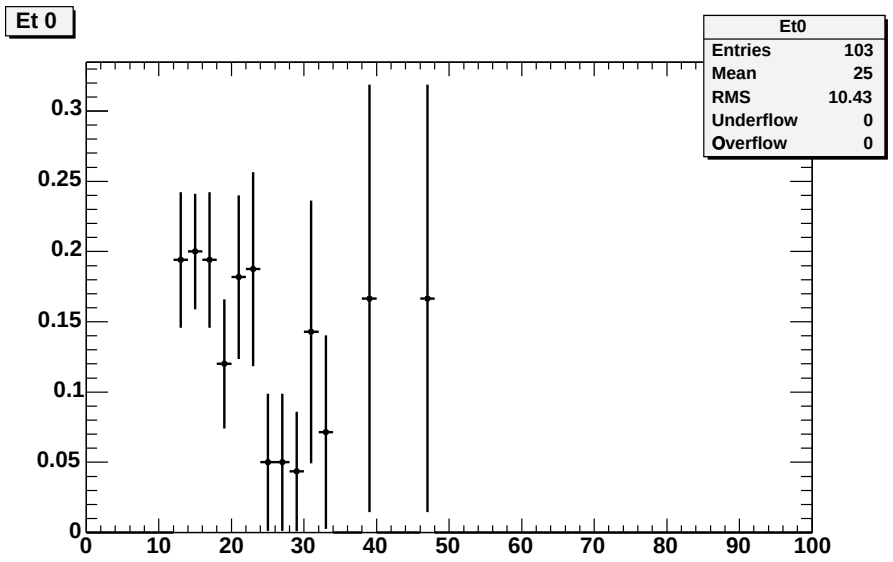

Figure 4.8: In the EM8 sample, there are 529 events with $\not\!\!E_T < E_T - 2$ GeV ($\not\!\!E_T$ is equal to the cluster) and no vertex, and $\Sigma E_T - \not\!\!E_T < 10$ GeV (no other energy in the event). The probability for these clusters to pass photon cuts is shown here as a function of E_T.

200 pb^{-1} and converting using 10^{-36} cm^2 in 1 pb^{-1}, we find an effective live time of $1.2 \cdot 10^7$ s. Since crossings occur at 36 crossings per 20 μs = 1.8 MHz, this implies $2.2 \cdot 10^{13}$ crossings observed. The fraction of time over the last 1.5 years (1.5 years $\times 3 \cdot 10^7$ s $= 4.5 \cdot 10^7$ s) we were live is thus $\frac{1.2 \cdot 10^7 \text{s}}{4.5 \cdot 10^7 \text{s}} = 0.27$, which is a typical duty factor. With a minbias cross section of 60 mb we expect $17 \cdot 10^{30}$ cm^{-2} s^{-1} $\times$ (60 mb) $\times \frac{10^{-27} \text{ cm}^2}{\text{mb}} = 1$ MHz of minbias events. If we expect $\frac{1.0 \text{ MHz}}{1.8 \text{ MHz}} = 0.55$ interactions per crossing, then we expect $e^{-0.55} = 0.60$ to be the probability of having an empty crossing. Given the $2.2 \cdot 10^{13}$ observed crossings we expect $2.2 \cdot 10^{13} \times 0.60 = 1.3 \cdot 10^{13}$ empty crossings. Combining with the $2 \cdot 10^5$ spurious photon events we estimate the probability of seeing a photon overlapping with a given event is $\frac{2 \cdot 10^5}{1.3 \cdot 10^{13}} = 1.5 \cdot 10^{-8}$.

Given the number of events with a single photon, we can apply the overlap to find the number of diphoton events in the sample from this source. From the EM8 triggers, we find 16K events which pass all photon cuts and have

$E_T > 13$ GeV. Multiplying by the 2,500 prescale, we find $4 \cdot 10^7$ inclusive photon events. Multiplying by the probability to overlap a cosmic gives $4 \cdot 10^7 \times 1.5 \cdot 10^{-8} = 0.6$ events.

Finally, we can take the number of $\gamma\gamma$ candidates from this source and estimate the rate at which events pass both the cosmic rejection and $\not\!\!E_T$ requirements. To estimate how many events are in the signal region, we first overestimate the rate at which cosmics push the $\not\!\!E_T$ from a typical event (order 5 GeV of $\not\!\!E_T$) to over 45 GeV and into the signal region by looking at events in the cosmics-like sample with more than about 30 GeV. We find 27% of the 600 events have $\not\!\!E_T >$ 30 GeV. Since in the final analysis we further require the events to have no muon stubs and to pass anti-halo cuts if the $\not\!\!E_T$ is equal and opposite one of the photons (which we expect to happen in these events) and we apply HADTDC cuts, we multiply by the total spurious cluster rejection factor of 90%. Thus, the final estimate is $0.6 \times 0.27 \times 0.1 = 0.016$ events.

There are a number of sources of uncertainty with this estimate. The statistical uncertainty is of order 10% from the fraction of cosmic-like events with $\not\!\!E_T$>30 GeV. We assign a 50% uncertainty due to potential Standard Model contamination in the sample used to measure the rate that spurious clusters pass cuts. We assign another 50% uncertainty due to the estimate of how much spurious energy is need to push the $\not\!\!E_T$ over 45 GeV since we used order-of-magnitude E_T cuts instead of convoluting the distributions. The final estimate is thus $0.016 \pm 0.0013 \pm 0.011$.

4.3.2 Type 1b: Two Spurious Photons

In this case both photon candidates are from the spurious energy source. We have already seen a few examples of this, one double halo and two cosmics, [3] which failed at least one final cut but came to our attention in previous versions, and indicate that this may actually be the largest spurious energy background. To estimate the background from this source case, we create a sample

[3]For example events (Run number/Event number), 153372/599319 and 160823/3284373 are cosmic-like and 154069/185247 is double-halo like. All are close, in some sense, to passing cuts.

of very loose diphoton candidate to accept more, hopefully mostly spurious, events at large $\not\!\!E_T$, and then apply the rejection rate for photon cuts to get the final estimate.

The sample of two very loose photons is selected as being events with two central clusters with $E_T > 13$ GeV, and $\not\!\!E_T > 45$ GeV, that passing the passing goodrun, vertex and diphoton trigger requirements in Tables 3.1 and 3.2. A total of 537 events pass these requirements. From this sample we select two separate sub-samples for comparison for the final estimate. The first sub-sample requires that the two clusters pass Had/EM and calorimeter isolation requirements (leaving 72 events) and that we reject W's by requiring no tracks more than 1 GeV pointing at the clusters leaving 4 events. The second sub-sample also adds the Had/EM and calorimeter isolation requirements, but releases the vertex requirement. Here we find 13 events and average the two results to get 8.6 events. Since, from the previous subsection we know that 40% of crossings have an interaction, and if this sample is dominated by spurious energy, then this predicts $8.6 \times 0.4/0.6 = 6.3$ events with a vertex.

From the cosmic-like sample from the previous section, we find 20% of cosmics passing Had/EM, iso and track cuts also pass all other photon cuts. If the HADTDC cut alone has an additional rejection of 60%, this implies a background of $6.3 \times (20\%)^2 \times (1 - 0.6) \approx 0.1$ events left in the signal sample. [4]

This is a small background which is difficult to quantify to high precision. Since it isn't the dominant background and large uncertainties are not a problem we have overestimated the background uncertainty to be 50% to the number of spurious clusters which pass photon cuts. We assign another 50% uncertainty to the number of events in the loose samples before cut rejection rates are applied since these samples can have Standard Model contamination. We assign another 50% to cover the difference between the two methods, even though they are statistically consistent. The statistical uncertainty is of order 30%. The final estimate is then $0.10 \pm 0.025 \pm 0.088$.

[4] The control sample cuts only reject 40% of the cosmic-like sample so we expect $4 \times 0.6 \times 0.6 \times 0.4 = 0.6$ events in the control sample.

4.3.3 Type 2: Unrelated to the Photons

If the photons are part of the primary collision and the energy imbalance is due to spurious energy then this source must produce $\not\!\!E_T$ in all types of events with equal probability. To estimate the rate of this background source we use empty crossings (events with no vertex) to estimate the rate at which significant $\not\!\!E_T$ is produced when there is no collision, [5] and then multiply this probability for spurious energy to overlap a given event by the observed number of diphoton events in the data.

To estimate the rate at which we observe significant $\not\!\!E_T$ in an empty crossing we use data collected from the $\not\!\!E_T$ trigger since there is nothing in the trigger to reject large spurious energy deposits with high efficiency [37]. If we select events with $\not\!\!E_T > 45$ GeV and $\Sigma E_T - \not\!\!E_T < 10$ GeV and no vertex, then we almost certainly have the complete sample of spurious energy in crossings with no interactions. Figure 4.9 shows the distributions of $\not\!\!E_T$ and $\Sigma E_T - \not\!\!E_T$. We can make a rough projection backwards of the $\not\!\!E_T$ from the region above 45, to the region above 25, and we find it increases the event rate by a factor of 2. We are using the number of events with $\not\!\!E_T >$ 25 GeV to overestimate this background as well as because this spurious met will be added to the $\not\!\!E_T$ already in the event due to resolution to cause the total $\not\!\!E_T$ to go over 45 GeV.

We estimate the total to be about 2 M events in 200 pb^{-1}. With crude HADTDC cuts, [6] we can reject about 90% of these events. We found only a 10% variation in the rejection as we varied the TDC window size or varied from 0.5 to 1.0 GeV the minimum energy required to be in a HAD tower before using its TDC information. After rejecting 90% of the events with spurious energy, we have $\approx$ 200K events with large $\not\!\!E_T$ and no vertex. Using the $1.3 \cdot 10^{13}$ estimated crossings with no interaction from Section 4.3.1, we estimate the probability of seeing fake $\not\!\!E_T$ from a non-collision source to be $1.3 \cdot 10^{13} \times 2 \cdot 10^{5} \approx 3 \cdot 10^{-8}$. The number overlapping with the $\sim$ 3K diphoton

[5] It is a mild assumption that if the out-of-time energy is not related to the interaction (essentially true by definition, and true for cosmics, halo, spikes, beam gas and most electronics failures) that we can study empty crossings to isolate this type of energy deposit.

[6] This is done for technical reasons which are particular to large sample sizes.

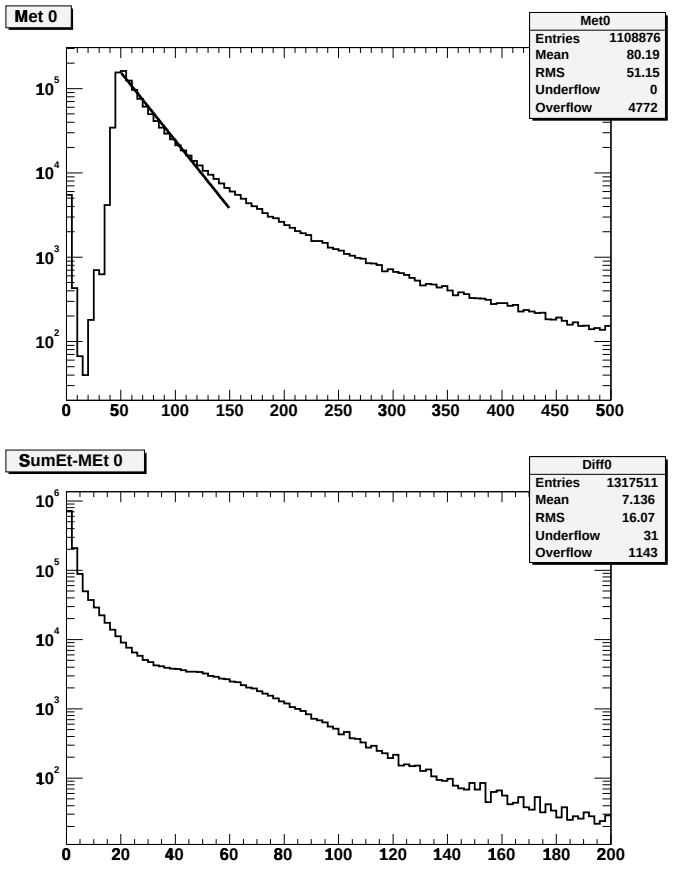

Figure 4.9: The distributions of $\not\!\!E_T$ (left) and $\Sigma E_T - \not\!\!E_T$ (right). We can make a rough projection of the event rate of $\not\!\!E_T > 45$ GeV, to the region above 25 GeV, and we find it increases the area by a factor of 2.

candidate events is thus $1 \cdot 10^{-4}$ which is negligible compared to the other sources.

4.3.4 Total Cosmic Background

Summing the above sources, we expect $0.12 \pm 0.025 \pm 0.088$ events in the signal region, dominated by events where the source produces both photons. Table 4.3 summarizes the results for other values of the $\not\!\!E_T$ cuts.

$\not\!\!E_T$ Cut	Type 1a	Type 1b	Total
25 GeV	$0.06 \pm 0.03 \pm 0.04$	$0.480 \pm 0.06 \pm 0.04$	$0.5 \pm 0.06 \pm 0.4$
35 GeV	$0.035 \pm 0.002 \pm 0.02$	$0.21 \pm 0.04 \pm 0.2$	$0.3 \pm 0.04 \pm 0.2$
45 GeV	$0.016 \pm 0.001 \pm 0.01$	$0.10 \pm 0.03 \pm 0.09$	$0.12 \pm 0.03 \pm 0.09$
55 GeV	$0.0089 \pm 0.001 \pm 0.006$	$0.06 \pm 0.02 \pm 0.05$	$0.07 \pm 0.02 \pm 0.05$

Table 4.3: Summary of the non-collision backgrounds. We have ignored type 2. For all numbers, the first uncertainty is statistical, the second is systematic.

4.4 Background Summary

In this Section we discussed the dominant SM backgrounds to the diphoton sample and estimated the event counts from each background source. We expect a total of $0.27 \pm 0.07 \pm 0.10$ events with $\not\!\!E_T > 45$ GeV. Table 4.4 summarizes the backgrounds for four different $\not\!\!E_T$ requirements and compares with the observed numbers of events. Each is consistent with the expectations from the background predictions within errors. As discussed in Chapter 6, after optimization, the final $\not\!\!E_T$ cut is 45 GeV. There are no events above the $\not\!\!E_T > 45$ GeV threshold.

$\not\!\!E_T$	**Expected**				**Obs**
Cut	QCD	$e\gamma$	Non-Collision	Total	
25	$4.01 \pm 3.21 \pm 3.76$	$1.40 \pm 0.52 \pm 0.45$	$0.54 \pm 0.06 \pm 0.42$	$5.95 \pm 3.25 \pm 3.81$	3
35	$0.30 \pm 0.24 \pm 0.22$	$0.84 \pm 0.32 \pm 0.27$	$0.25 \pm 0.04 \pm 0.19$	$1.39 \pm 0.40 \pm 0.40$	2
45	$0.01 \pm 0.01 \pm 0.01$	$0.14 \pm 0.06 \pm 0.05$	$0.12 \pm 0.03 \pm 0.09$	$0.27 \pm 0.07 \pm 0.10$	0
55	(negligible)	$0.05 \pm 0.03 \pm 0.02$	$0.07 \pm 0.02 \pm 0.05$	$0.12 \pm 0.04 \pm 0.05$	0

Table 4.4: Number of observed and expected events from the background sources as a function of the $\not\!\!E_T$ requirement. Here "QCD" includes $\gamma\gamma$, γj and jj processes. The first uncertainty is statistical, the second is systematic.

The $\not\!\!E_T$ distribution of the diphoton candidate sample, see Figure 4.10, shows good agreement with that of the expected backgrounds, the sum of QCD, $e\gamma$ production and non-collision backgrounds. Note that for completeness we have separated out the contribution from the QCD diphoton production (using CES/CPR background subtraction method) even though those numbers are

not used in the analysis.

We investigated two events in the bin between 40 and 45 GeV. Both two events have small mass, with two photons nearby each other, shown in Figure 4.11 and 4.12. The one with the display does not look like a halo and the photons are in different wedges in both events. Perhaps they are W' electrons which radiate a photon and then lose their tracks. That would also explain why they are close. The physics parameters are shown in Table 4.5.

Run/Event	**143281/791695**	**167998/1041462**
E_{T_1} (GeV)	26.368	19.114
E_{T_2}	17.401	16.915
ϕ_1 (rad)	4.81	4.04
ϕ_2	5.36	3.86
η_1	-0.78	-0.96
η_2	-1.02	-0.21
mass (GeV)	12.893	12.595
$\not\!\!E_T$ (GeV)	40.775	40.613
$\not\!\!E_T$' ϕ (rad)	1.9014	1.7697
ΣE_T (GeV)	52.877	107.38

Table 4.5: Parameters describing two events with $\not\!\!E_T > 40$ GeV. Both two events have small mass, with two photons are nearby each other, shown in Figure 4.11 and 4.12. Two photons are ordered by E_T. There exist no distinct jet or electron or muon in R143281/E791695. R167998/E1041462 has two jets with $E_T = 16$ and 11 GeV, approximately.

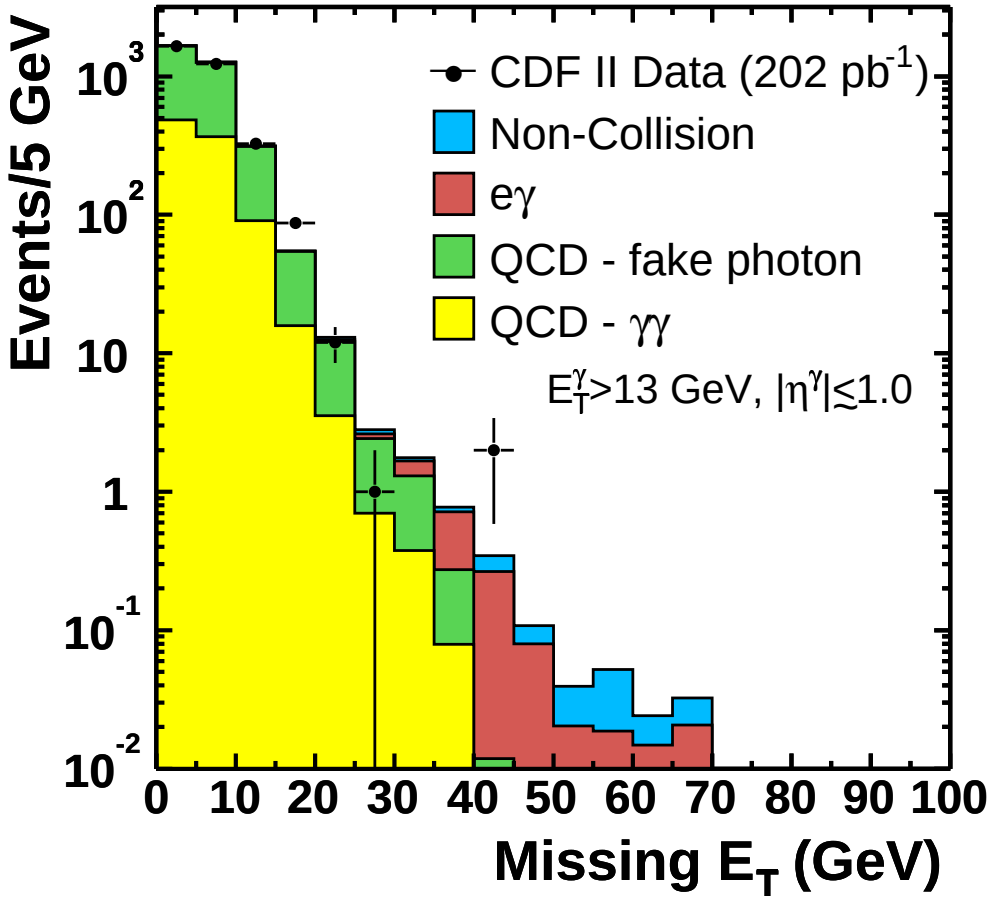

Figure 4.10: The $\not\!\!E_T$ spectrum for events with two isolated central photons with $E_T^\gamma > 13$ GeV and $|\eta^\gamma| \lesssim 1.0$. The diphoton candidate sample data are in good agreement with the background predictions. There are no events above the $\not\!\!E_T > 45$ GeV threshold.

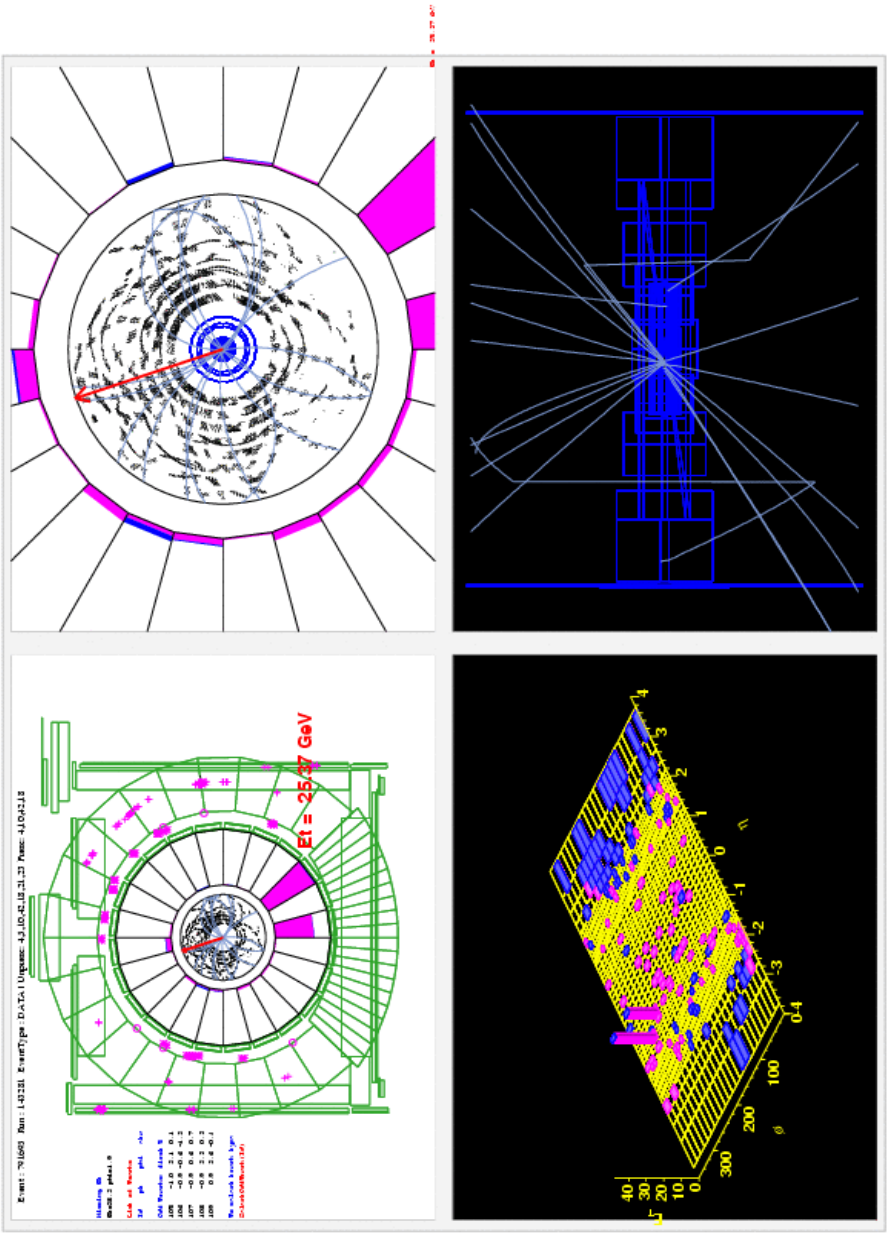

Figure 4.11: The Event Display of R143281/E791695 with $\not\!\!E_T > 40$ GeV. The arrow indicates the direction of $\not\!\!E_T$. Two photons are nearby each other. One has 25.37 GeV in raw E_T (before corrected). There exist no jets, electron or muon. See Table 4.5 for details.

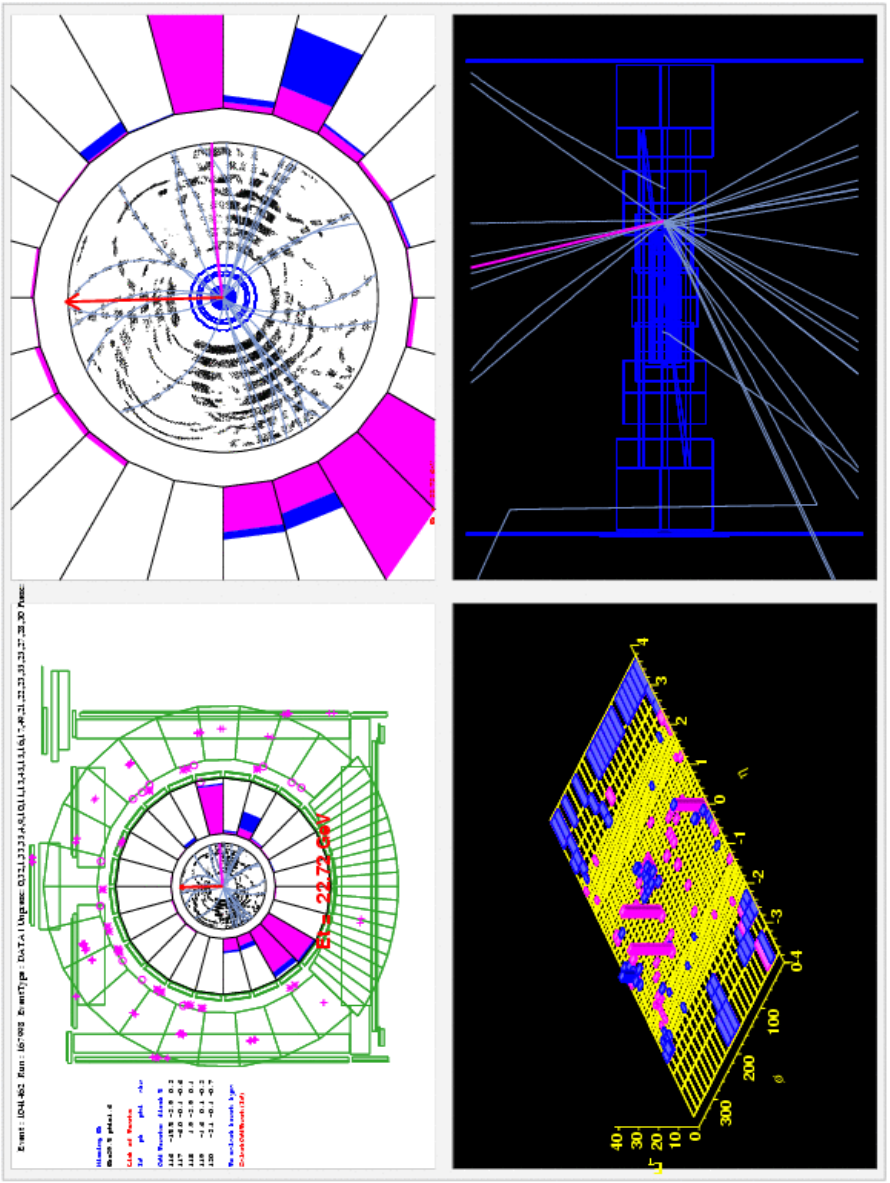

Figure 4.12: The Event Display of R167998/E1041462 with $\not\!\!E_T > 40$ GeV. The arrow indicates the direction of $\not\!\!E_T$. Two photons are nearby each other. One has 22.72 GeV in raw E_T (before corrected). There are two jets with $E_T = 16$ and 11 GeV, respectively. See Table 4.5 for details.

Chapter 5

Models and Acceptances

The baby is more inclined to smile at familiar adults than at stranger.

- in BabyTalk

Since there is no evidence for events with anomalous $\not\!\!E_T$ in the diphoton candidate sample, we set limits on new particle production from GMSB using the parameters suggested in Ref. [38], and the following relationship:

$$\sigma \cdot \mathcal{B}r\ (p\bar{p} \rightarrow GMSB \rightarrow \gamma\gamma + \not\!\!E_T + X) = \frac{\mathrm{N}_{95\%}}{\mathcal{L} \cdot \mathcal{A}_{\mathrm{MC}}} \tag{5.1}$$

where $\mathrm{N}_{95\%}$ is the 95% C.L. upper limit on the number of signal events observed in the data (taking into account the systematic uncertainty), $\mathcal{L}$ is the luminosity (202 pb^{-1}), and $\mathcal{A}_{\mathrm{MC}}$ is the acceptance as estimated using Monte Carlo methods. In this section we describe the GMSB SUSY models we will be using to set limits, the generator and detector simulation methods, as well as data-based corrections to the acceptances for MC deficiencies.

5.1 GMSB and Monte Carlo Simulation

We consider a GMSB model with the following parameters fixed on the minimal-GMSB Snowmass slope with a neutralino NLSP [38]:

$$N = 1, \quad M_m/\Lambda = 2, \quad \tan\beta = 15, \quad \mu > 0 \tag{5.2}$$

All theoretical expectations are obtained using the `ISAJET V7.51` MC program [39] with `CTEQ-5L` parton distribution functions (PDFs) [40]. [1] A minimum p_T of 0.5 GeV of the hard scattering is applied for all signal processes. A total of 64 thousand events were generated in 25 GeV steps of $m_{\widetilde{\chi}_1^\pm}$ from 100 to 225 GeV. Using offline version `4.9.1` we process the events through the GEANT-based [41] detector simulation, and correct the resulting efficiency with information from data measurements. For the range of Λ values of interest at the Tevatron, the supersymmetry production cross section is dominated by $\widetilde{\chi}_1^\pm\widetilde{\chi}_1^\mp$ and $\widetilde{\chi}_1^\pm\widetilde{\chi}_2^0$ production as shown in Figure 1.3 although the productions of all possible pairs of charginos and neutralinos are included in our simulation because this should produce the best exclusion region [42]. We note that in the final limit calculation we will use a K-factor of approximately 1.2 to get the next-to-leading order (NLO) prediction [43]. [2] The mass spectrum of the phenomenologically important superpartners and lightest CP–even Higgs boson, h^0, is shown in Figure 1.2. Table 5.1 gives the $m_{\widetilde{\chi}_1^\pm}$ and $m_{\widetilde{\chi}_1^0}$, total cross sections and branching ratios as a function of Λ. The kinematic variables of the two generated photons are shown in Figure 5.1.

5.2 Acceptances Calculations and Corrections

With the signal generator and detector simulation in hand we estimate the signal acceptance, $\mathcal{A}_{\rm MC}$, in Eqn. 5.1. We approximate the acceptance (excluding

[1] PYTHIA MC program gives same cross section and signal acceptance to ISAJET. A difference occurs in branching ratio. PYTHIA is higher than ISAJET since PYTHIA has missing processes of SUSY.

[2] The K-factor has a small dependence on the $\widetilde{\chi}_1^\pm$ mass and is taken from Ref. [43].

Λ (TeV)	45	54	63	72	81	90
$m_{\widetilde{\chi}_1^\pm}$ (GeV)	100	125	150	175	200	225
$m_{\widetilde{\chi}_1^0}$ (GeV)	57.5	70.6	83.6	96.6	109.6	122.7
σ_{total} (pb)	1.930	0.7510	0.3333	0.1599	0.0802	0.0419
$\mathcal{B}r(p\bar{p} \to \gamma\gamma + \widetilde{G}\widetilde{G} + X)$	0.96	0.96	0.96	0.96	0.95	0.93

Table 5.1: Some important parameters in the GMSB as a function of Λ.

branching ratio issues), as a function of $m_{\widetilde{\chi}_1^\pm}$, as the fraction of events in the MC which pass all the selection criteria in Table 3.2 and correct for deficiencies in the MC which do not reproduce the data well (see Section 5.2.5).

For expository reasons we break up the efficiency components of the acceptance, ϵ, into kinematic acceptance (E_T and detector geometry cuts), ID and isolation cuts, topology cuts (the $\Delta\phi(\not\!\!E_T-\text{jet})$ and non-collision background removal cuts) and the $\not\!\!E_T$ cut, and separately correct, $\mathcal{C}$, for the differences. Quantitatively we define:

$$\mathcal{A}_{\text{MC}} = \mathcal{A}_{Kine} \times \epsilon_{MC-ID} \times \epsilon_{Top} \times \epsilon_{Met} \times \mathcal{C}_{MC \to Data} \tag{5.3}$$

where:

$$\mathcal{A}_{Kine}(\%) = \frac{N_{\text{events}}^{\text{two photons passing kinematic acceptance criteria}}}{N_{\text{events}}^{\text{two photons from } \widetilde{\chi}_1^0 \text{ at generator level}}} \tag{5.4}$$

$$\epsilon_{MC-ID}(\%) = \frac{N_{\text{events}}^{\text{two photons passing the ID and ISO cuts}}}{N_{\text{events}}^{\text{two photons from } \widetilde{\chi}_1^0\text{, passing kinematic acceptance cut}}} \tag{5.5}$$

$$\epsilon_{Top}(\%) = \frac{N_{\text{events}}^{\text{passing the topology cuts}}}{N_{\text{events}}^{\text{passing all previous plus the ID and ISO cuts}}} \tag{5.6}$$

$$\epsilon_{Met}(\%) = \frac{N_{\text{events}}^{\text{passing } \not\!\!E_{\text{T}} \text{ threshold}}}{N_{\text{events}}^{\text{passing all previous plus the topology}}} \tag{5.7}$$

$$\mathcal{C}_{MC \to Data} = \epsilon_{Trigger} \times \mathcal{C}_{Vertex} \times \mathcal{C}_{Material} \times \mathcal{C}_{ID\ and\ Iso} \tag{5.8}$$

where $\epsilon_{Trigger}$ is the measured trigger efficiency from the data (not estimated in the MC), $\mathcal{C}_{Vertex}$ is a correction factor to take into account differences in the vertex cut efficiency, $\mathcal{C}_{Material}$ takes into account differences in photon conversion probability due to material differences in the MC and the real detector

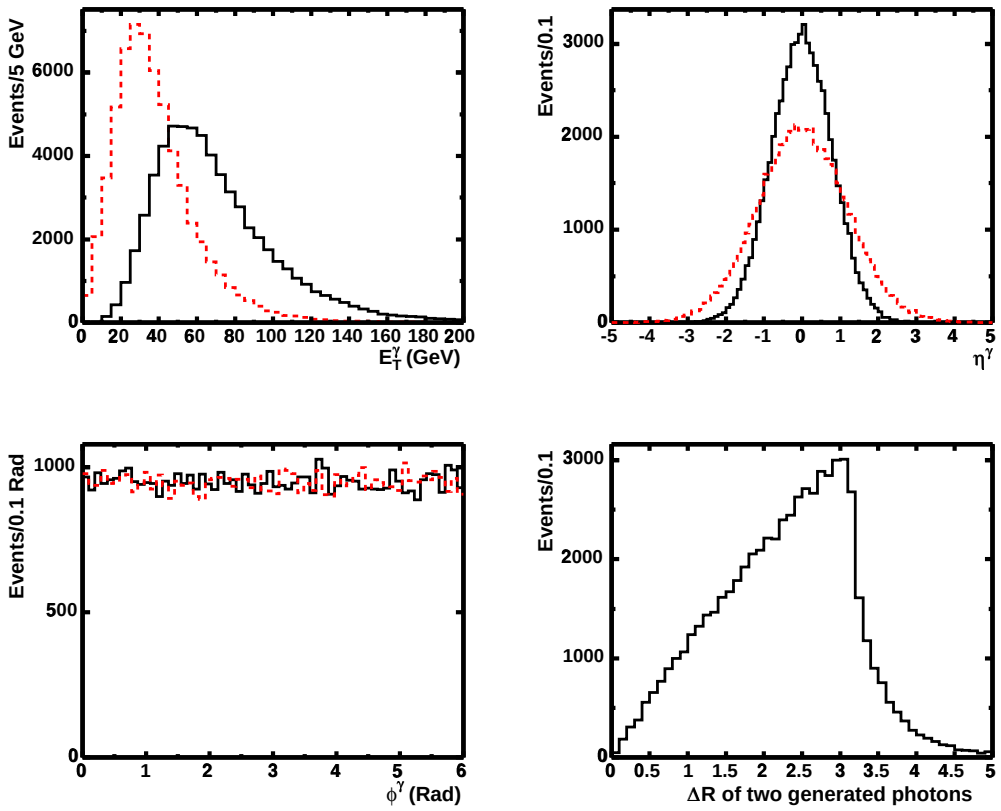

Figure 5.1: The kinematic variables of the two generated photons in GMSB: E_T, η, ϕ, and the separation in $\eta - \phi$ space of the two generated photons for a $\widetilde{\chi}_1^{\pm}$ mass of 175 GeV. The solid line indicates the primary photon and the dotted line indicates secondary photon where we have ordered the photons by E_T.

and $\mathcal{C}_{ID\ and\ Iso}$ takes into account differences between the MC and observed ID and isolation efficiencies. We estimate these in order.

5.2.1 Kinematic Acceptance

The kinematic acceptance, $\mathcal{A}_{Kine}$, is estimated to be the fraction of events from the MC which have two photons passing the following kinematic acceptance criteria divided by the number of events from the MC which have two photons from neutralinos at generator level:

- $|z_{\rm vertex}| < 60$ cm
- Two central EM clusters with $E_T > 13$ GeV
- $|\text{CES } x| < 21.0$ cm and $9.0 < |\text{CES } z| < 230.0$ cm

Differences between the MC values of the vertex efficiency and the values measured in data control samples in Section 5.2.5. After the detector simulation we require an offline electromagnetic object to be within 0.2 in a cone in $\eta - \phi$ space around the photon from the lightest neutralino at generator level; those passing all the above cuts go into the acceptance sample. The results are shown in Table 5.2 as a function of $\widetilde{\chi}_1^{\pm}$ mass.

$m_{\widetilde{\chi}_1^{\pm}}$	100 GeV	125 GeV	150 GeV	175 GeV	200 GeV	225 GeV
$\mathcal{A}_{Kine}$ (%)	24.9±0.2	28.1±0.2	30.7±0.2	32.2±0.2	33.1±0.2	33.9±0.2

Table 5.2: The kinematic acceptance, $\mathcal{A}_{Kine}$, for GMSB SUSY from the MC data samples. The errors are statistical only.

5.2.2 Identification and Isolation Efficiency

The ID and isolation selection requirements are listed in Table 3.2 and we use the MC to estimate their efficiency, and correct for differences between the MC values and the values measured in data control samples in Section 5.2.5. There

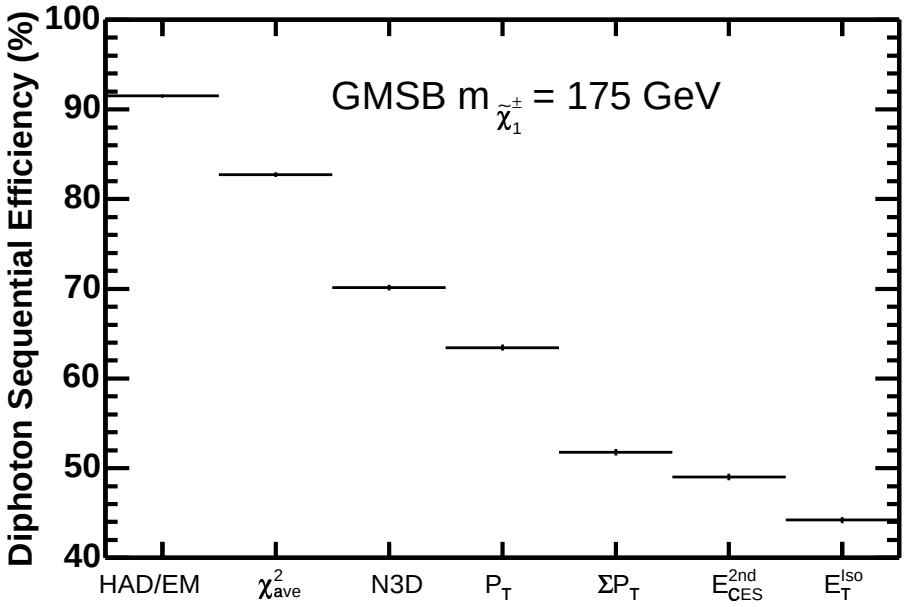

Figure 5.2: The sequential efficiency as a function of the selection criteria for varying $m_{\tilde{\chi}_1^\pm}$ for diphoton events.

are two standard ways of measuring the efficiency: the efficiency after each successive cut, and the efficiency of the cut assuming the object passes all the other cuts. Figure 5.2 shows the efficiency by placing the cuts sequentially in given order for diphoton events. Table 5.3 lists the efficiency for each individual cut as well as the total efficiency, ϵ_{MC-ID}. Note that the efficiency falls slowly as a function of the $m_{\tilde{\chi}_1^\pm}$ as more the jet energy from the cascade decay products goes up, and there are more and more jets in the event which cause the isolation variables to fail. [3]

[3] A detailed study of kinematics is given in Appendix C.

	The Efficiency for each individual cut (%) for varying $m_{\widetilde{\chi}_1^\pm}$					
Cut	100 GeV	125 GeV	150 GeV	175 GeV	200 GeV	225 GeV
Had/EM	90.5±0.2	90.6±0.2	91.2±0.2	91.5±0.2	91.7±0.2	91.9±0.2
χ^2_{ave}	92.5±0.2	91.3±0.2	90.8±0.2	90.7±0.2	89.4±0.2	90.0±0.2
N3d	79.4±0.3	79.3±0.3	78.9±0.3	78.5±0.3	76.6±0.3	76.1±0.3
P_T	72.0±0.4	72.2±0.3	72.2±0.3	72.3±0.3	70.6±0.3	70.5±0.3
ΣP_T	59.5±0.4	59.2±0.4	59.0±0.4	59.3±0.3	56.6±0.3	55.6±0.3
E^{2nd}_{CES}	84.7±0.3	85.2±0.3	85.8±0.3	86.7±0.2	86.1±0.2	86.3±0.2
E^{Iso}_T	69.9±0.4	70.6±0.3	71.1±0.3	71.3±0.3	68.7±0.3	67.7±0.3
ϵ_{MC-ID}	44.0±0.4	43.5±0.4	43.7±0.4	44.3±0.4	42.2±0.3	41.0±0.3

Table 5.3: The individual and total efficiencies for diphoton events as measured in the MC for GMSB SUSY events. The errors shown are statistical only.

5.2.3 Efficiency for Cosmic/Beam Halo, and $\not\!\!E_T$ Clean–up cuts

The selection requirements for the topology cuts, the $\Delta\phi(\not\!\!E_T-\text{jet})$ and non-collision background removal cuts, are listed in Table 3.2. We use the MC to estimate their efficiency, ϵ_{Top}, and correct for differences between the MC values and the values measured in data control samples in Section 5.2.5. The cosmic/halo rejection efficiency is approximately 99.7% for MC samples which is consistent with the results of Ref. [35], and the HADTDC cut efficiency is 97% [34]. Table 5.4 lists the efficiency of all the additional cuts. Again the efficiency decreases as the chargino mass goes up as there are more jets in the event to make the $\Delta\phi(\not\!\!E_T-\text{jet})$ cut fail. Figure 5.3 shows the distributions of $\Delta\phi$ between $\not\!\!E_T$ and the nearest or farthest jet in data and MC samples.

$m_{\widetilde{\chi}_1^\pm}$	100 GeV	125 GeV	150 GeV	175 GeV	200 GeV	225 GeV
ϵ_{Top} (%)	83.5±0.5	82.0±0.4	81.4±0.4	80.7±0.4	79.5±0.4	78.5±0.5

Table 5.4: The efficiency for GMSB events to pass the cosmic and beam halo rejection, and the $\not\!\!E_T$ clean–up cuts. Note that the efficiency decreases as the chargino mass goes up, producing more jets which makes the $\Delta\phi(\not\!\!E_T-\text{jet})$ cut fail. The errors are statistical only.

5.2.4 Efficiency of the $\not\!\!E_T$ Requirement

Figure 5.4 shows the $\not\!\!E_T$ distribution for the MC samples of the GMSB model with the background predictions. We estimate the efficiency of the $\not\!\!E_T$ threshold requirements, ϵ_{Met} (%) as a function of the mass of the $\widetilde{\chi}_1^\pm$ using the MC. The results, as a function of various $\not\!\!E_T$ cuts, are given in Table 5.5.

5.2.5 Corrections for MC Deficiencies

While the MC does a good job of modeling many quantities of interest for the final acceptance there are deficiencies in the MC which do not reproduce

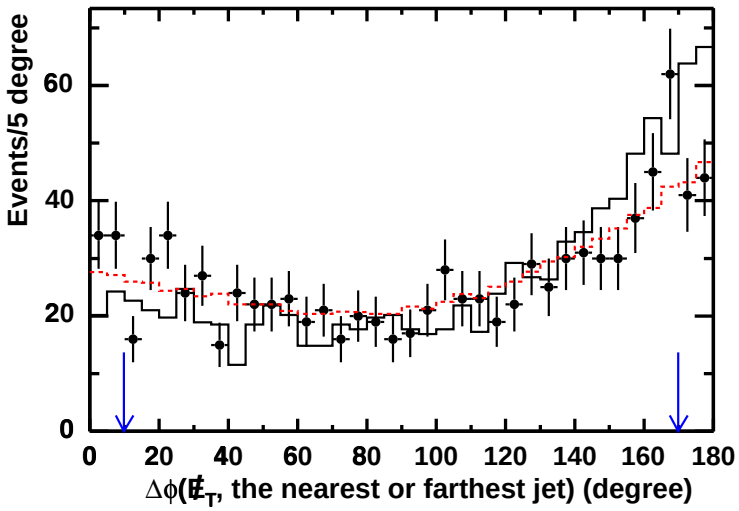

Figure 5.3: The distributions of $\Delta\phi$ between $\not\!\!E_T$ and the nearest or farthest jet in data (points), QCD background prediction (histogram), and GMSB MC samples (dotted). The QCD background prediction and GMSB MC samples are normalized to data. The arrows indicate the $\not\!\!E_T$ clean–up cuts. Note that we have superimposed the GMSB results for all models together.

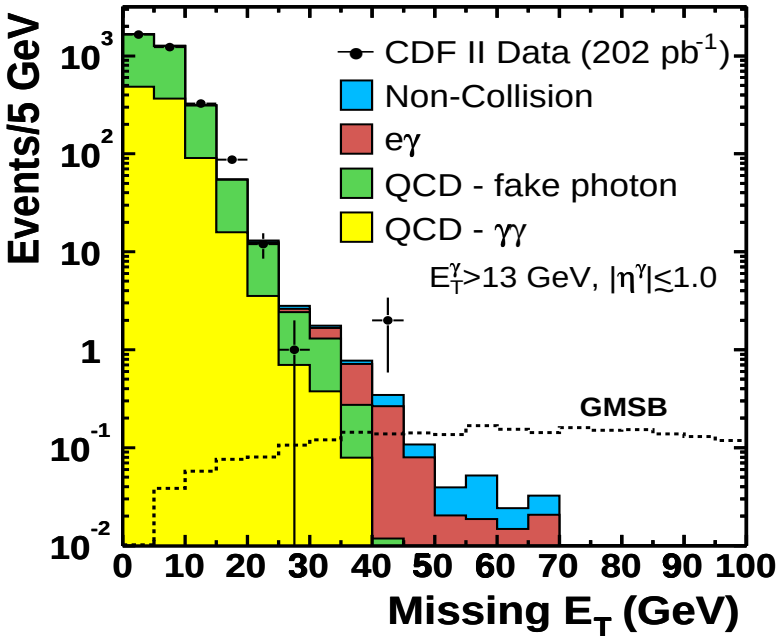

Figure 5.4: The $\not\!\!E_T$ distribution for the GMSB MC samples with $m_{\widetilde{\chi}_1^\pm}$ of 175 GeV. For 202 pb^{-1}, $\sim$ 3 events are expected in an overall region of $\not\!\!E_T$.

$\not\!\!E_T$	100 GeV	125 GeV	150 GeV	175 GeV	200 GeV	225 GeV
25 GeV	77.3±0.6	83.9±0.5	88.4±0.4	91.2±0.3	91.9±0.3	94.0±0.3
35 GeV	61.4±0.6	71.9±0.6	78.7±0.5	83.7±0.4	85.5±0.4	88.2±0.4
45 GeV	43.7±0.7	58.2±0.6	67.2±0.6	74.3±0.5	78.1±0.5	82.2±0.5
55 GeV	28.1±0.6	44.7±0.6	55.0±0.6	65.1±0.6	70.1±0.6	75.4±0.5

Table 5.5: The efficiency for GMSB diphoton events to pass various $\not\!\!E_T$ threshold. The errors are statistical only.

the data well in other areas. This includes the trigger efficiency which is not simulated in the MC, differences in the vertex cut efficiency, differences in photon conversion probability due to material differences in the MC and the real detector and differences between the MC and observed ID and isolation efficiencies. Again we estimate the correction factor, $\mathcal{C}_{MC\to Data}$, based on studies performed by other analysis groups and using the relation in Eqn. 5.8.

For the trigger efficiency of MC data sample, we take $\epsilon_{Trigger} = 99.7\%$ from Ref. [33]. The vertex efficiency of the $|z_{\rm vertex}| \leq 60$ cm cut has been measured in Ref. [44] to be 95.1%. In the MC it is estimated to be 96.5%. We take the correction factor $\mathcal{C}_{Vertex} = \frac{95.1\%}{96.5\%} = 0.986$. [4] The diphoton ID efficiency per event depends on the conversion probability which depends on the amount of material in the detector. Since this is underestimated in the `4.9.1` simulation we take a correction factor, $\mathcal{C}_{Material} = 0.926$ from Ref. [45].

The last effect is to correct for ID and isolation efficiency differences between the simulation and data. This is done using a sample of $Z \to ee$ events since the shapes of the variables which go into the efficiency calculations for electrons should, in most cases, be very similar to photons. The data studied was approximately 202 pb^{-1} from the inclusive high P_T electron trigger. For each event we required the presence of a central electron with $E_T > 20$ GeV passing the following cuts: $0.8 < E/p < 1.5$, $\Delta X < 3$ cm, $\Delta Z < 5$ cm, LShr< 0.2, $\mathrm{E_T^{Iso}} < 0.1$, and Had/EM< 0.125 (these cuts were the same or

[4] We note that while the vertex finding efficiency is high, in offline version `4.8.4` it is not 100% for all processes with low multiplicity. GMSB SUSY produces very large multiplicities, and in the MC has an efficiency of 100%. We take no additional correction for the vertex finding efficiency, and take a 3% systematic error for this effect.

tighter than the trigger cuts). In addition, we then required a second cluster with $E_T > 20$ GeV and $0.9 < E/p < 1.1$ (to avoid bremsstrahlung electrons which might cause the CES χ^2 cut to be mis-measured as inefficient), both legs to have opposite charges, and a mass between 75 and 105 GeV. If both electrons pass the tighter requirements then one was chosen at random to be the "trigger" electron. Comparing the efficiencies between Z data and MC samples (we used the ztop0e based on offline version `4.9.1` which is in Stntuple) shows that the ID efficiency per photon is corrected by 3.5% per photon. Table 5.6 gives the relative efficiencies[5] and Figure 5.5 shows the corrected total efficiency of MC sample versus E_T to compare with the efficiency of data. From the table we take $\mathcal{C}_{ID\ and\ Iso} = (\frac{84.6\%}{87.7\%})^2 = 0.93$. Plugging in the numbers we find $\mathcal{C}_{MC \to Data} = 0.997 \times 0.986 \times 0.926 \times 0.930 = 0.847$.

	Relative Efficiency (%)		
Cut	Data	MC	$\Delta\epsilon$
Had/EM	99.2 ± 0.2	99.0 ± 0.1	$+0.2$
E_T^{Iso}	95.9 ± 0.5	95.1 ± 0.2	$+0.8$
χ^2_{ave}	97.5 ± 0.4	98.9 ± 0.1	-1.4
N3d	98.5 ± 0.3	98.8 ± 0.1	-0.3
P_T	96.1 ± 0.5	97.4 ± 0.2	-1.3
ΣP_T	96.5 ± 0.4	98.0 ± 0.1	-1.5
Total	84.6 ± 0.8	87.7 ± 0.3	-3.5

Table 5.6: The efficiencies for an unbiased $Z \to ee$ leg to pass the ID cuts, and their comparisons of MC to data. The errors shown are statistical only.

[5] Relative efficiency $= N_{\text{events}}^{\text{passing cut and all previously applied cuts}} / N_{\text{events}}^{\text{passing all previously applied cuts}}$.

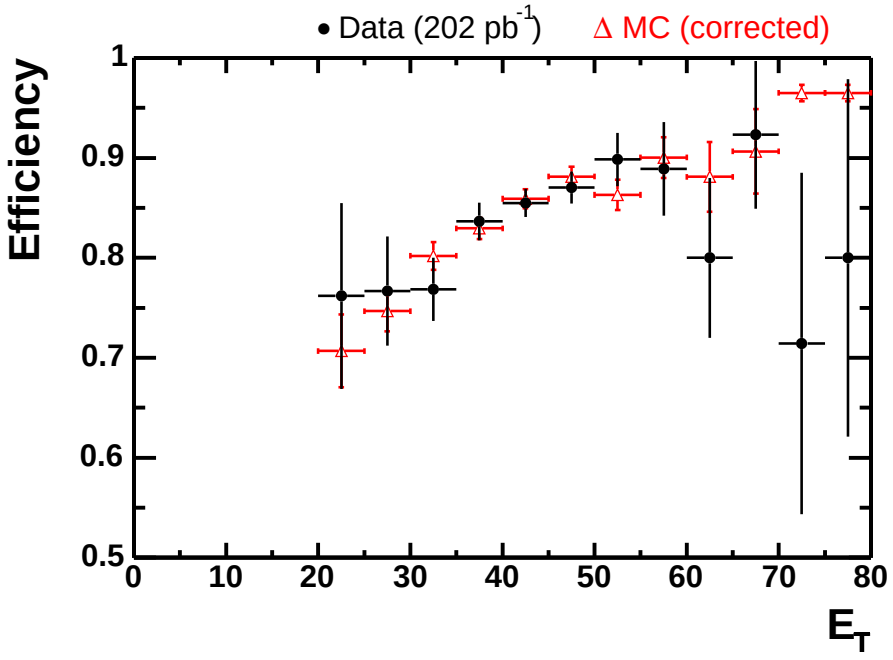

Figure 5.5: The ID and isolation efficiency for a single electron versus E_T as measured using $Z \to ee$ data and MC samples.

5.2.6 Total Acceptance

Collecting all the pieces we find the final signal acceptance, $\mathcal{A}_{\rm MC}$ and tabulate the results, typically 3% to 8%, in Table 5.7 with the final $\not\!\!E_T$ cut of 45 GeV (see Chapter 6). The acceptance, as functions of $m_{\tilde{\chi}_1^\pm}$ and $m_{\tilde{\chi}_1^0}$, is shown in Figure 5.6. For completeness, we have added the results for different $\not\!\!E_T$ threshold requirements.

$m_{\tilde{\chi}_1^\pm}$	100 GeV	125 GeV	150 GeV	175 GeV	200 GeV	225 GeV
$\mathcal{A}_{\rm MC}$ (%)	3.4 ± 0.1	4.9 ± 0.1	6.2 ± 0.1	7.2 ± 0.1	7.3 ± 0.1	7.6 ± 0.1

Table 5.7: The full, corrected signal acceptances, $\mathcal{A}_{\rm MC}$, from the MC samples using the $\not\!\!E_T > 45$ GeV requirement. The errors are statistical only.

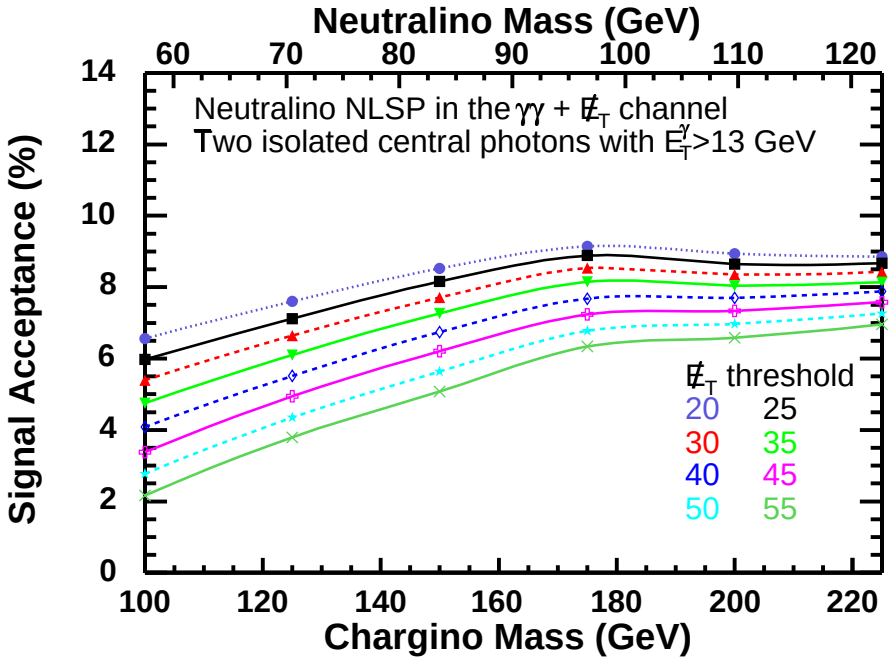

Figure 5.6: The final signal acceptance for the GMSB model as functions of $m_{\tilde{\chi}_1^\pm}$ and $m_{\tilde{\chi}_1^0}$. While the final analysis uses a $\not\!\!E_T > 45$ GeV requirement, for completeness we include the results for $\not\!\!E_T$ threshold varying from 20 to 55 GeV.

5.3 Systematic Uncertainties on the Acceptance

The systematic uncertainty on the signal acceptance was estimated by taking into account the following sources. All systematic errors were combined in quadrature to give a total systematic uncertainty of 18%.

- Selection cut efficiencies (13%)
  Following the results in Ref. [45] we have estimated the relative systematic uncertainties in the efficiency of the photon identification and isolation requirements. Using a comparison of $Z^0 \to ee$ MC to a study of energy deposits in random cones with various jet samples, the differences in efficiency by the standard cut ordering are estimated: Had/EM (1%), energy isolation (5%), χ^2 (2%), N3D (0.5%), track p_T (1%), track isolation (1%), fiducial (3%) and conversions (1.2%). The each uncertainty is added in quadrature, approximately 6.5% per photon (or $\approx$ 13% for the pair) which is consistent with the results of Ref. [45].

- PDFs uncertainty ($+1\% \sim -5\%$)
  5 `MRST` sets were used to investigate the PDFs dependence in the signal acceptance. Changes of up to $+1\% \sim -5\%$ in the final acceptance result were observed. The maximum uncertainty of 5% is choosen.

- Initial/Final State Radiation, ISR/FSR (10%)
  The effects of ISR and FSR are determined by the following procedure; turn ISR off only or turn FSR off only. This procedure gave rise to a systematic error averaging 10% on the final signal acceptance.

- Q^2 (3%)
  We examined the acceptance changes varying the scale from $0.25 \times Q^2$ to $4 \times Q^2$. Changes of up to 3% in the final result were observed.

- MC statistics (1%)
  64 thousand events are generated for each $m_{\widetilde{\chi}_1^+}$ point. The statistical uncertainty by roughly 1% added in quadrature for all selection criteria.

- Luminosity (6%)
  The estimated uncertainty in the CLC measurement is 4.4% and is mostly due to the uncertainty in the CLC acceptance (4.0%). If we use the CDF measurement of the inelastic cross-section for normalization, (with a 3.8% uncertainty), the total uncertainty in the luminosity would be 6%.

Chapter 6

Optimization and Final Results

By three months, he produces the most delightful laughter and will now respond to a smile by smiling back.

- in BabyTalk

The kinematic selection requirements defining the final data sample are determined by a study to optimize the expected limit, *i.e.*, without looking at the signal region data. To compute the expected 95% C.L. cross section upper limit we combine the predicted signal and background estimates with the systematic uncertainties using a Bayesian method [46] and follow the prescription described in Ref. [47]. The expected limits are computed as a function of $\not\!\!E_T$, E_T^γ, and $\Delta\phi(\not\!\!E_T,j)$ selection requirements. We find that the best limit is predicted with the selection described above for the diphoton candidate sample, and $\not\!\!E_T >$ 45 GeV. The statistical analysis indicates that the most probable expected result would be an exclusion of $m_{\widetilde{\chi}_1^\pm}$ less than 161 GeV/c^2 and $m_{\widetilde{\chi}_1^0}$ less than 86 GeV/c^2.

6.1 Expectations Vs. Different Cuts

The default $\Delta\phi(\not\!\!E_T-\text{jet})$ cut removes events when there is a jet which is not in the range $10^\circ < \Delta\phi < 170^\circ$. This was done to remove pathological jets from producing large $\not\!\!E_T$ and fake events. Several choices of $\Delta\phi$ cut were chosen to test the effect on the expected chargino mass limit to see if significant benefits could be reaped if we loosened this cut and found other ways to remove pathological events. We investigated:

- the jet nearest the $\not\!\!E_T$ has to be more than 0°–20° from the $\not\!\!E_T$
- the jet most opposite the $\not\!\!E_T$ must be more than 160°–180° from the $\not\!\!E_T$
- both at the same time.

For each $\Delta\phi$ cut the expected limit on chargino mass is calculated using the MC acceptance from Chapter 5 and the background estimate from Chapter 4. The result is shown in Figure 6.1 for two different values of the $\not\!\!E_T$ cut. Since removing the $\Delta\phi$ cut, which appears optimal, only raises the expected limit from 161 to 170 GeV, we choose to remain with the $10^\circ \leq \Delta\phi \leq 170^\circ$ for reasons of robustness.

The same procedure was performed to maximize the chargino mass limit as a function of photon E_T and $\not\!\!E_T$. The expected chargino mass limits are estimated for photon E_T thresholds of $13 \sim 25$ GeV and $\not\!\!E_T$ thresholds of $20 \sim 55$ GeV, respectively. Figure 6.2 shows the expected 95% C.L. lower mass limit on the lightest chargino as a function of photon E_T for a number of $\not\!\!E_T$ cut for the default $\Delta\phi$ requirements. We find our cut of $E_T^\gamma > 13$ GeV and $\not\!\!E_T > 45$ GeV to be optimal. Finally, using the nominal values of the photon E_T and $\Delta\phi$ cuts Figure 6.3 shows that $\not\!\!E_T > 45$ GeV provides the best expected mass limit.

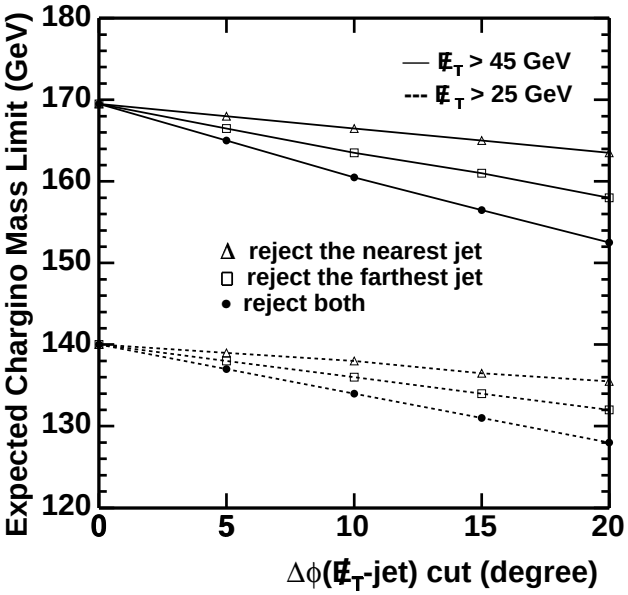

Figure 6.1: The expected 95% C.L. lower mass limit on the lightest chargino as a function of the $\Delta\phi(\not\!\!E_T-$jet) cut.

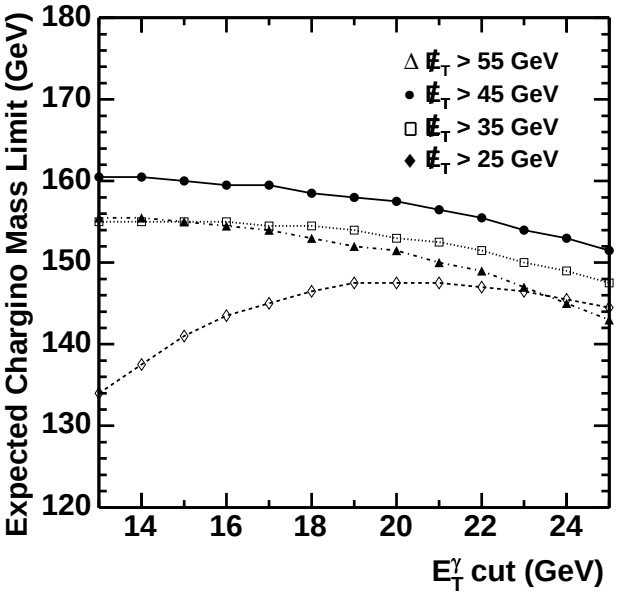

Figure 6.2: The expected 95% C.L. lower mass limit on $\widetilde{\chi}_1^{\pm}$ as a function of the photons' E_T for each $\not\!\!E_T$ cut (25, 35, 45 and 55 GeV) for the default requirements.

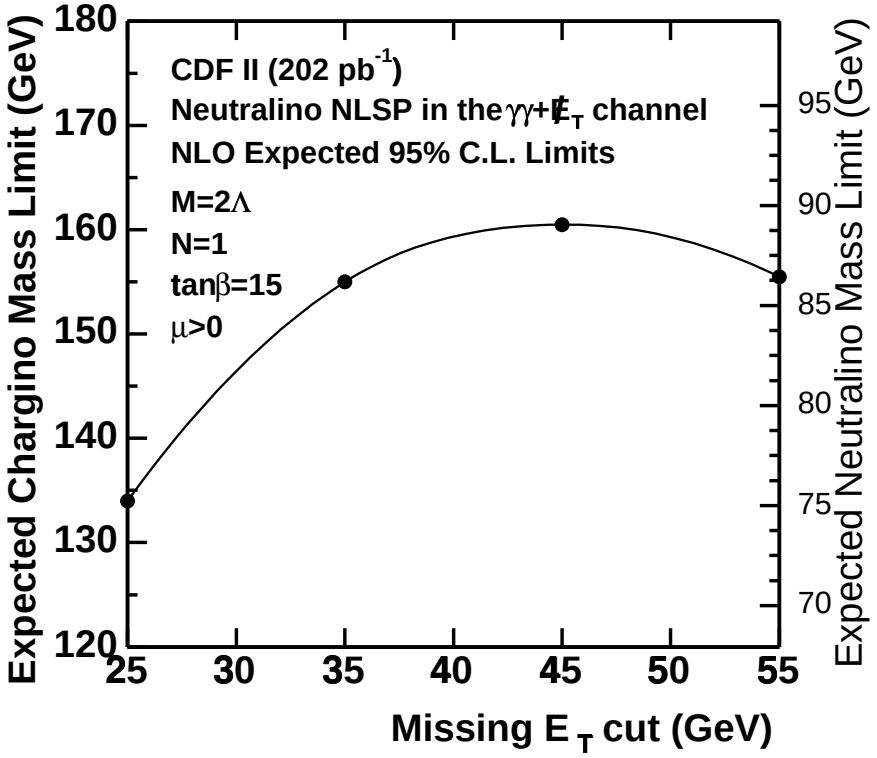

Figure 6.3: The expected 95% C.L. lower mass limit on the lightest chargino and the lightest neutralino as a function of $\not\!\!E_T$.

6.2 Final Limits from Data

In the data signal region, with $\not\!\!E_T > 45$ GeV, we observe zero events. Taking into account the 18% systematic uncertainty we set a 95% C.L. upper limit of 3.3 signal events. Figure 6.4 shows the observed cross section limits as functions of $m_{\tilde{\chi}_1^\pm}$ and $m_{\tilde{\chi}_1^0}$ along with the theoretical LO and NLO production cross sections. Using the NLO predictions we set a limit of $m_{\tilde{\chi}_1^\pm} > 167$ GeV/c^2 at 95% C.L. From mass relations in the model, we equivalently exclude $m_{\tilde{\chi}_1^0} <$ 93 GeV/c^2 and Λ < 69 TeV. The Run I limits in this channel using similar models were 120 GeV/c^2 for the lightest chargino in CDF [4] and 150 GeV/c^2 in DØ [12]. Earlier exclusion interpreted as lower limit on the $m_{\tilde{\chi}_1^0}$ within similar parameter set is 100 GeV from combined LEP II results [15].

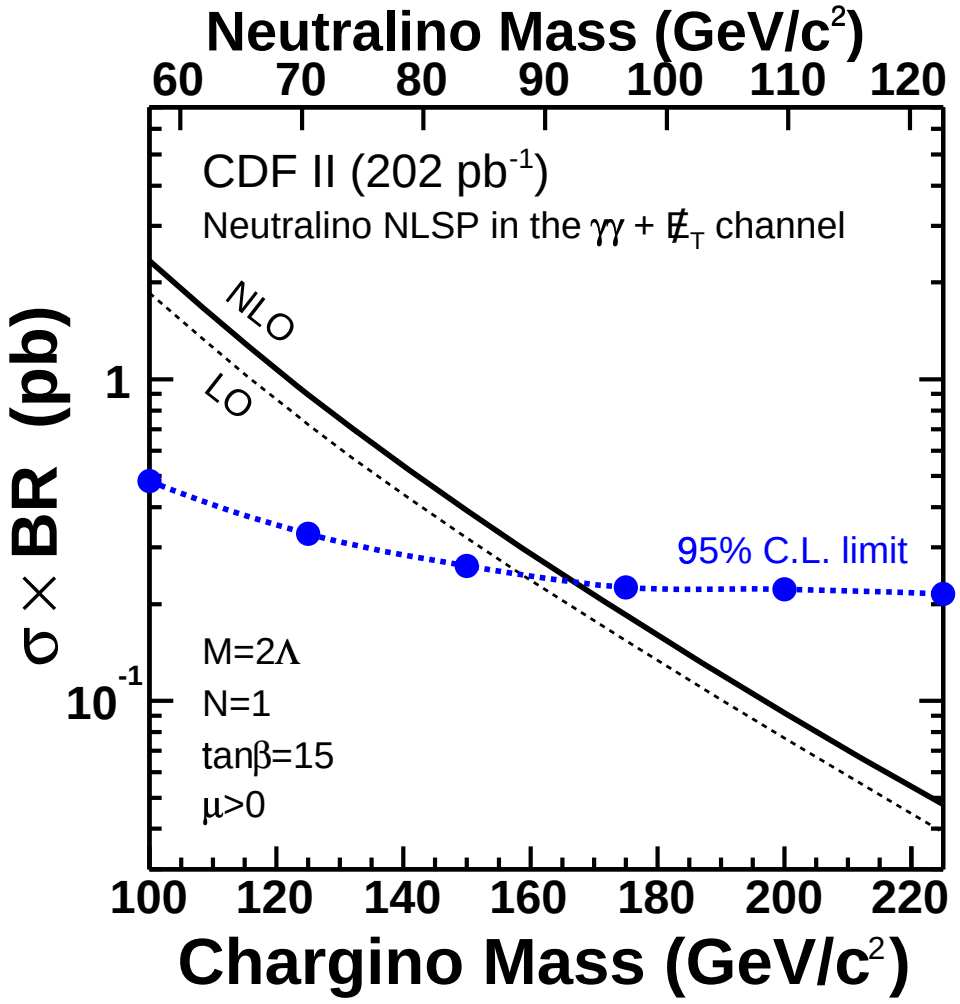

Figure 6.4: The 95% C.L. upper limits on the total production cross section times branching ratio versus $m_{\widetilde{\chi}_1^\pm}$ and $m_{\widetilde{\chi}_1^0}$ for the light gravitino scenario using the parameters proposed in Ref. [38]. The lines show the experimental limit and the LO and NLO theoretically predicted cross sections. We set limits of $m_{\widetilde{\chi}_1^\pm} > 167$ GeV/c^2 and $m_{\widetilde{\chi}_1^0} > 93$ GeV/c^2 at 95% C.L.

Chapter 7

Conclusions

In the first three months, social interaction typically occurs between infant and adult, without other objects or events serving as a focus of the interaction.

- in BabyTalk

In conclusion, we have searched 202 pb^{-1} of inclusive diphoton events at CDF Run II for anomalous production of missing transverse energy as evidence of new physics. We find good agreement with standard model expectations. We find no events above the *a priori* $\not\!\!E_T$ threshold, and thus observe no new $ee\gamma\gamma\not\!\!E_T$ candidates. Using these results, we have set limits on the lightest chargino $m_{\tilde{\chi}_1^\pm} > 167$ GeV/c^2 and $m_{\tilde{\chi}_1^0} > 93$ GeV/c^2 at 95% C.L. in a GMSB model. This limit is an improvement over previous CDF and DØ limits and is comparable to LEP II for similar models [15].

Appendix A

A detailed comparison

In this section we present some more in-depth comparisons between the control and diphoton candidate samples to convince ourselves that it can be used in Section 4.2 to model the data in the large $\not\!\!E_T$ signal region.

A.1 CES/CPR Subtracted Quantities

The $\not\!\!E_T$ resolution is a function of the $\Sigma E_T^{\text{Corrected}}$. As shown in Figure 4.3 the diphoton and control samples are similar but disagree by $\approx 6\%$. As another comparison, Figure A.1 compares the direct $\gamma\gamma$ component of the diphoton candidate sample using the CES/CPR background subtraction methods. While the comparison is statistically limited, again the shapes are very similar and there is no reason to believe the control sample should not do a good job of estimating the $\not\!\!E_T$ distribution after correction.

A.2 Kinematic variables

Figures A.2 through A.5 compare a number of kinematic distributions from diphoton and control samples. Figure A.2 shows that the azimuthal angle and detector η distributions are qualitatively satisfactory. Figure A.3 shows the E_T of the primary photon candidates, the E_T of the secondary photon candi-

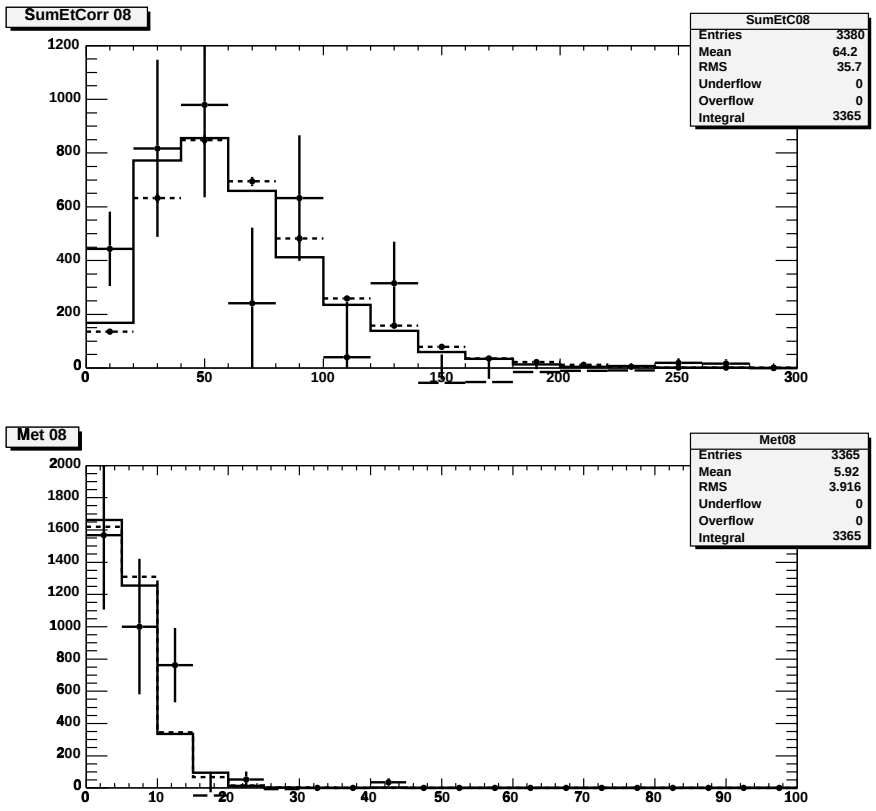

Figure A.1: The $\Sigma E_T^{\text{Corrected}}$ (top) and $\not\!\!E_T$ (bottom) distributions of the CES/CPR background subtracted diphoton candidate sample (points), the full diphoton candidate sample (solid histogram), and the control sample (dashed histogram). All are normalized to the full diphoton candidate sample size.

dates, and the difference in azimuthal angle between the two photons. Various combinations of other $\Delta\phi$ variables are shown in Figure A.4. Figure A.5 shows the distributions of $\Sigma E_T^{\text{Corrected}}$, unclustered $\Sigma E_T^{\text{Corrected}}$, jet multiplicity and E_T of the jets.

All cases are in reasonable agreement between the diphoton candidate sample and control sample is seen. This confirms that the control sample has a similar calorimetric response and resolution to diphoton candidate sample.

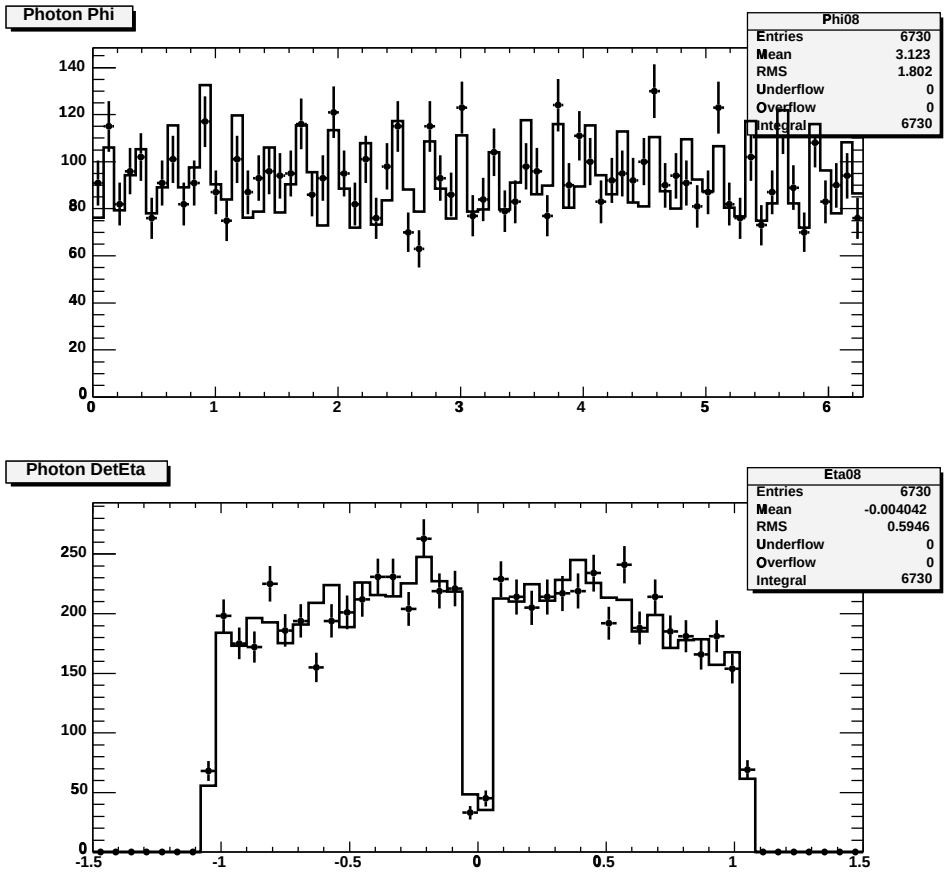

Figure A.2: The azimuthal angle (top) and detector η (bottom) distribution of photon candidates. The points are from the diphoton candidate sample, and the histogram is the distribution from control sample, normalized to the number of diphoton candidates.

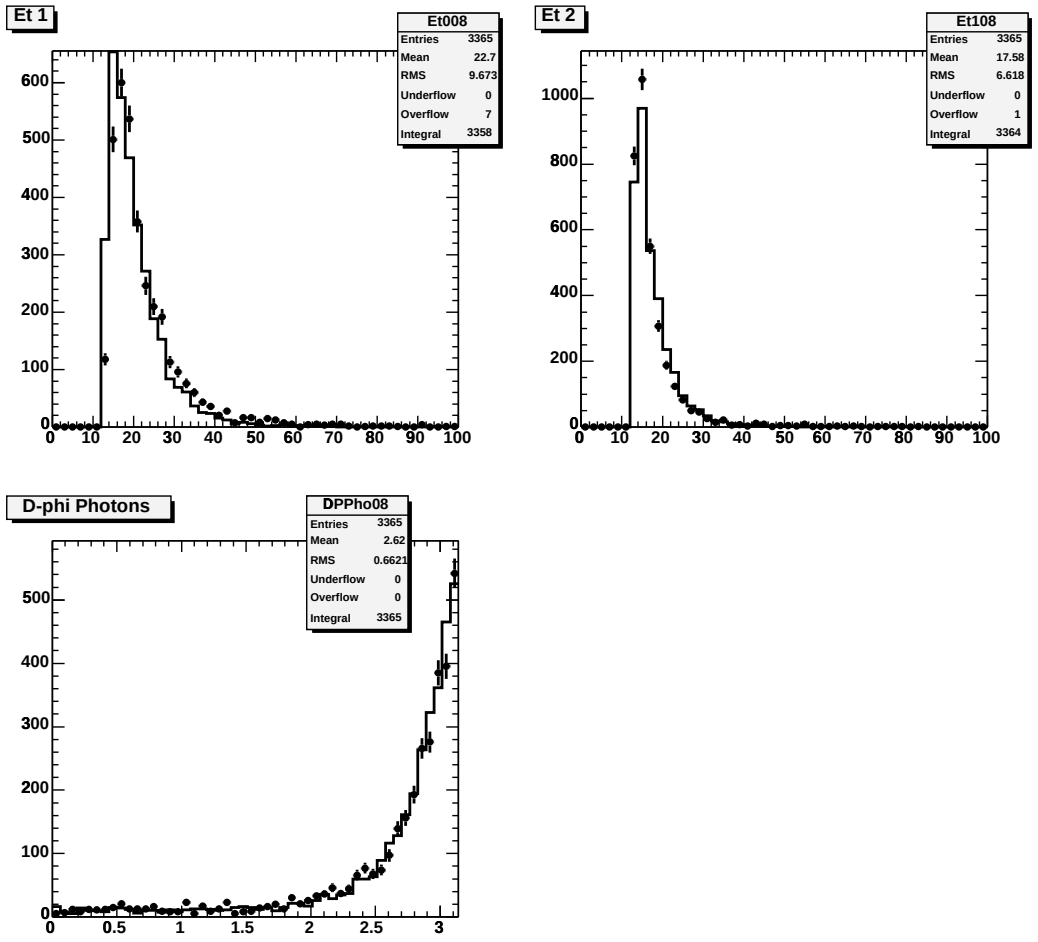

Figure A.3: The E_T of the primary photon candidates (top left), E_T of the secondary photon candidates (top right), and difference in azimuthal angle between the two photons (bottom left). The points are from the diphoton candidate sample, and the histogram is the distribution from control sample, normalized to the number of diphoton candidates.

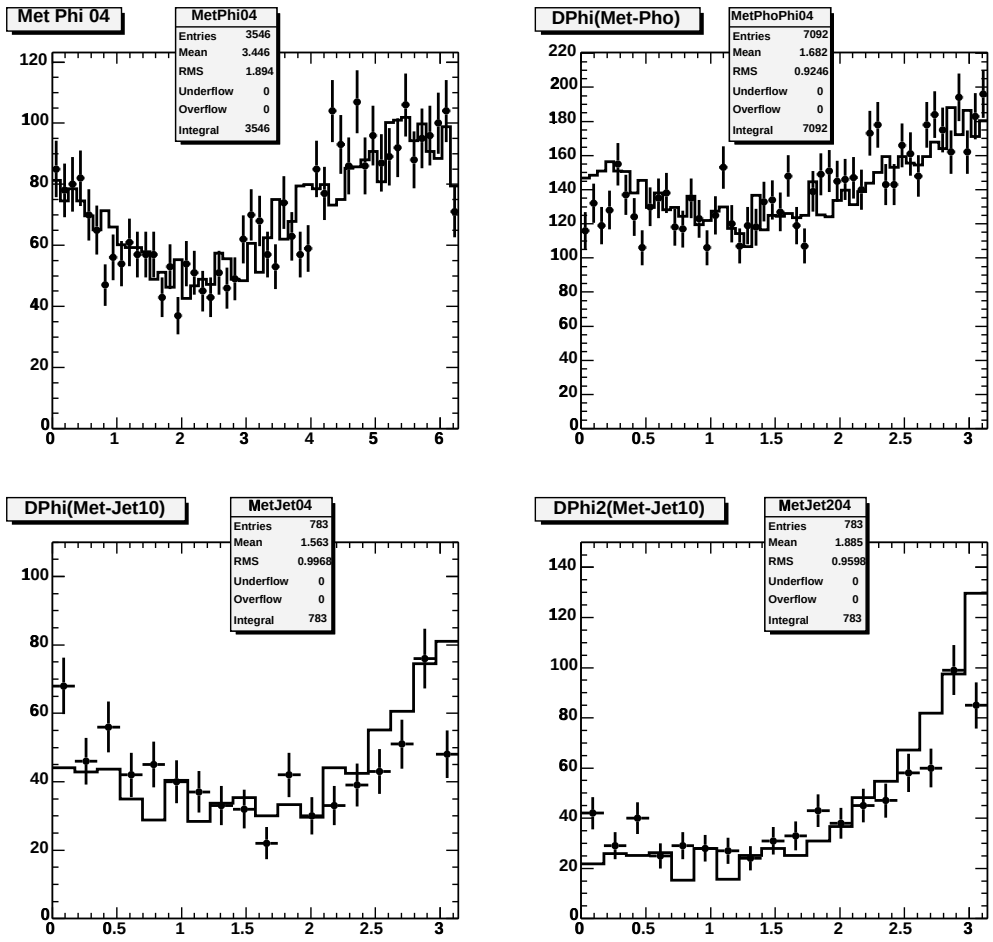

Figure A.4: Some azimuthal angle distribution comparisons. The ϕ of the $\not\!\!E_T$ is shown in the top left and the $\Delta\phi(\not\!\!E_T - \gamma)$ is shown in the top right. The bottom left is the azimuthal angle difference between $\not\!\!E_T$ and the jet nearest to the $\not\!\!E_T$ and the bottom right is the azimuthal angle difference between $\not\!\!E_T$ and the jet farthest from the $\not\!\!E_T$. The points are from the diphoton candidate sample, and the histogram is the distribution from control sample, normalized to the number of diphoton candidates.

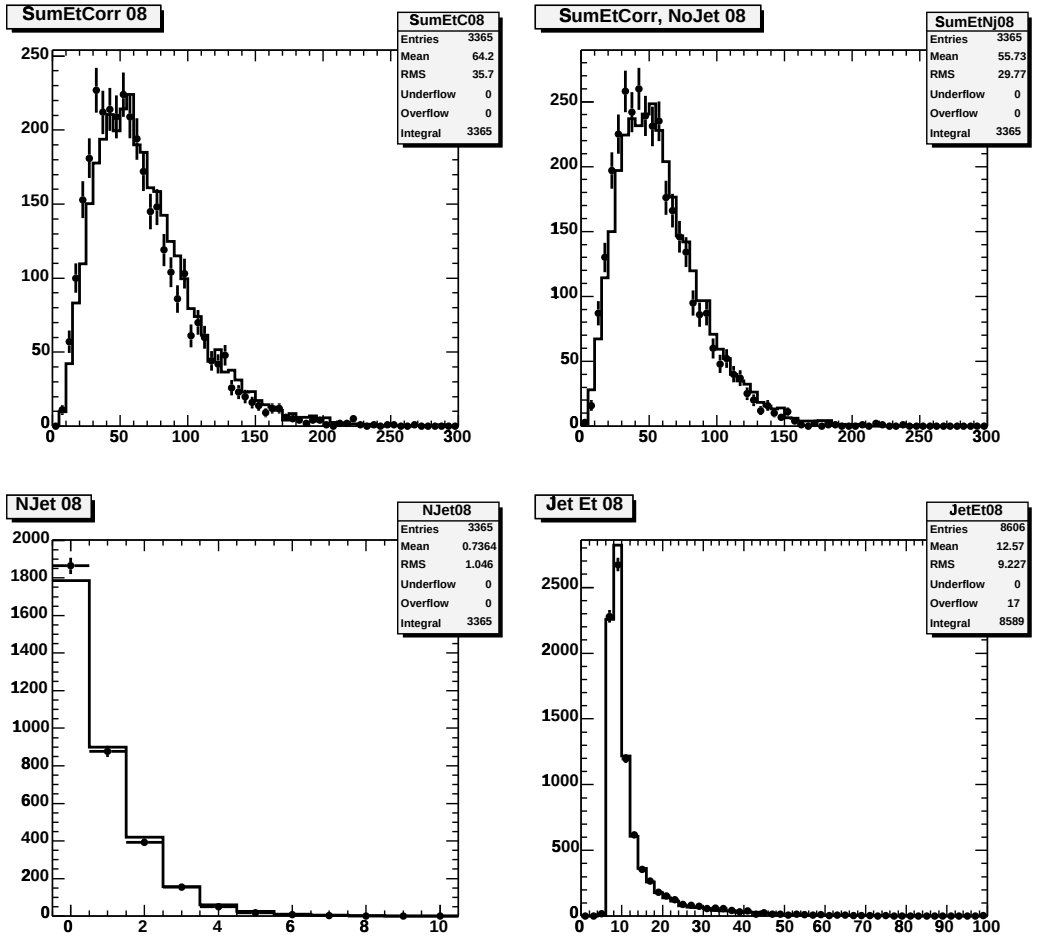

Figure A.5: The distributions of $\Sigma E_T^{\text{Corrected}}$(top left), unclustered $\Sigma E_T^{\text{Corrected}}$ (top right), jet multiplicity (bottom left) and E_T of the jets (bottom right). The points are from the diphoton candidate sample, and the histogram is the distribution from the control sample, normalized to the number of diphoton candidates.

Appendix B

Gaussian $\not\!\!E_T$ Resolution Model

B.1 Problems with the Model

As described in Section 4.2, $\not\!\!E_T$ distributions, when there is no intrinsic $\not\!\!E_T$, can be estimated using $\Sigma E_T^{Corrected}$ in the event. In Run I we corrected for differences between $\Sigma E_T^{Corrected}$ in a $Z \to ee$ control sample and in the diphoton signal sample using a method which assumed that the $\not\!\!E_T$ distribution was well modeled by Gaussian errors on the resolution [4]. However, at this point in time, with the current calibrations, this method does not reproduce back the distribution it was taken from so we have abandoned it for now. In this Appendix we discuss these differences.

For our studies we used a sample of $\sim$ 3.5K $Z^0 \to e^+e^-$ events selected with two tight, isolated central electrons with $76 < M_{e^+e^-} < 106$ GeV as described in Table 3.4. Figs. B.1 and B.2 shows the $\not\!\!E_T$ in the x direction, $\not\!\!E_T^x$, and the y direction, $\not\!\!E_T^y$. The distributions are separated into 12 bins of $\Sigma E_T^{Corrected}$ centered on $\Sigma E_T^{Corrected}$ = 10, 25, 35, 45, 55, 65, 75, 87.5, 105, 125 and 167.5 GeV respectively. While the width, $\sigma(\not\!\!E_T^x)$ and $\sigma(\not\!\!E_T^y)$, clearly increase as a function of $\Sigma E_T^{Corrected}$ as expected, and there is an easily fixable offset in both $\not\!\!E_T^x$ and $\not\!\!E_T^y$, each bin is not well modeled by a Gaussian as there are tails to high values.

While the tails are visible, we investigate how much affect this has on our

ability to use a Gaussian met model to reproduce the original data. Following the methods in Ref. [4], since $Z^0 \to e^+e^-$ events have no intrinsic $\not\!\!E_T$ the expected $\not\!\!E_T$ distribution can be predicted from the mean values of $\not\!\!E_T^x$ and $\not\!\!E_T^y$ and the $\sigma(\not\!\!E_T^x)$ and $\sigma(\not\!\!E_T^y)$ resolution alone. The expected $\not\!\!E_T$ distribution is estimated by smearing the x and y components by the $\not\!\!E_T^x$ and $\not\!\!E_T^y$ resolution (estimated as a function of $\Sigma \mathrm{E_T^{Corrected}}$) and centered on the measured mean values. The means and resolutions are determined using the best fits in Figs B.1 and B.2 with the results plotted in Figure B.3 as a function of the $\Sigma \mathrm{E_T^{Corrected}}$. In the region $\Sigma \mathrm{E_T^{Corrected}} < 200$ GeV the distributions can be parameterized by

$$\sigma(\not\!\!E_T^x) = (3.15 \pm 0.12) + (0.024 \pm 0.002) \times \Sigma \mathrm{E_T^{Corrected}} \quad \text{(B.1)}$$

$$\sigma(\not\!\!E_T^y) = (3.32 \pm 0.11) + (0.018 \pm 0.002) \times \Sigma \mathrm{E_T^{Corrected}} \quad \text{(B.2)}$$

$$\text{Mean } (\not\!\!E_T^x) = (\ 0.061 \pm 0.145) + (\ 0.014 \pm 0.002) \times \Sigma \mathrm{E_T^{Corrected}} \quad \text{(B.3)}$$

$$\text{Mean } (\not\!\!E_T^y) = (-0.035 \pm 0.145) + (-0.011 \pm 0.002) \times \Sigma \mathrm{E_T^{Corrected}} \quad \text{(B.4)}$$

The $\not\!\!E_T$ distribution from $Z^0 \to e^+e^-$ data is shown along with the expectations in Figure B.4 The data do not agree well with expectations above about 15 GeV. We also checked a fit of the $\not\!\!E_T$ distribution for each $\Sigma \mathrm{E_T^{Corrected}}$ bin which is shown in Figure B.5. Since the $\not\!\!E_T$ resolution is not Gaussian and has asymmetric tails in $\not\!\!E_T(x, y)$, each bin is under-predicted. For these reasons we conclude that since we can reproduce the $\not\!\!E_T$ distribution from which the model parameters are drawn that we will not use the Gaussian $\not\!\!E_T$ model until the $\not\!\!E_T(x, y)$ distributions become symmetric and the $\not\!\!E_T$ parameterization works well.

B.2 Another study

To understand, and potentially fix this problem, we did a number of studies of the correlation between $\not\!\!E_T^x$ and $\not\!\!E_T^y$. Figures B.6 and B.7 shows $\not\!\!E_T^x$ versus $\not\!\!E_T^y$ and Mean $(\not\!\!E_T^x)$ vs. Mean $(\not\!\!E_T^y)$ for various regions in $\Sigma \mathrm{E_T^{Corrected}}$. Since there is no slope in $\not\!\!E_T(x, y)$ and the linear correlation coefficient between $\not\!\!E_T^x$ and

$\not\!\!E_T^y$ is -0.019, we concluded that $\not\!\!E_T^x$ and $\not\!\!E_T^y$ are uncorrelated, and there is not much to do at this point except wait for the next set of calibrations. Since the initial writing of this document, this set of calibrations has come out, but in the interests of time, we have not re-done the study since the Histogrammed met method, described in Section 4.2 works just fine.

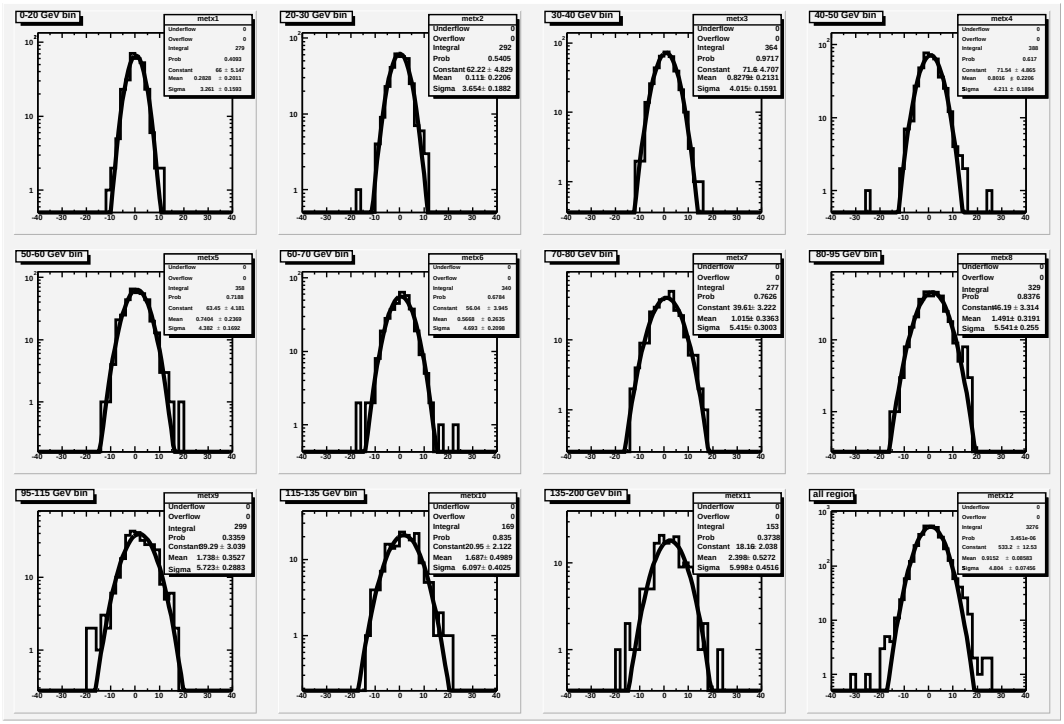

Figure B.1: The $\not\!\!E_T^x$ for various regions in $\Sigma E_T^{\text{Corrected}}$. They are (top to bottom, left to right) centered on $\Sigma E_T^{\text{Corrected}} = 10$, 25, 35, 45, 55, 65, 75, 87.5, 105, 125 and 167.5 GeV respectively. In many of the plots the tail of the distribution is poorly modeled by a Gaussian fit.

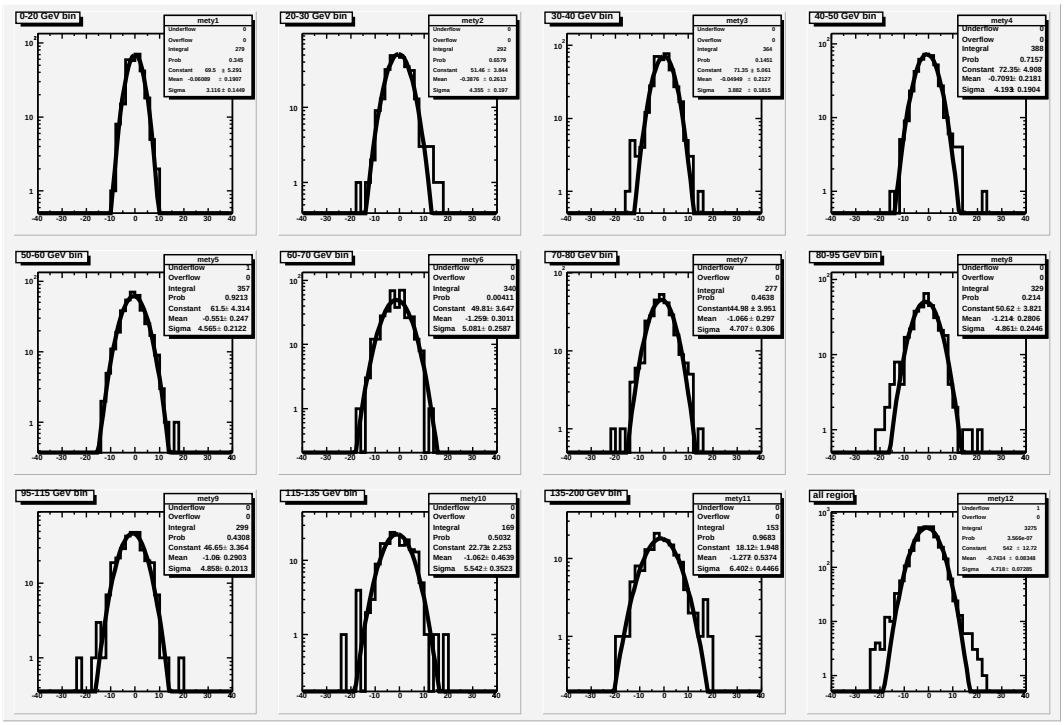

Figure B.2: The $\not\!\!E_T^y$ for various regions in $\Sigma E_T^{\text{Corrected}}$. They are (top to bottom, left to right) centered on $\Sigma E_T^{\text{Corrected}} = 10$, 25, 35, 45, 55, 65, 75, 87.5, 105, 125 and 167.5 GeV respectively. In many of the plots the tail of the distribution is poorly modeled by a Gaussian fit.

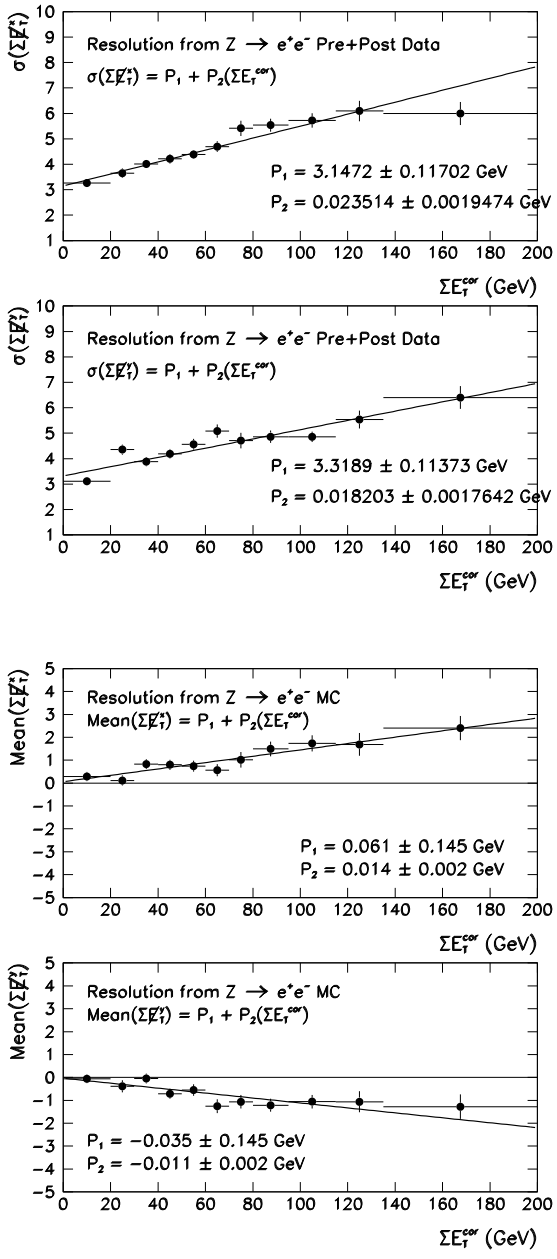

Figure B.3: The $\not\!\!E_T$ resolution (left) and offset (right) as determined from a sample of $Z^0 \to e^+e^-$ events. The resolutions and offsets are parameterized by $\mathrm{P}_1 + \mathrm{P}_2 \times \Sigma\mathrm{E}_\mathrm{T}^{\mathrm{Corrected}}$.

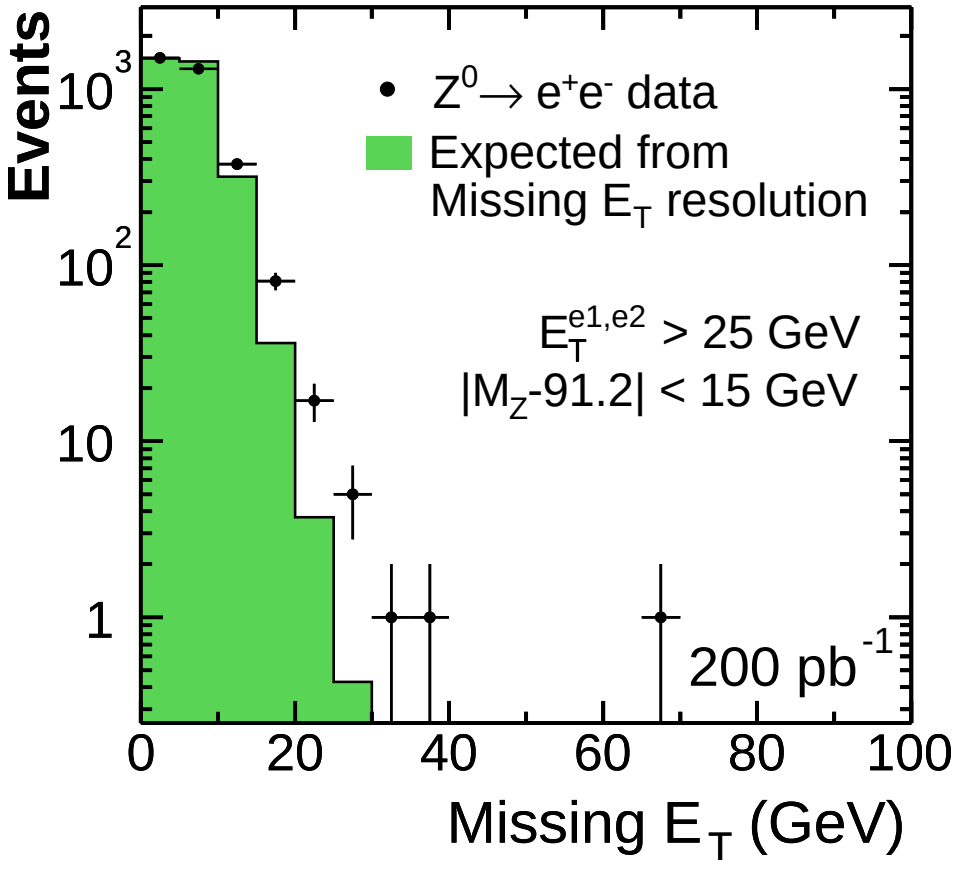

Figure B.4: The $\not\!\!E_T$ spectrum for $Z^0 \rightarrow e^+e^-$ data shown along with the expectation using the Gaussian $\not\!\!E_T$ method.

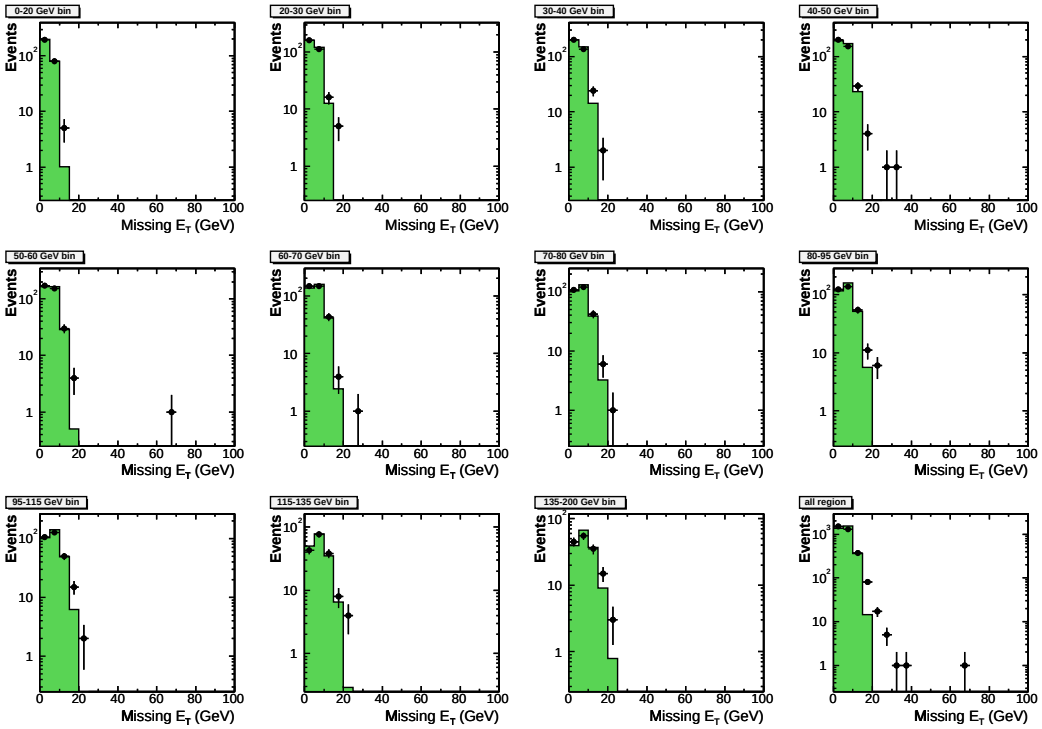

Figure B.5: The $\not\!\!E_T$ spectra for various regions in $\Sigma E_T^{\rm Corrected}$. They are (top to bottom, left to right) centered on $\Sigma E_T^{\rm Corrected}$ = 10, 25, 35, 45, 55, 65, 75, 87.5, 105, 125 and 167.5 GeV respectively. The $\not\!\!E_T$ spectra for $Z^0 \to e^+e^-$ data (dots) are shown along with the expectations using the Gaussian $\not\!\!E_T$ method (histogram).

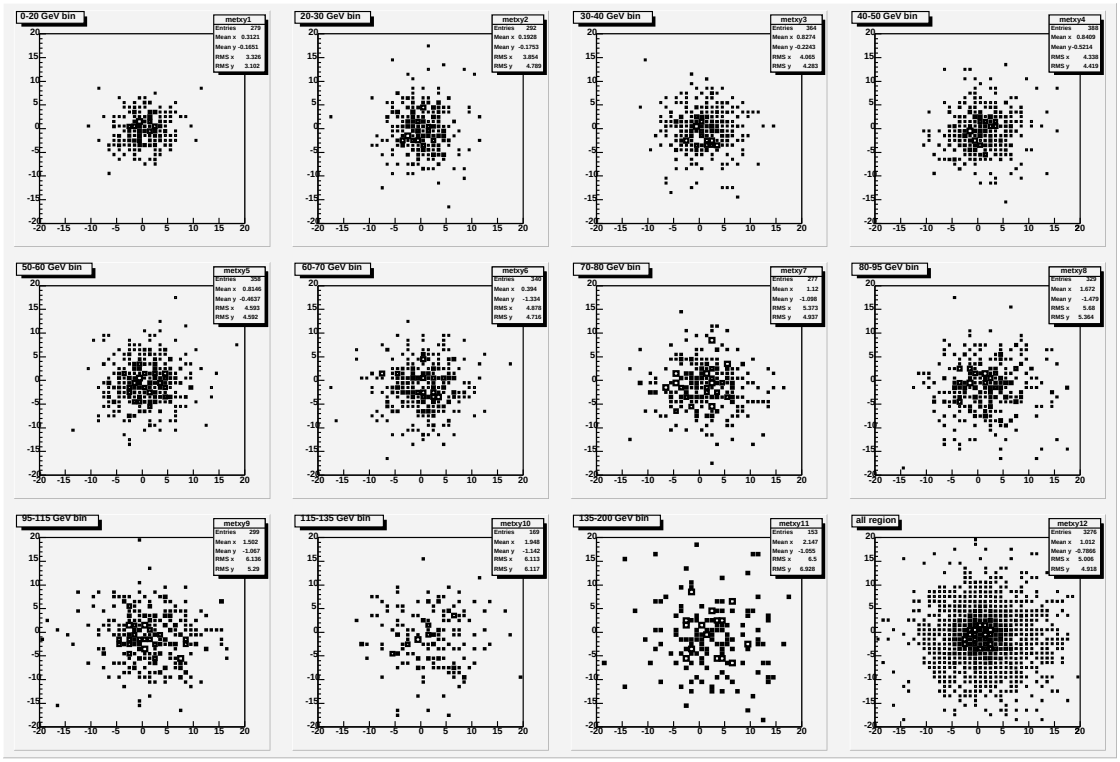

Figure B.6: The $\not\!\!E_T^x$ (x-axis) versus $\not\!\!E_T^y$ (y-axis) for various regions in $\Sigma \mathrm{E_T^{Corrected}}$. They are (top to bottom, left to right) centered on $\Sigma \mathrm{E_T^{Corrected}}$ = 10, 25, 35, 45, 55, 65, 75, 87.5, 105, 125 and 167.5 GeV respectively.

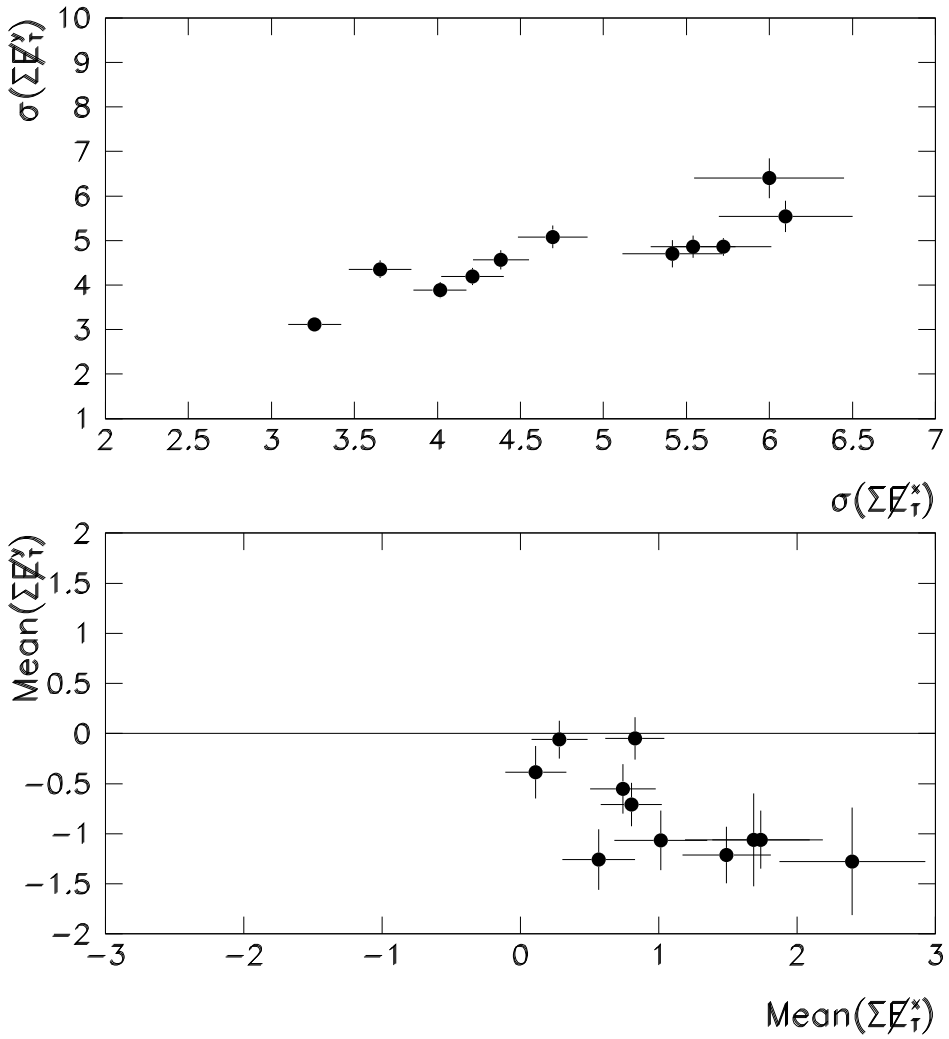

Figure B.7: The $\sigma(\not\!\!E_T^x)$ versus $\sigma(\not\!\!E_T^y)$ and the Mean $(\not\!\!E_T^x)$ versus Mean $(\not\!\!E_T^y)$ for various regions in $\Sigma \mathrm{E_T^{Corrected}}$.

Appendix C

Isolation and Conversion

We discuss pair-production of the lightest neutralinos via $p\bar{p} \to X \to \widetilde{\chi}_1^0\widetilde{\chi}_1^0$ (cascade decays: GMSB) or $p\bar{p} \to \widetilde{\chi}_1^0\widetilde{\chi}_1^0$ (direct decays: N1N1) leading to a two–photon plus missing energy signature in the detector. In order to compare GMSB diphoton samples with N1N1 and QCD diphoton samples (perhaps N1N1 and QCD processes have similar kinematics in some point of direct decay), a lightest chargino mass is chosen 125 GeV for GMSB and N1N1 since it is close to lower mass limits searched in CDF Run I. The QCD diphoton events are generated using PYTHIA MC program. With a minimum p_T of 10 GeV, we generated 500 thousand events corresponding to 1 fb^{-1}.

The photon E_T and η are used as kinematic acceptance cut at generator–level. In order to be sure how E_T and η cuts are working in GMSB, N1N1 and QCD diphoton samples, we looked at the probability by individually applying $E_T^\gamma > 13$ GeV and $|\eta^\gamma| < 1.1$ (central) to two photons generated. As we see in Figure C.1, the E_T cut distinguishes GMSB and N1N1 from QCD diphoton sample by η, and the η selection is similarly working. Table C.1 shows the generator acceptance which is the probability that two generated photons pass $E_T > 13$ GeV and given η selections: central or plug. At generator level GMSB/N1N1 diphoton sample have higher acceptance than QCD. This keeps us in suspense – what happen at detector level? We compare the angular separation between two generated photons, selected with kinematic acceptance cut described above, from QCD, N1N1 and GMSB diphoton samples to study

η *cut*	QCD	N1N1	GMSB
Central-Central	12.7 ± 0.1%	43.1 ± 0.2%	49.5 ± 0.2%
Central-Plug	19.8 ± 0.1%	34.7 ± 0.2%	30.6 ± 0.2%
Plug-Plug	14.5 ± 0.1%	7.8 ± 0.2%	5.4 ± 0.1%
Total	47.0 ± 0.1%	85.6 ± 0.1%	85.5 ± 0.1%

Table C.1: The acceptance table in diphoton samples of $E_T^\gamma > 13$ GeV according to the η^γ selections. For example, 'Central-Central' means that both photons are in the central region.

what effect this has on the isolation in detector level. We then discuss the activities of jets in the efficiencies of the diphoton samples. In addition the photon conversion probability is measured to make a check on data samples.

C.1 Isolation Energy

In the diphoton analysis photons are required to be isolated. Normally this means that the extra transverse energy inside a cone of radius ΔR, centered on the photon has to be less than a few GeV [48].

At generator level, the QCD diphotons come out back-to-back and the system is boosted if there is a jet. Thus the photons are well separated from the jet. In N1N1, to first order the lightest neutralinos are back-to-back but the photons come out randomly. This effect is due to the fact that if there is a jet it boosts the neutralinos, but the photons don't necessarily go in the directions of the neutralinos making them more likely near the jets. GMSB has lots of jets and the same issue as N1N1 about the photons direction, but the photons come out more randomly in GMSB as shown in Fig. C.2.

At detector level, the distributions of ΔR between a photon and the nearest jet are shown in Fig. C.3. A photon is required to pass all standard cuts except the energy isolation. Within jets with raw $E_T^{jet} > 10$ GeV and $|\eta^{jet}| < 2.5$, the nearest jet is considered as one which comes out near to a selected photon. To distinguish jet from a selected photon $\Delta R(\gamma, jet) > 0.2$ is used. Since there

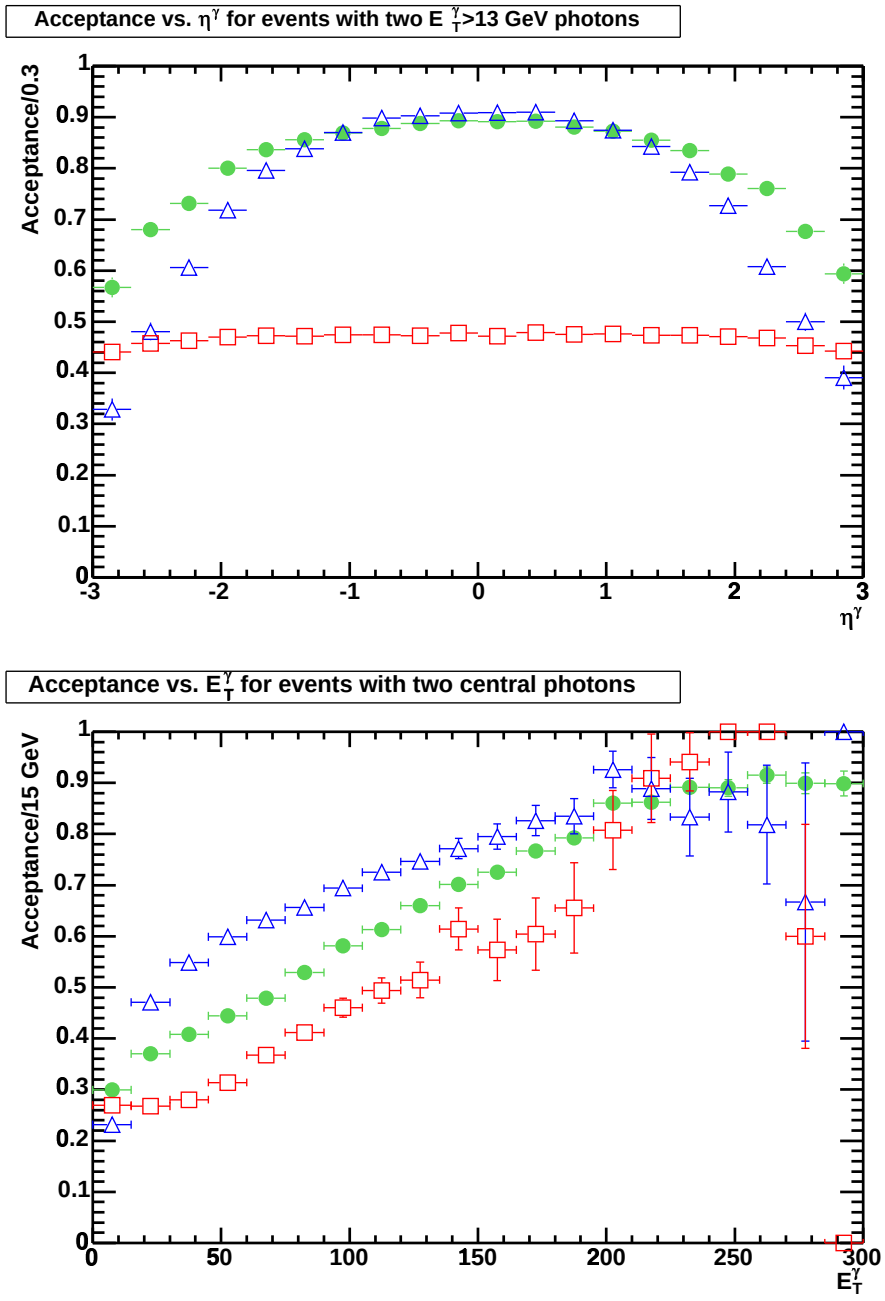

Figure C.1: Top plot shows the probability that the generated photon pass $E_T > 13$ GeV as a function of its η. and bottom plot shows the probability for the generated photon pass $|\eta| < 1.1$ as a function of its E_T. The red squares are from QCD, the green circles from N1N1, and the blue triangles from GMSB.

is the priority of photon candidate to jet when any object pass both photon and jet requirements, it is possible for the nearest jet to be another photon in such diphoton samples. The QCD diphotons come out back-to-back and most of the nearest jet must be another photon, well isolated. However, most of the GMSB/N1N1 photons fail isolation due to nearby one, regardless of jet or photon, and yet the N1N1 photons fail less than GMSB.

Fig. C.4 shows the distributions of the E_T^{γ} and its isolation energy, E_T^{Iso}, in diphoton events which passed all standard cuts. The number of jets expected from three samples are shown in Fig. C.5. GMSB and N1N1 have more jets than QCD. A photon surrounded with more energy is inefficient in isolation:

$$N_{jet}^{GMSB} > N_{jet}^{N1N1} > N_{jet}^{QCD} \tag{C.1}$$

C.2 Conversion

The conversion probability per photon is estimated counting a central photon with $E_T > 13$ GeV converted the electron pair at generator level. The calculated probability is $13 \pm 0.1\%$ for three samples: 12.7% of QCD, 12.6% of N1N1, and 12.5% of GMSB.

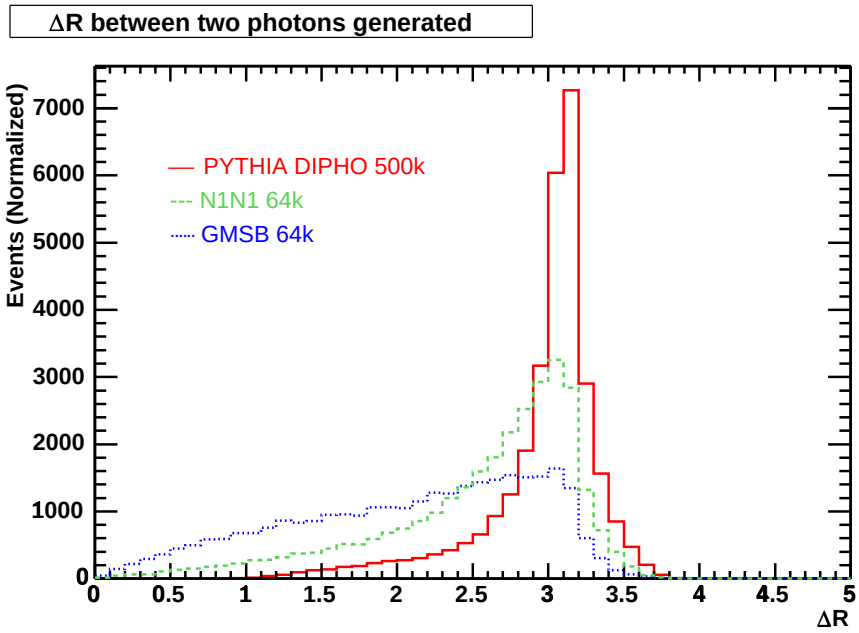

Figure C.2: The distributions of ΔR between two generated photons selected with the kinematic acceptance cut. The red solid line is for QCD, the green dash for N1N1, and the blue dot for GMSB.

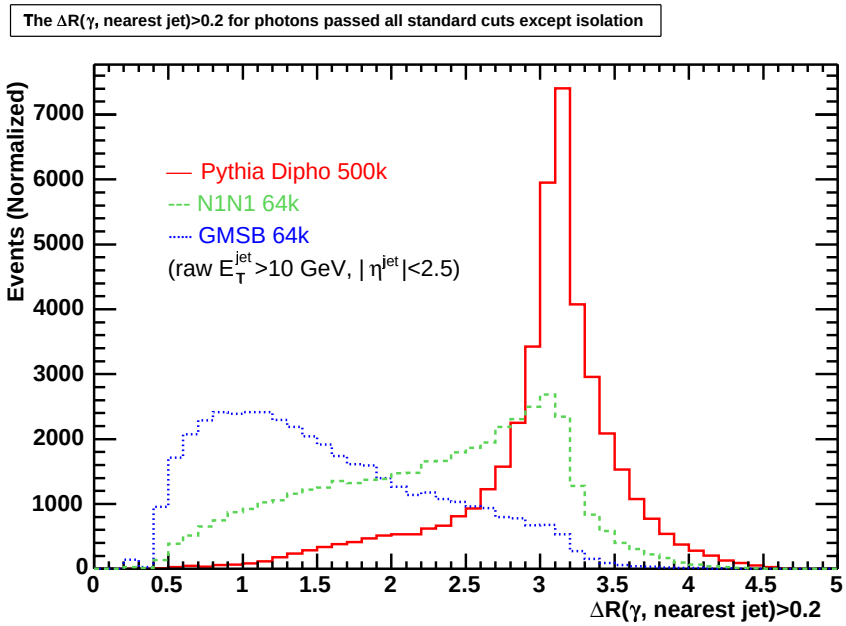

Figure C.3: The distributions of ΔR between a photon and the nearest jet. The red solid line is for QCD, the green dash for N1N1, and the blue dot for GMSB.

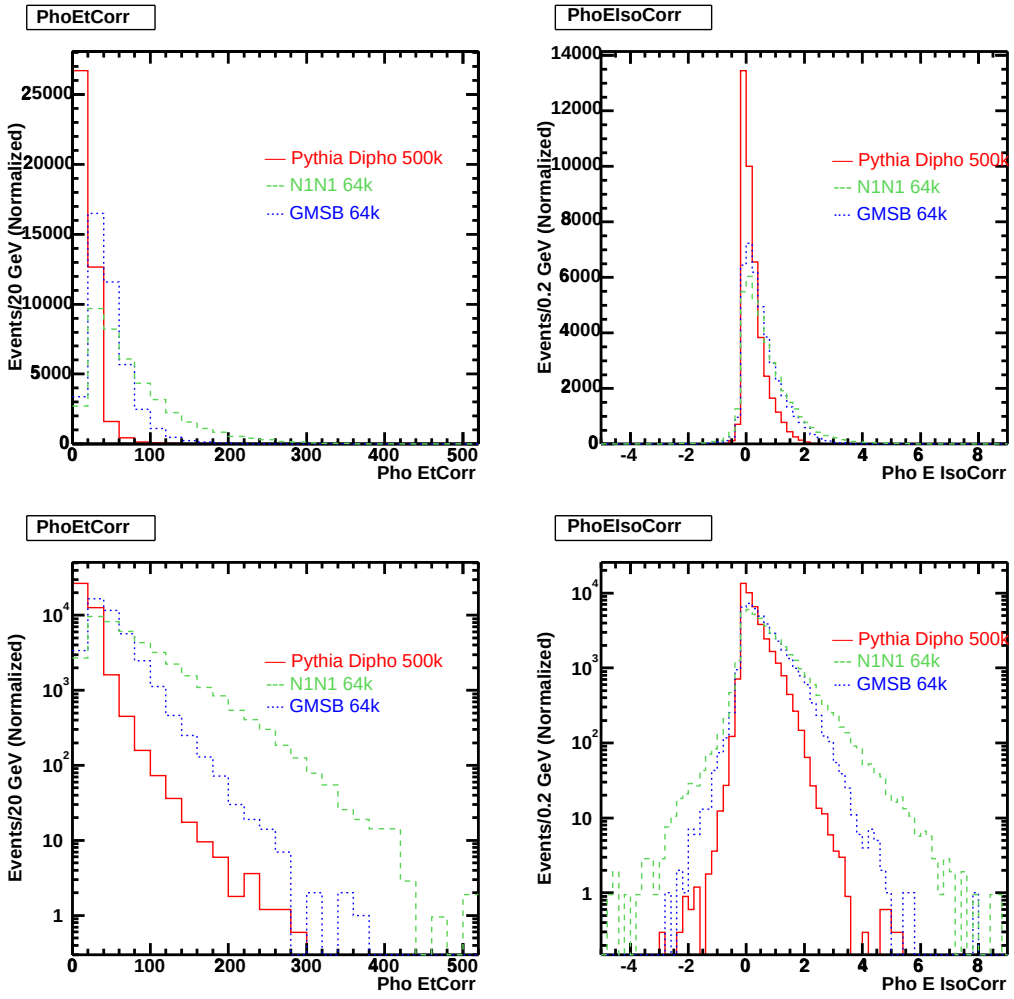

Figure C.4: The distributions of E_T^{γ} (left) and E_T^{Iso} (right). The top histograms are linearly plotted and the bottom histograms logarithmically. The red solid line is for QCD, the green dash for N1N1, and the blue dot for GMSB.

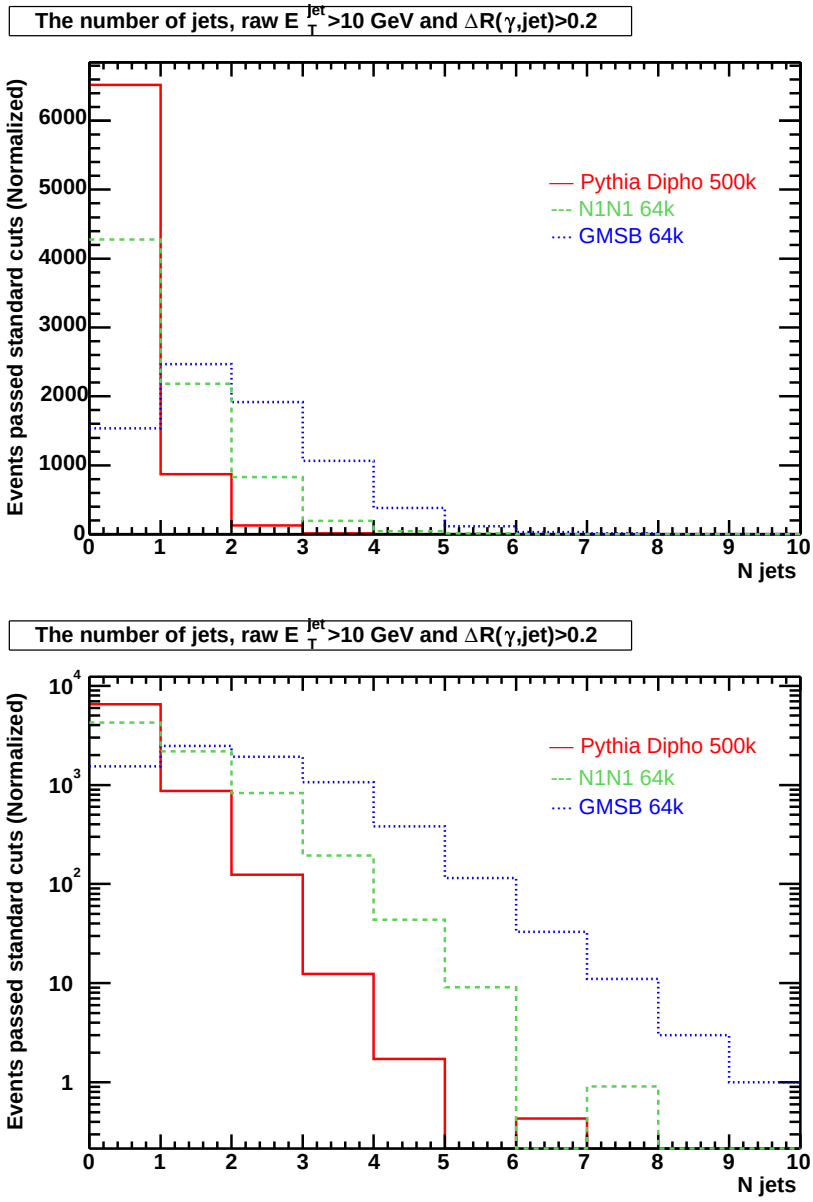

Figure C.5: The number of jets expected from diphoton events which passed all standard cuts. The top histograms are linearly plotted and the bottom histograms logarithmically. We counted all jets with raw $E_T^{jet} > 10$ GeV, $|\eta^{jet}| < 2.5$, and $\Delta R(\gamma, jet) > 0.2$. The QCD diphoton samples have less jets than GMSB/N1N1: $N_{jet}^{QCD} < N_{jet}^{N1N1} < N_{jet}^{GMSB}$. The red solid line is for QCD, the green dash for N1N1, and the blue dot for GMSB.

Bibliography

[1] See for example, F. Halzen and A. D. Martin, "Quarks and Leptons," John Wiley & Sons, 1984; C. Quigg, "Gauge Theories of the Strong, Weak, and Electromagnetic Interactions," Addison-Wesley, 1983; and I. S. Hughes, "Elementary particles," Cambridge University Press, 1990.

[2] S. Dimopoulos, S. Thomas, J. D. Wells, Nucl. Phys. B **488**, 39 (1997); S. Ambrosanio, G.D. Kribs and S.P. Martin, Phys. Rev. D **56**, 1761 (1997); G. F. Giudice and R. Rattazzi, Phys. Rept. **322**, 419 (1999); and S. Ambrosanio, G. Kane, G. Kribs, S. Martin and S. Mrenna, Phys. Rev. D **55**, 1372 (1997).

[3] Ray Culbertson *et al.*, "Low-Scale and Gauge-Mediated Supersymmetry Breaking at the Fermilab Tevatron Run II," FERMILAB-PUB-00/251-T and SLAC-PUB-8643, hep-ph/0008070.

[4] CDF Collaboration, F. Abe *et al.*, Phys. Rev. Lett. **81**, 1791 (1998) and Phys. Rev. D **59**, 092002 (1999).

[5] We use a cylindrical coordinate system that defines z as the longitudinal axis and along the proton beam axis, in which θ is the polar angle, ϕ is the azimuthal angle and $\eta = -\ln\tan(\theta/2)$. In general, all quantities are defined from $z_{\rm vertex} = 0$, $E_T = E \cdot \sin\theta$ and $p_T = p \cdot \sin\theta$ where E is the energy measured by the calorimeter and p the momentum measured in the tracking system. $\vec{\not\!\!E}_T = -\sum_i E_T^i \vec{n}_i$ where $\vec{n}_i$ is a unit vector that points from the interaction vertex to the ith calorimeter tower in the transverse plane. $\not\!\!E_T$ is the magnitude of $\vec{\not\!\!E}_T$.

[6] D. A. Dicus and S. Nandi, Phys. Rev. D **56**, 4166 (1997)

[7] H. Pagels and J. R. Primack, Phys. Rev. Lett. **48**, 223 (1982);
S. Weinberg, K. Hamaguchi and K. Suzuki, Phys. Rev. Lett. **48**, 1303 (1982);
T. Asaka, K. Hamaguchi and K. Suzuki, Phys. Lett. B **490**, 136 (2000).

[8] E. Calzetta, A. Kandus, F. D. Mazzitelli and C. E. M. Wagner, Phys. Lett. B **472**, 287 (2000).

[9] S. P. Martin, "A Supersymmetry Primer," `hep-ph/9709356`, and in *Perspectives on supersymmetry*, ed. by G. Kane, World Scientific, Singapore, pp 1-98 (1998)

[10] D. Toback and P. Wagner, "Prospects of Searches for Neutral, Long-Lived Particles which Decay to Photons using Timing at CDF," hep-ph/0407022, or see CDF Note 7089.

[11] S. Dimopoulos, M. Dine, S. Raby, S. Thomas and J. D. Wells, Nucl. Phys. Proc. Suppl. A **52**, 38 (1997).

[12] DØ Collaboration, S. Abachi *et al.*, Phys. Rev. Lett. **78**, 2070 (1997) and Phys. Rev. Lett. **80**, 442 (1998).

[13] D. Acosta *et al.*, Nucl. Instrum. Meth. A **494**, 57 (2002)

[14] *The CDF II Detector Technical Design Report,* FERMILAB-PUB-96/390-E (1996).

[15] ALEPH Collaboration, A, Heister *et al.*, Eur. Phys. J. **C25** 339 (2002); L3 Collaboration, M. Acciarri *et al.*, Phys. Lett. B **472**, 420 (2000); OPAL Collaboration, G. Abbiendi *et al.*, Eur. Phys. J. **C18** 253 (2000); DELPHI Collaboration, P. Abreu *et al.*, Eur. Phys. J. **C17** 53 (2000).

[16] J. Cockcroft and E. Walton. Proc. Roy. Soc., 136:619, 1932

[17] W. K. H. Panofsky *et al.,* Berkeley Proton Linear Accelerator. Rev. Sci. Instrum., 26:111, 1955.

[18] D. Mohl, G. Petrucci, L. Thorndahl, and Simon Van Der Meer. Physics and Technique of Stochastic Cooling. Phys. Rept., 58:73-119, 1980.

[19] `http://www-cdfonline.fnal.gov/opshelp/stores/`

[20] `http://www-cdf.fnal.gov/internal/people/links/JacoboKonigsberg/instr02.ps`

[21] S. Kilemnko *et al.*, "The CDF Run II Luminosity Monitor," CDF Note 4330.

[22] Muge Karagoz Unel and Richard Tesarek, "Beam Halo Monitoring at CDF," Nucl. Instrum. Meth. A **506**, 7 (2003), FERMILAB-PUB-02/304-E.

[23] S. Nahn, "Status of the CDF Run II Silicon Detector," CDF Note 6264.

[24] COT group, A. Mukherjee, R. Wagner, "CDF Central Outer Tracker," Nucl. Instrum. Meth. A **526**, 249 (2004), CDF Note 6267.

[25] Shin-Shan Yu *et al.*, "COT dE/dx Measurement and Corrections," CDF Note 6361.

[26] K. Anikeev *et al.*, "Construction and Installation of the CDF Time-Of-Flight Counters for Run II," CDF Note 5818.

[27] C. Grozis *et al.*, "The Time-Of-Flight Detector at CDF," Nucl. Phys. Proc. Suppl. A **47**, 344 (2001); Int. J. Mod. Phys. A16S1C, 1119 (2002).

[28] F. Abe *et al.*, Nucl. Instrum. Meth. A **271**, 387 (1988).

[29] CDF Collaboration, F. Abe *et al.*, Phys. Rev. D **52**, 4784 (1995) and D. Acosta *et al.*, Phys. Rev. D **65**, 112003 (2002).

[30] `http://www-cdf.fnal.gov/internal/dqm/goodrun/v4/goodv4.html`

[31] `http://www-cdf.fnal.gov/internal/physics/photon/docs/cuts.html`

[32] The corrected transverse energy of the photon, E_T, is the 2-tower sum from `emobj_alg::CEMFourMomentum::TwoTower(emObject,false).e()`, rather than the default EM Object E_T accessor (3-tower EM sum). This E_T is then corrected to the event vertex, the CES position at CES radius and `em_alg::cemcorr`.

[33] Y. Liu *et al.*, "Diphoton central-central cross-section measurement at CDF RunII," CDF Note 6312.

[34] D. Toback, "A Method of using the HADTDC System to reject Large MET Events with Out-of-Time Energy," CDF Note 6928.

[35] P. Onyisi, "A Study of Photon Fakes from Beam Halo Events," CDF Note 6009.

[36] D. Benjamin *et al.*, "Measurement of $W\gamma$ and $Z\gamma$ Production at CDF in Run 2," CDF Note 6601, and "Theoretical Predictions for $W\gamma$ and $Z\gamma$ Production in Run II," CDF Note 6619.

[37] C.Rott *et al.*, "Run-II Search for Scalar Bottom Quarks from Gluino Decays," CDF Note 6542.

[38] B. C. Allanach *et al.*, Eur. Phys. J. **C25** 113 (2002). We take the messenger mass scale $M_{\rm m} = 2\Lambda$, $\tan(\beta) = 15$, $\mathrm{sgn}(\mu) = 1$ and the number of messenger fields $N_{\rm m} = 1$.

[39] H. Baer, F. E. Paige, S. D. Protopopescu and X. Tata, hep-ph/0001086.

[40] H. L. Lai *et al.*, Eur. Phys. J. **C12** 375 (2000).

[41] R. Brun *et al.*, CERN-DD/EE/84-1 (1987).

[42] P. Simeon and D. Toback, "An Advantage of Setting Cross Section Limits on the Total Production Mechanism When Multiple Processes Produce the Same Final State," CDF Note 7084.

[43] The K-factor has a small dependence on the $\widetilde{\chi}_1^{\pm}$ mass and is taken from W. Beenakker *et al.*, Phys. Rev. Lett. **83**, 3780 (1999) and T. Plehn http://pheno.physics.wisc.edu/~plehn/prospino/prospino.html.

[44] W.K. Sakumoto and A. Hocker, "Event $|Z_{vtx}| \leq 60$ cm Cut Efficiency for Run II," CDF Note 6331.

[45] Tracey Pratt and Ray Culbertson, "Search for Randall Sundrum Gravitons in High Mass Diphotons," CDF Note 6560.

[46] J. Conway, CERN 2000-005, 247 (2000). We assume a flat prior in the production cross section up to a high cutoff; the limit is not significantly dependent on the value of the cutoff.

[47] E. Boos, A. Vologdin, D. Toback and J. Gaspard, Phys. Rev. D. **66**, 013011, (2002).

[48] Arthur Maghakian and Steve Kuhlmann, "Isolation Cut Efficiency in Direct Photon Analysis," CDF Note 2214.